

REPORT DOCUMENTATION PAGE

Form Approved
OMB NO. 0704-0188

Public Reporting burden for this collection of information is estimated to average 1 hour per response, including the time for reviewing instructions, searching existing data sources, gathering and maintaining the data needed, and completing and reviewing the collection of information. Send comment regarding this burden estimates or any other aspect of this collection of information, including suggestions for reducing this burden, to Washington Headquarters Services, Directorate for Information Operations and Reports, 1215 Jefferson Davis Highway, Suite 1204, Arlington, VA 22202-4302, and to the Office of Management and Budget, Paperwork Reduction Project (0704-0188), Washington, DC 20503.

1. AGENCY USE ONLY (Leave Blank)	2. REPORT DATE June 2000	3. REPORT TYPE AND DATES COVERED Final	
4. TITLE AND SUBTITLE Turbulence and Dispersion over Complex Terrain		5. FUNDING NUMBERS DAAH04-95-C-0041	
6. AUTHOR(S) R. I. Sykes D. S. Henn		8. PERFORMING ORGANIZATION REPORT NUMBER AR 724	
7. PERFORMING ORGANIZATION NAME(S) AND ADDRESS(ES) The Titan Corporation, Titan Research and Technology Div P.O. Box 2229 Princeton NJ 08543-2229		9. SPONSORING / MONITORING AGENCY NAME(S) AND ADDRESS(ES) U. S. Army Research Office P.O. Box 12211 Research Triangle Park, NC 27709-2211	10. SPONSORING / MONITORING AGENCY REPORT NUMBER ARO 32836.1-EV
11. SUPPLEMENTARY NOTES The views, opinions and/or findings contained in this report are those of the author(s) and should not be construed as an official Department of the Army position, policy or decision, unless so designated by other documentation.			
12 a. DISTRIBUTION / AVAILABILITY STATEMENT Approved for public release; distribution unlimited.		12 b. DISTRIBUTION CODE	
13. ABSTRACT (Maximum 200 words) Large-Eddy Simulation (LES) is used to generate explicit time-dependent, three-dimensional representations of the turbulent flow field over sinusoidal hills. An advanced Lagrangian puff model is used to calculate dispersion from a small source near the surface within the turbulent flow. The puff model represents the local shear distortions, and includes a splitting algorithm to give an accurate description of the inhomogeneous velocity field In order to provide a measure of confidence in the LES flow simulations, an extensive comparison with laboratory measurements of turbulent flow over wavy surfaces has been completed. Model predictions compare very favorably with the experimental data. Dispersion calculations using the LES velocity fields show strong effects of the terrain on releases from point sources near the surface. In separated flow conditions, wide variability in cloud behavior is observed due to the retention of material within the recirculating valley flow.			
14. SUBJECT TERMS Large-eddy Simulation Sinusoidal terrain Turbulent dispersion			15. NUMBER OF PAGES 89
			16. PRICE CODE
17. SECURITY CLASSIFICATION OR REPORT UNCLASSIFIED	18. SECURITY CLASSIFICATION ON THIS PAGE UNCLASSIFIED	19. SECURITY CLASSIFICATION OF ABSTRACT UNCLASSIFIED	20. LIMITATION OF ABSTRACT UL

NSN 7540-01-280-5500

Standard Form 298 (Rev.2-89)
Prescribed by ANSI Std. Z39-18
298-102

20001124 020

DTIC QUALITY ENGINEERED 4

A.R.A.P Report No. 724

Turbulence and Dispersion over Complex Terrain

R. I. Sykes

D. S. Henn

**The Titan Corporation
Titan Research & Technology Div.
P.O. Box 2229
Princeton, NJ 08543-2229**

Army Research Office

CONTRACT No. DAAH04-95-C-0041

June 2000

SUMMARY

The technique of Large-Eddy Simulation (LES) is applied to flow over terrain, in order to generate turbulent velocity fields for use in dispersion calculations. The objective of the research is to study the effects of simple terrain on the diffusion of a tracer from a localized source. Most of our understanding of atmospheric turbulence is based on studies over horizontally-homogeneous terrain, but the presence of hills or ridges disturbs the atmospheric boundary layer and presumably affects the dispersion properties. LES provides the most fundamental methodology available for studying atmospheric turbulence, and is therefore particularly appropriate for modeling dispersion in the presence of idealized terrain.

We first evaluate the capability of LES using laboratory data on neutral flow over sinusoidal ridge terrain with a variety of amplitudes. Good agreement is obtained for both mean flow and observed turbulence statistics. We then utilize the LES model to study atmospheric boundary layer flow over similar sinusoidal terrain, and calculate the dispersion of a tracer using a Lagrangian puff model and also a particle trajectory model. The effects of heat flux on the dispersion properties are examined, and found to reduce the effect of the terrain. This is due to the increased vertical mixing under convective conditions, which limits the effect of the increased shear near the terrain surface.

Quantitative information on dispersion rates has been obtained for idealized terrain profiles. Several basic dispersion phenomena associated with flow and turbulence fields over terrain have been elucidated. In addition to the effects of convection on streamwise dispersion, the LES calculations also show the effect of separated flow regions. Material released or entrained into a separated flow region, such as that within a steep-sided valley, is detrained over a relatively long timescale. The detrainment is not incremental, however, but intermittent in nature on the timescale of the recirculation. This implies that a small release within a separated flow will be randomly ejected, and the downwind concentration is therefore extremely uncertain.

In summary, LES has been shown to be a valuable tool for studying boundary layer flow and dispersion over simple terrain.

TABLE OF CONTENTS

Section	Page
SUMMARY	iii
1. INTRODUCTION	1
2. COMPARISON WITH EXPERIMENTAL DATA	3
3. TRACER DISPERSION RESULTS	5
4. CONCLUDING REMARKS	7
5. REFERENCES	9
APPENDIX A: LARGE-EDDY SIMULATION OF FLOW OVER WAVY SURFACES	A-1
APPENDIX B: LARGE-EDDY SIMULATION OF DISPERSION OVER TERRAIN	B-1
APPENDIX C: DISPERSION EFFECTS OVER RIDGE/VALLEY TERRAIN	C-1

1. INTRODUCTION

The presence of terrain can greatly influence the structure of the atmospheric boundary layer, modifying both the mean flow and the turbulent fluctuations from the values over a flat surface. Flow acceleration over hillcrests, separation and flow reversal behind steep hills, and buoyancy-driven drainage circulations are all familiar examples of flow phenomena associated with topography. Many studies have been conducted to investigate turbulent boundary layer flow over terrain, and the wide range of phenomena has necessitated many simplifying assumptions. Since the complexity of the real atmospheric situation masks the individual processes, most theoretical studies focus on idealized terrain to isolate specific aspects of the dynamics. Thus, for example, many researchers have studied neutral or near-neutral flow over topography, using a variety of turbulence closure models, to elucidate the effect of different empirical modeling assumptions on the predictions. For example, Jackson and Hunt (1975), Mason and Sykes (1979), and Hunt et al. (1988) present linearized analytical solutions using a turbulent eddy-viscosity model for flow over idealized terrain. Higher-order turbulence closure models have been applied by Sykes (1980), Newley (1986), and Belcher et al. (1993), and numerical solutions for various closure models have been presented by Taylor et al. (1976) and Wood and Mason (1993). Belcher and Hunt (1998) review the subject with emphasis on the turbulence distortions and the interaction with vertical wind shear.

We will focus on the aerodynamic flow studies described above, since they are concerned with smaller scale terrain features and their effects on boundary layer turbulence. This is directly relevant to the dispersion of material from localized sources, and extends the homogeneous terrain approximations used in traditional models for the turbulent boundary layer structure. Other researchers have examined mean flows induced by larger scale terrain features (mountain ranges) and buoyancy-driven circulations (valley/slope winds), but these studies are principally concerned with mean flow effects, and place less emphasis on the turbulence modifications. Since our main interest is in extending the atmospheric diffusion parameterizations to include small-scale terrain effects, we will concentrate on terrain with length scales comparable to the atmospheric boundary layer depth, i.e., on the order of a few kilometers or less.

The terrain-induced distortions of the flow imply modification of the dispersion properties of the boundary layer, since material is transported by the turbulent wind field. Here, it is important to distinguish mean flow effects from turbulent diffusion effects, although the two

will be coupled in general. The dispersion properties of the modified boundary layer turbulence have not been extensively studied, and will therefore be the major objective of the current work.

As discussed above, there have been a number of approaches using turbulence closure models to calculate the effect of terrain on the turbulent boundary layer. Large-eddy simulation (LES) is an alternative approach to Reynolds-average closure, which minimizes the empirical assumptions involved in the calculation. LES uses a 3-dimensional time-dependent numerical solution of the spatially averaged Navier-Stokes equations to represent the larger scale turbulent eddies explicitly. Turbulent motions smaller than the resolved scale must still be parameterized using some form of closure model, since it is impractical to resolve the turbulent spectrum down to viscous scales in the atmosphere. However, predictions are less sensitive to the subgrid closure, and the dependence is reduced as the numerical resolution is improved.

Recent studies of turbulent boundary layer flow over terrain have been reported by Krettenauer and Schumann (1992), for convective conditions, and Gong et al. (1996), for neutral conditions. Both papers study two-dimensional sinusoidal terrain, since this is the simplest possible geometry that can be considered using the periodic lateral boundary conditions used in most LES calculations. Krettenauer and Schumann consider zero mean wind and focus on the effects of terrain on the convective eddies, while Gong et al. study neutral flow over waves and compare with wind tunnel observations. In this report, we will examine wind flow over simple terrain with specific emphasis on the dispersion of a passive tracer in the flow. However, we first compare the LES results with available laboratory data on flow over sinusoidal terrain, in order to examine the ability of LES to model the terrain-induced phenomena.

2. COMPARISON WITH EXPERIMENTAL DATA

Since Large-eddy simulation of flow over terrain is not well-established, we first make an extensive comparison between detailed laboratory measurements and the numerical predictions. Prior to examining dispersion of a passive tracer within the numerically generated turbulent flow field, we must ascertain that the computational results are consistent with real flows. To this end, we have compared LES predictions with a number of laboratory experiments, as reported in Henn and Sykes (1999).

An extensive set of measurements of channel flow over wavy surfaces has been presented by Hanratty and coworkers at the University of Illinois. These experiments cover a wide range of slopes and Reynolds numbers since the nature of the flow depends strongly on these parameters. We have concentrated on the experiments with larger Reynolds numbers and steeper slopes since they are most relevant to the atmospheric flows we are interested in. However, we have made some comparisons over a range of slopes, including a flat channel.

In modeling the laboratory and atmospheric flows, the major required modification to the basic Cartesian LES technique presented previously in Sykes and Henn (1989, 1992) involves the use of the terrain-following coordinate transformation of Clark (1977). This introduces a number of additional terms to the basic equations and complicates the numerical implementation. In particular, the pressure field must be computed iteratively, with the number of iterations increasing with slope. Thus the computational effort is greatly increased. Details can be found in Henn and Sykes (1999).

Although the laboratory experiments involve fully turbulent flow, finite-Reynolds-number effects, especially near the lower wavy boundary, are still evident. Therefore, the basic LES model is modified for this comparison with the implementation of a no-slip boundary condition and a wall-damping function on the turbulent length scale. Thus, the wall shear-stress is determined by the viscosity and the assumption of parallel flow at the first grid level. The momentum and turbulent kinetic energy transport equations are also modified with viscous diffusion terms, but it should be emphasized that it is not intended to construct a true low-Reynolds-number model (e.g., one that would handle transitional flows), but is included principally to impose the no-slip boundary condition.

This study involves model comparisons with experiments over a wide range of wave slopes, from flat to moderate (with nearly linear perturbations) to steep (with strongly separated flow). The available measurements include mean streamwise velocity and its variance, skewness and flatness, wall shear-stress, surface pressure and integrated form drag. Although the calculations use moderate resolution (typically 48 points in each horizontal direction and around 70 in the vertical), the LES model appears capable of predicting most of the salient features of the laboratory flow. In particular, the response of the mean flow and streamwise velocity variance to different wave amplitudes is accurately predicted even close to the surface. Model sensitivity to resolution and domain size confirms the moderate resolution/domain results. The resolution tests also indicate that the subgrid model results in the appropriate transfer of energy to the resolved scale as resolution increases.

One striking aspect of the LES results is a large increase in lateral velocity fluctuation intensity on the upslope of the ridges. The increase seems to be associated with vortex stretching as the flow is accelerated over the crest of the ridge, and the vortices are relatively long-lived. The increase in the turbulence intensity scales with the square of the terrain slope, indicating that it is a nonlinear phenomenon in contrast to the linear distortions of the "upstream" turbulence. Unfortunately, the lateral velocity component was not measured in any of the laboratory experiments, so this feature is still to be confirmed.

For applications to atmospheric flows, it is important to be able to predict variations in the mean velocity, turbulence and surface pressure along the wave, as well as to characterize separation for large slope waves (e.g., location of separation, the mean flow and variance in the separation zone). It is amply confirmed that the LES model is capable of predicting these features qualitatively and quantitatively. The results from this study have been published in the Journal of Fluid Mechanics, and the complete paper is included as Appendix A of this report.

3. TRACER DISPERSION RESULTS

The tracer dispersion calculations require the solution of the passive scalar conservation equations. Since the source size will often be less than the grid size used to generate the velocity field, Lagrangian methods are used for the scalar field so that subgrid growth can be computed. In particular, when early-time, near-source behavior is of primary interest, the generalized Gaussian puff method of Sykes and Henn (1995) is employed. For late-time statistics, i.e., when the scalar field is large compared to the length scale of the terrain, a particle method, which accounts for subgrid diffusivity with a random-walk model, is used since only the overall centroid and second-moments are of interest.

This study focuses on dispersion in the presence of simple, idealized terrain so that the effects of parameters such as slope and release location can be clearly illustrated. Given the constraints of periodic boundary conditions (on the velocity field) and the extensive comparison with velocity measurements over sinusoidal waves, two-dimensional sinusoidal terrain is also used for the dispersion calculations. Although obviously an idealization, this is a reasonable prototype of ridge-valley terrain.

A limited range of terrain slopes and atmospheric stabilities are considered in the two conference papers (Henn and Sykes 1996,1998). Specifically, the maximum slopes are 0, 0.25 and 0.5; with a wavelength of 2 km, these correspond to maximum ridge elevations of 0, 159 m and 318 m, respectively. For all cases, the boundary layer depth is approximately 1000 m. The maximum elevations are a substantial fraction of this, so it is expected that the terrain will substantially modify the boundary layer flow. Two uniform surface temperature fluxes are considered: $0.03 \text{ }^{\circ}\text{Kms}^{-1}$ and $0.0045 \text{ }^{\circ}\text{Kms}^{-1}$, which give convective velocity scales of 1 ms^{-1} and 0.5 ms^{-1} , respectively. The higher heat flux results in flow which is dominated by large-scale convective eddies, while the lower value is closer to neutral stability in character. The LES domain is a 4 km cube, but the periodic nature of the velocity field is utilized to allow the dispersion calculation to extend beyond the nominal velocity field domain. Independent dispersion realizations are obtained by varying the horizontal location of the source within the same LES velocity field; this procedure is repeated for a number of independent velocity fields. Thus, ensemble dispersion statistics are generated from 12 to 24 realizations.

The principal results of this study concern the sensitivity of short-range dispersion to release location as well as the enhanced dispersion over longer ranges. Clearly the relatively large terrain slopes considered here induce complex flow features such as re-circulation zones, intermittent separation, vertical mixing and vertical shears, which increase sensitivity to release location. This is particularly evident with the lower heat flux case; in contrast, the higher heat flux produces stronger vertical mixing, reducing the overall effect of the terrain. Long-range calculations also clearly point out the effects of stronger vertical mixing. For instance, the intermediate terrain slope and larger heat flux results in no enhanced long-range, streamwise dispersion compared with the flat case, whereas the low heat flux case gives an effective diffusion coefficient twice the flat value. Both heat fluxes produce significant enhanced dispersion with the largest slope, but, as expected, the low heat flux shows the larger increase (about 50% greater than the larger heat flux).

4. CONCLUDING REMARKS

The ability of LES to reproduce the observed flow features in boundary layer flow over a sinusoidally varying surface has been demonstrated through comparison with laboratory data. The moderate Reynolds numbers achieved in the laboratory are sufficiently high for the significant turbulence effects to be similar to those for very high Reynolds number flow. Extensive comparison with a variety of experiments and observed flow statistics, in addition to numerical sensitivity studies, provides sound evidence that the LES flow fields accurately model many of the significant features of flow over ridges. One of the most striking aspects of the LES results is a large increase in lateral velocity fluctuation intensity on the upslope of the ridges. The increase appears to be associated with vortex stretching as the flow is accelerated over the crest of the ridge, but the lateral velocity component was not measured in any of the laboratory experiments, so this feature is still to be confirmed.

Further LES calculations have been presented for buoyancy-driven turbulence over sinusoidal ridges. These simulations are more representative of atmospheric flow, where buoyancy forcing is always present. Stability categories ranging from near-neutral to strongly convective have been considered. The neutral laboratory comparisons provide confidence that the LES can properly represent the flow features, since buoyancy-driven turbulence is more amenable to LES. This is because the buoyancy-driven eddies are large-scale features, and consequently easier to resolve in the numerical calculation.

Dispersion calculations for a passive tracer emitted from a small, instantaneous source, located at several positions relative to the terrain variations, were then presented. The dispersion results clearly show the increased rate of diffusion, particularly in the streamwise direction, associated with the terrain-induced turbulence and mean flow modifications. The results also show that increasing the surface buoyancy flux reduces the diffusion rates, due to the increased vertical mixing rates. The major mechanism for streamwise extension of the cloud is the increased vertical wind shear over the valley regions; increasing the vertical mixing reduces the effective shear. An extreme example of the shear occurs for a separated flow region, where material entrains and detains from the recirculation zone where mean the streamlines are closed. Under unstable conditions, the exchange rate between the recirculation zone and the free stream above is much higher than under neutral conditions. Thus under neutral conditions, we see much more separation between particles trapped within the separation region and particles outside.

This study has demonstrated the capability of LES to model turbulent dispersion in boundary layer flow over terrain. We have restricted the calculations to highly idealized terrain forms, since our understanding of the full complexity of atmospheric situations can only be improved in stages. LES has been shown to reproduce the important features of the distorted turbulent flow, and several aspects of the dispersion process have been elucidated, using the LES velocity fields. Further work is necessary to extend the calculations to other terrain forms.

5. REFERENCES

Belcher, S. E. and J. C. R. Hunt (1998), "Turbulent flow over hills and waves", *Ann. Rev. Fluid Mech.*, **30**, 507-538.

Belcher, S. E., T. M. J. Newley and J. C. R. Hunt (1993), "The drag on an undulating surface induced by the flow of a turbulent boundary layer", *J. Fluid Mech.*, **249**, 557-596.

Gong, W., P. A. Taylor and A. Dornbrack (1996), "Turbulent boundary-layer flow over fixed aerodynamically rough two-dimensional sinusoidal waves", *J. Fluid Mech.*, **312**, 1-37.

Henn, D. S. and R. I. Sykes (1996), "Large-eddy simulation of dispersion over terrain", Ninth Joint Conference on the Applications of Air Pollution Meteorology, AMS, Atlanta, GA, 401-405.

Henn, D. S. and R. I. Sykes (1998), "Dispersion effects over a ridge/valley system", 10th Joint Conference on the Applications of Air Pollution Meteorology, AMS, Phoenix, AZ, 215-219.

Henn, D. S. and R. I. Sykes (1999), "Large-eddy simulation of flow over wavy surfaces", *J. Fluid Mech.*, **383**, 75-112.

Hunt, J. C. R., S. Leibovich and K. J. Richards (1988), "Turbulent shear flow over low hills", *Quart. J. Roy. Met. Soc.*, **114**, 1435-1470.

Jackson, P. S. and J. C. R. Hunt (1975), "Turbulent wind flow over a low hill", *Quart. J. Roy. Met. Soc.*, **101**, 929-955.

Jackson, P. S. and J. C. R. Hunt (1975), "Turbulent wind flow over a low hill", *Quart. J. Roy. Met. Soc.*, **101**, 929-955.

Krettenauer, K. and U. Schumann (1992), "Numerical solution of turbulent convection over wavy terrain", *J. Fluid Mech.*, **237**, 261-300.

Mason, P. J. and R. I. Sykes (1979), "Flow over an isolated hill of moderate slope", *Quart. J. Roy. Met. Soc.*, **105**, 383-395.

Newley, T. M. J. (1986), "Turbulent air flow over hills", Ph. D. Thesis, Cambridge University.

Sykes, R. I. (1980), "An asymptotic theory of incompressible turbulent boundary-layer flow over a small hump", *J. Fluid Mech.*, **101**, 647-670.

Taylor, P. A., P. R. Gent and J. M. Keen (1976), "Some numerical solutions for turbulent boundary-layer flow above fixed, rough, wavy surfaces", *Geophys. J.Roy. Astr. Soc.*, **44**, 177-201.

Wood, N. and P. J. Mason (1993), "The pressure force induced by neutral, turbulent flow over hills", *Quart. J. Roy. Met. Soc.*, **119**, 1233-1267.

Appendix A

Published in the Journal of Fluid Mechanics, 1999, Vol. 383

Large-Eddy Simulation of Flow Over Wavy Surfaces

Abstract

Large-eddy simulation is used to investigate fully developed turbulent flow in a neutral channel wherein the lower wall is sinusoidal. The numerical results are compared with experimental observations for wave slopes ranging from 0 to 0.628. Particular emphasis is placed on the separated flow induced by a large-amplitude wave. A detailed comparison with the data of Buckles *et al.* (1984) shows generally good agreement. LES surface pressures are integrated to calculate form drag as a function of wave slope. Drag is found to increase quadratically with slope for small-amplitude waves, with a somewhat slower increase for larger amplitudes. However, comparison with experimental measurements is confounded by uncertainties with the values reported in the literature. An interesting feature characteristic of all wavy surface simulations is an increase in transverse velocity fluctuations on the wave upslope. Although the precise mechanism responsible is not known, analysis shows it to be associated with temporally persistent vortex-like structures localized near the surface. The magnitude of the fluctuation increase appears to scale quadratically with slope for small-amplitude waves, in contrast to the streamwise fluctuations, which increase linearly.

1. Introduction

The use of large-eddy simulations to model complex flow configurations is becoming increasingly common. One of the earliest applications to go beyond the horizontally homogeneous channel case was in modeling turbulent convective flow over sinusoidal terrain, e.g. Krettenauer and Schumann (1992), Walko, Cotton and Pielke (1992) and Dörnbrack and Schumann (1993). Simulations over flat homogeneous terrain have demonstrated that this type of flow is particularly amenable to LES since the dominant thermally-driven eddies are on the scale of the mixed-layer height (or channel depth) and so are typically well-resolved (Schmidt and Schumann 1989; Mason 1989). While LES has shown that wavy terrain can modify the large-scale flow in the convective boundary layer, horizontally-averaged profiles are not very different from the flat case, even in the presence of a mean wind. This is because strong vertical mixing tends to reduce the velocity shears caused by even large surface slopes. However, the

effects of terrain on more neutrally stable flow are likely to be much more dramatic since even relatively small slopes can induce significant variations in the mean flow and turbulence structure (Sykes 1980; Taylor 1977; Belcher and Hunt 1998).

This research effort is oriented towards atmospheric flow over terrain which, while idealized, is nonetheless realistic in terms of slope and wavelength. However, before making this extension, it is desirable to verify the LES against laboratory measurements. Gong *et al.* (1996) recently presented experimental observations and LES calculations for wind-tunnel flow over sinusoidal terrain with a growing boundary layer. However, the flow is complicated by the non-uniformity of the boundary layer and may also be influenced by the lateral walls of the wind tunnel. Hanratty and coworkers have presented an extensive set of measurements of channel flow over wavy surfaces, e.g., Zilker, Cook and Hanratty (1977), Zilker and Hanratty (1979), Buckles, Hanratty and Adrian (1984, BHA hereafter; 1986), Frederick and Hanratty (1988), Kuzan, Hanratty and Adrian (1989) and Hudson, Dykhno and Hanratty (1996). We will focus in particular on the data of BHA, who present extensive measurements of the mean and fluctuating velocity for turbulent channel flow over an aerodynamically smooth, large-amplitude sinusoidal surface. However, we will also consider smaller-amplitude waves in order to establish confidence in the model as well as examine the effects of varying wave slope. Although the data we are comparing with are all for smooth walls and hence Reynolds number dependent, the Reynolds numbers are high enough so that the flows are fully turbulent. Nonetheless, the LES model does account for finite Reynolds number effects since a no-slip velocity boundary condition is used.

Analytic flow studies, e.g., Sykes (1980), Hunt *et al.* (1988) and Belcher *et al.* (1993), have shown that terrain-induced turbulence modifications are subject to rapid variation close to the surface. The equilibrium log-layer relations are valid only very near the boundary, and an inner layer develops in which advection and distortion of the turbulence are important, with a vertical scale much smaller than the horizontal wavelength. The inner layer is typically about 5% of the wavelength, making explicit resolution of eddies in this region very difficult. These difficulties also affect the ability to represent surface forces correctly, since the forces are closely coupled to the details of the flow near the boundary. However, the total drag force is also related to the total energy dissipation in the flow, and we expect wavy surfaces, especially in the case of large-scale separation, to generate resolvable eddies well suited to modeling by LES.

Direct numerical simulations of channel flow over wavy surfaces, e.g., Maaß and Schumann (1994,1996) , De Angelis *et al.* (1997) and Cherukat *et al.* (1998) have successfully reproduced many of the laboratory observations for moderate Reynolds number, while also providing great

detail on the flow structure. For instance, both De Angelis *et al.* and Cherukat *et al.* note increased transverse fluctuations on the wave upslope, which we have observed for a range of wave amplitudes. However, the application of DNS is limited since resolution requirements become prohibitive for high Reynolds number flow.

The paper is organized as follows. First the LES model is described, with particular emphasis on features relevant to finite Reynolds number flow over wavy surfaces, since the infinite Reynolds number, Cartesian version of the model has been described elsewhere. The numerical methods and boundary conditions are then briefly outlined. After summarizing the basic flow configurations and parameters, model results are compared with a number of experiments. We first present results from flat channel calculations and then proceed to examine a small-amplitude wavy surface case. Next, LES results are compared in detail with the data of BHA for separated flow over a large-amplitude wave. A limited comparison between flows over waves with different amplitudes is then made; the dependence of form drag on wave slope is examined in particular. Finally, the interesting feature of increased transverse turbulent fluctuations on the wave upslope is investigated.

2. LES model

2.1 *Model equations*

The basic LES model has previously been applied to buoyancy-driven turbulence (Sykes and Henn, 1989; Henn and Sykes 1992) and a neutral boundary layer (Sykes and Henn, 1992). For the current application, the terrain-following coordinate transformation of Clark (1977) is used for accurate representation of the surface boundary conditions. The equations of motions are based on the filtered Navier-Stokes equations and follow the approach of Moin and Kim (1982) in explicitly including viscosity so that a no-slip boundary may be imposed. The resolved-scale Cartesian velocity components $u_i = (u, v, w)$ are solved as functions of transformed coordinates $\tilde{x}_i = (\tilde{x}, \tilde{y}, \tilde{z})$, defined in terms of Cartesian coordinates $x_i = (x, y, z)$ by $\tilde{x} = x$, $\tilde{y} = y$ and $\tilde{z} = \eta(x, y, z)$. The transformation

$$\eta = (z - h)/J \quad (1)$$

where $J = 1 - h/H$, maps the domain between the lower wavy surface at $z = h$ and the upper flat channel wall at $z = H$ onto a rectangular domain. The lower surface is a two-dimensional infinite wavetrain defined by $h(x, y) = a[1 + \cos(2\pi x/\lambda)]$, with wavelength λ and amplitude a .

Cartesian derivatives for an arbitrary scalar field ϕ are given in terms of the transformed coordinates as

$$\frac{\partial}{\partial x_i} \phi = \frac{\partial \tilde{x}_j}{\partial x_i} \frac{\partial}{\partial \tilde{x}_j} \phi \equiv G^{ji} \frac{\partial}{\partial \tilde{x}_j} \phi \quad (2)$$

where the summation convention is assumed. Note that $J^{-1} = \det(G^{ij})$. Since a fluid of constant density ρ is considered here, it is convenient to define $V = \rho J$. Then, following Krettenauer and Schumann (1992), the model equations are given concisely as

$$\frac{\partial}{\partial \tilde{x}_i} (VG^{ij} u_j) = 0 \quad (3)$$

$$\frac{\partial}{\partial t} (Vu_i) + \frac{\partial}{\partial \tilde{x}_j} (VG^{jk} u_k u_i) = -\frac{\partial}{\partial \tilde{x}_j} (VG^{ji} p) + \frac{\partial}{\partial \tilde{x}_j} (VG^{jk} \tau_{ik}) + \nu \frac{\partial}{\partial \tilde{x}_j} (VG^{jk} D_{ik}) + VP_x \delta_{1i} \quad (4)$$

where p is the dynamic pressure, τ_{ij} is the subgrid stress tensor, ν is the kinematic viscosity and P_x is a uniform pressure gradient in the x -direction that drives the flow. It should be noted that this is not intended as a low Reynolds number model; the viscous term is only important in a thin layer near the wall and is included principally to impose the no-slip boundary condition.

The subgrid turbulence model uses a turbulent kinetic energy transport equation based on the second-order closure model of Lewellen (1977). The subgrid velocity variance, q^2 , is obtained from the conservation equation

$$\frac{\partial}{\partial t} (Vq^2) + \frac{\partial}{\partial \tilde{x}_i} (VG^{ij} u_j q^2) = -\tau_{ij} VD_{ij} - \frac{\partial}{\partial \tilde{x}_i} (VG^{ij} F_j) - \nu \frac{\partial}{\partial \tilde{x}_i} \left(G^{ij} \frac{\partial}{\partial \tilde{x}_k} (VG^{kj} q^2) \right) - 2bV \frac{q^3}{\Lambda} \quad (5)$$

where F_i is the subgrid flux, Λ is the subgrid turbulence length scale (or filter scale) and the velocity deformation tensor is given by

$$VD_{ij} = \frac{\partial}{\partial \tilde{x}_k} (VG^{kj} u_i + VG^{ki} u_j) \quad (6)$$

The first term on the right-hand side of (5) represents subgrid turbulence production due to gradients in the resolved velocity field, the next two terms represents transport due to diffusive fluxes and the last term models the dissipation. The subgrid fluxes are given by

$$V\tau_{ij} = S_m q \Lambda VD_{ij} \quad (7)$$

$$VF_i = S_H q \Lambda \frac{\partial}{\partial \tilde{x}_j} (VG^{ji} q^2) \quad (8)$$

The various empirical model constants are taken from Lewellen (1977) so that $b = 0.125$, $S_m = 1/4$ and $S_H = 1/3$.

Finally, the subgrid length scale is specified algebraically by

$$\frac{1}{\Lambda^2} = \frac{1}{\ell^2} + \frac{1}{\Lambda_{\max}^2} \quad (9)$$

where ℓ is a function of distance normal to the nearer of the top or lower bounding surfaces and Λ_{\max} is problem dependent. The philosophy of Mason and Callen (1986) is followed in setting the subgrid filter scale independent of the numerical grid, subject to the requirement that the resulting large-scale eddies are adequately resolved. While, in principle, one could use an arbitrarily fine grid for a fixed filter scale, in practice the idea is to reduce the length scale more or less in proportion with the grid size so that smaller-scale turbulent eddies will be resolved. The wall function ℓ is simply set proportional to normal distance in infinite-Reynolds number applications. However, it was found that the length scale must be damped more rapidly as the wall is approached when imposing a zero-slip boundary condition for finite-Reynolds number flow. Therefore, following Moin and Kim (1982), we use the Van Driest exponential damping function such that

$$\ell = \alpha n \left(1 - \exp(-n^+ / A^+) \right) \quad (10)$$

where n is distance normal to the nearest wall, $\alpha = 0.65$ from Lewellen (1977), $A^+ = 25$, $n^+ = n \tau_0^{1/2} / \nu$ and τ_0 is the local instantaneous wall shear stress.

2.2 Numerical implementation

The numerical scheme is similar to that used in the Cartesian model (Sykes and Henn, 1989), although the coordinate transformation introduces a number of new terms and other complications; details of the implementation generally follow Clark (1977). The model uses a standard second-order accurate, finite difference energy-conserving scheme on a staggered grid with leapfrog time differencing. A small amount of smoothing (1%) is used to couple the two time levels and prevent the time-splitting instability. Diffusion terms are modeled using central differencing with the DuFort-Frankel approximation to provide stable integration. The DuFort-Frankel scheme is second-order accurate and consistent with the advection-diffusion equation if $d = K(\Delta t / \Delta z^2)$ is small, where K is the total diffusivity. At the wall, $K = \nu$ and d is less than 0.05 for all cases. In fact, d is generally less than 0.01 over most of the domain since the timestep, which is limited by the vertical Courant condition near the wall, is small. The grid spacing is uniform horizontally but varies vertically, with fine resolution at the walls expanding to a section of uniform spacing comparable to the horizontal spacing.

The elliptic equation for the pressure field is obtained by applying the finite-difference approximation of the divergence operator (3) to the partially advanced velocity fields, i.e., including all terms from (4) except the pressure gradients. The pressure field is then computed from the resulting equation such that zero divergence of the velocity field is maintained. However, the non-orthogonal coordinate transformation makes the equation non-separable, so the direct solver of the Cartesian model must be used in an iterative scheme as in Clark (1977) and Krettenauer and Schumann (1992). The pressure equation is written in the form

$$L_0(p) = N(p) + D(\tilde{u}_i) \quad (11)$$

where L_0 is the finite-difference representation of the Cartesian Laplace operator (i.e., the case with $h = 0$), N represents the terms of the operator resulting from the coordinate transformation and D is the numerical divergence operator, here applied to the partially advanced velocity fields (denoted by a tilde). The solution is obtained using the direct Cartesian solver for each iteration of the system

$$L_0(p^{(n+1)}) = N(p^{(n)}) + D(\tilde{u}_i) \quad (12)$$

where the superscripts denote iteration and the previous timestep value is used as the initial guess $p^{(0)}$. The iteration continues until the maximum change in p is less than 10^{-5} times the maximum value of p in the domain. The rate of convergence depends on the wave slope since N is generally proportional to the square of the slope. For the maximum slope of 0.628 considered here, convergence requires 5 to 7 iterations.

2.3 Boundary conditions

Periodic boundary conditions are imposed at all lateral boundaries. A no-slip condition is imposed on the lower wall by setting u and v below the surface equal and opposite to the values on the first level above the surface. For some of the flows described in the next section, a no-slip condition is also imposed on the upper wall. However, since the flow details at the top of the channel are generally not of primary interest, the upper boundary is usually treated as a rough wall. In this case, a logarithmic profile is used to relate the top wall shear stress to the tangential velocity half a grid length below the wall.

The momentum fluxes at the lower surface are determined by the no-slip condition at the wall and by assuming flow parallel to the wall at the first grid level. The total momentum flux is given by

$$\tau_0 = \nu |u_i^s| z_n^{-1} \quad (13)$$

where $u_i^s = (u_s, v_s, h_x u_s + h_y v_s)$ is the velocity vector located half a grid length above the lower surface, h_x and h_y are the surface slopes in the x - and y -directions, respectively, and z_n is the normal distance to the wall. Note that for the purpose of setting the wall stress, w is defined in (13) so that u_i^s is parallel to the lower surface. The normal distance is related to the transformed vertical grid spacing at the wall, $\Delta\tilde{z}_0$, by

$$z_n = \frac{J\Delta\tilde{z}_0}{2\sqrt{1+h_x^2+h_y^2}} \quad (14)$$

In a local coordinate system defined by the unit surface normal \hat{n}_i and the unit vector in the direction of the tangential velocity, $\hat{u}_i = u_i^s |u_i^s|^{-1}$, the full stress tensor at the surface is

$$\underline{\underline{\tau}}'_s = \tau_0 \begin{bmatrix} 0 & 0 & 1 \\ 0 & 0 & 0 \\ 1 & 0 & 0 \end{bmatrix} \quad (15)$$

where the prime denotes the local coordinate system. The stress tensor (15) must be rotated into the global Cartesian frame since the momentum equations use the Cartesian velocity components. Using the fact that $h_y = 0$, this rotation results in

$$\underline{\underline{\tau}}_s = \frac{\nu}{J\Delta\tilde{z}_0/2} \begin{bmatrix} -2h_x u_s & -h_x v_s & (1-h_x^2)u_s \\ -h_x v_s & 0 & v_s \\ (1-h_x^2)u_s & v_s & 2h_x u_s \end{bmatrix} \quad (16)$$

which defines the lower boundary condition for the total stress tensor, $\tau_{ij} + \nu D_{ij}$.

The pressure boundary condition is set to insure consistency between the numerical discretizations of the momentum equation (4) and the pressure source term N from (11) when imposing the constraint of zero normal flow at the wall. By requiring that both u_i and \tilde{u}_i (the partially advance velocity used in (11)) satisfy this constraint, we obtain a numerical expression of the form $\delta_z p + f(\bar{p}^z) = 0$ for $\tilde{z} = 0$, where δ_z denotes a vertical finite difference and f is a function of the vertically-averaged pressure \bar{p}^z . The numerical expression for the pressure source term is given by $N = \delta_z f + N_H(\delta_z \bar{p}^z)$, where N_H is a horizontal difference operator. Thus, setting $\delta_z p = 0$ and $f = 0$ at $\tilde{z} = 0$ provides all the necessary boundary conditions for the pressure solver while maintaining consistency with the zero normal flow condition.

3. Flow parameters

The principal focus of this investigation is the configuration of BHA, i.e., channel flow over an infinite array of two-dimensional large-amplitude sinusoidal waves. However, since this LES

model had not previously been applied to flows at finite-Reynolds numbers, a flat channel with $Re \approx 12000$ was first simulated to test model performance. Then, to test the model with the transformed equations, channel flow over a small-amplitude wavy surface was calculated. Additionally, intermediate wave amplitude configurations were examined as part of a limited investigation into variations of surface pressure, drag, turbulence intensity and flow separation with wave slope.

3.1 Numerical experiments

The basic flow geometry is illustrated in Figure 1 and all configurations are summarized in Table 1. For the wavy surface cases, the standard computational domain contains two wavelengths; test calculations with a single wave (not shown) gave quite different results whereas calculations with four waves were very similar to the standard domain results. This can be seen from the values for case BHA1L given in Tables 3 (form drag) and Table 4 (variance perturbations) which agree within 10% of the standard domain case BHA1. Note also that grid resolutions for the $2a/\lambda = 0, 0.031$ and 0.2 cases are varied along with the subgrid length scale to demonstrate numerical convergence.

The vertical resolution requirements are fairly stringent near the wall, requiring that the lowest grid level be in the viscous sublayer below $z^+ \approx 10$ (using local wall scaling). Using the experimental results to estimate the maximum mean wall shear stress, it was determined that grid levels below $\tilde{z}/H \approx 0.005$ and 0.01 were required for the BHA and flat configurations, respectively. The minimum vertical grid spacings shown in Table 1 are less than these estimates to accommodate fluctuations in local wall stresses resulting from very thin viscous shear layers.

All cases were initialized from previous fully-turbulent runs and continued until an approximate equilibrium between the imposed constant streamwise pressure gradient and the wall stresses, including pressure forces, was attained. The statistics for all cases presented below are from periods after this equilibrium was reached. Averaging was done over a time of $30H/U_b$ or longer, as well as the lateral coordinate and position of equal phase relative to the surface wave. (The flat cases were averaged over the lateral and streamwise coordinates.) The velocity scale used here is given by a bulk velocity that is independent of streamwise location:

$$U_b = (H - a)^{-1} \int_h^H \bar{u} dz \quad (17)$$

where the overbar denotes averaging. Henceforth, it will be assumed that all velocities are normalized with respect to U_b .

Case	L	W	λ	$2a/\lambda$	Grid Size	$\Delta\tilde{z}_{\min}$	$\Delta\tilde{z}_{\max}$	Λ_{\max}	Re
F	2	1	∞	0	48x48x90	0.002	0.02	0.005	11810
FR	2	1	∞	0	80x80x90	0.002	0.02	0.003	11820
S1	2	1	1	0.031	48x48x91	0.002	0.02	0.005	6560
S1R	2	1	1	0.031	80x80x102	0.002	0.02	0.003	5720
S2	1.984	0.992	0.992	0.050	48x48x71	0.00124	0.0248	0.00620	11050
S3	2.034	1.017	1.017	0.100	48x48x71	0.00127	0.0254	0.00636	10580
S4	2	1	1	0.125	48x48x67	0.0025	0.025	0.00625	10800
BHA1	2.143	1.072	1.072	0.200	48x48x71	0.00134	0.0268	0.00670	10600
BHA1R	2.143	1.072	1.072	0.200	80x80x99	0.00134	0.0167	0.00402	10450
BHA1L	4.286	1.072	1.072	0.200	96x48x71	0.00134	0.0268	0.00670	12000
BHA2	2.143	1.072	1.072	0.200	48x48x71	0.00134	0.0268	0.00670	5990
BHA3	2.143	1.072	1.072	0.200	48x48x71	0.00134	0.0268	0.00670	20060

Table 1. Non-dimensional parameters for the various LES calculations, listed in order of increasing slope. L , W , and λ are the streamwise length (x -direction), transverse width (y -direction) and wavelength, respectively; $\Delta\tilde{z}_{\min}$ and $\Delta\tilde{z}_{\max}$ are the minimum (at the lower wall) and maximum vertical transformed grid sizes, respectively; Λ_{\max} is the maximum subgrid filter length scale; and the Reynolds number is defined by $Re = U_b \delta / \nu$, where δ is the channel mean half-height and U_b is the bulk velocity, defined in the text. All lengths are normalized by the mean channel depth, $H - a$. The computational grid sizes are given as the number of grid points in the streamwise, transverse and vertical directions, respectively.

To check that the flow was sufficiently stationary for computing steady, long-time averages, the time evolution of U_b and the total pressure and shear stress forces at the walls were monitored. As an illustration, Figure 2 shows the time history of the integrated surface pressure force, defined in equation (19), for case BHA1. High-frequency (period $\approx H/U_b$) and low-frequency (period $\approx 20H/U_b$) fluctuations are apparent. Nonetheless, it is evident that a meaningful long-time average can be defined over the averaging period shown on the figure.

All simulations were performed on a Windows NT workstation employing a DEC Alpha 21164 300 MHz processor. For the standard BHA1 case (48x48x71 grid), a single step takes about 7 cpu-s. Thus, with a non-dimensional timestep of 8.6×10^{-4} , the integration to a time of 75 took approximately 170 cpu-h. By comparison, the flat channel case F (48x48x90 grid) requires

about 5.5 cpu-s per step; with a timestep of 3.7×10^{-3} and an integration time of 166, the total run time was about 69 cpu-h.

It will be noted that the Reynolds numbers in Table 1 do not match the experimental values exactly. Since P_x is held constant throughout the integration, the final bulk velocity and, hence, Reynolds number cannot be controlled directly, but results from the balance between wall stresses and imposed pressure gradient.

In presenting the LES results, the resolved turbulence fluctuations are defined as $\overline{u_i' u_j''}$ where $u_i'' = u_i - \bar{u}_i$ while the total fluctuations include the subgrid components, $\overline{u_i' u_j'} = \overline{u_i'' u_j''} - \bar{\tau}_{ij}$. We also define the r.m.s. streamwise velocity fluctuations as $\sigma_u = \sqrt{\overline{u'^2}}$, and similarly for v and w . Note that in presenting results for the flat channel and small-amplitude wave, wall scaling is denoted by a superscript “+”, i.e., velocities are normalized by $u_* = \sqrt{\langle \bar{\tau}_0 \rangle}$ and heights by v/u_* , where angle brackets indicate averaging over a wavelength.

3.2 Laboratory experiments

As mentioned in the introduction, Hanratty and coworkers at the University of Illinois have presented an extensive set of measurements of channel flow over wavy surfaces; those referred to in this paper are summarized in Table 2. The experiments cover a wide range of slopes and Reynolds numbers since the nature of the flow depends strongly on these parameters, as illustrated in the flow regime map presented by Kuzan *et al.* (1989). We have concentrated on experiments with $Re \approx 10^4$ where the mean flow separates for $2a/\lambda$ somewhat greater than 0.05.

All experiments were conducted in a rectangular water channel with a cross section of 5.08×61 cm. A long flat section preceded a sinusoidal wavetrain machined into the lower channel wall such that the mean cross section was unchanged. The flat section was long enough that the flow was fully turbulent before encountering the first wave and the channel wide enough for the mean flow to be essentially two-dimensional. Spatially periodic flow was established fairly rapidly; measurements were typically taken over the eighth wave in a series of ten. (The measurements of Hudson, *et al.* (1996) were taken over the 31st of 36 waves.)

Reference	Measurements	Re	$2a/\lambda$	Observed Features
Frederick and Hanratty (1988)	Mean and fluctuating streamwise velocity (LDV)	6400	0.031	Linear shear stress response
Hudson, <i>et al.</i> (1996)	Mean and fluctuating streamwise and vertical velocities, Reynolds stress (LDV)	3380	0.100	Separated flow
Zilker and Hanratty (1979)	Mean streamwise velocity, wall pressure, wall shear stress (split-film thermal probes, pressure taps, electro-chemical surface probes)	29300 14730 30000 30530	0.05 0.125 0.125 0.200	Instantaneous reverse flow, non-linear stress response Separated flow
Buckles, <i>et al.</i> (1984,1986)	Mean and fluctuating streamwise velocity, wall pressure (LDV and pressure taps)	12300* 10700*	0.125 0.200	Separated flow

Table 2. Summary of relevant experiments of flow over wavy surfaces conducted in the laboratory of Hanratty and coworkers. The measurement techniques are given in parentheses.

*These Reynolds numbers have been modified from their published values to conform with the bulk velocity definition (17). See Section 6 for further discussion.

4. Flat channel

We first present results for a flat channel at $Re \approx 12000$ with no-slip boundary conditions at both walls, similar to the LES study of Moin and Kim (1982). Figure 3 shows the mean streamwise velocity profiles for cases F and FR compared with the data of Hussain and Reynolds (1970). The calculated profiles are in reasonable agreement with the data, with only a slight underprediction evident in the outer part of the wall layer ($z^+ \approx 10$ to 30). The profiles show very little sensitivity to resolution, an indication of numerical convergence. LES profiles from only the lower wall are plotted, but those from the upper wall are virtually indistinguishable, an indication of adequate statistical averaging.

Figure 4 shows profiles of the turbulence intensities, resolved and total, in the vicinity of the wall while Figure 5 shows the profiles over the lower half of the channel. The peak values near the wall match the experiments well, as do the values in the middle of the channel. The streamwise intensity is somewhat overpredicted for $z^+ \approx 20$ to 80, since the LES shows a more gradual fall off from the near-wall peak. It is evident that the vertical intensity prediction is determined principally by the subgrid model near the wall; τ_{33} increase too rapidly from the wall but nonetheless shows good agreement overall. It can be seen that the resolved components increase as the subgrid filter scale is reduced but the total intensities are not significantly changed, indicating an appropriate transfer of energy from the subgrid to the resolved component as resolution is increased. The agreement with the experimental data is comparable to the LES of Moin and Kim (1982).

5. Small-amplitude wavy surface

Before presenting results for the large-amplitude wave, we simulate flow over a small-amplitude wave that tests the coordinate transformation while still yielding results close to the flat channel. This flow is of interest in its own right, so we will compare with experimental and theoretical results. This will enable us to examine the model predictions without the complicating effects of separation.

5.1. Mean velocity

Results from cases S1 and S1R, with $2a/\lambda = 0.031$, are compared with the measurements of Frederick and Hanratty (1988). Figure 6 shows the wavelength-averaged mean streamwise velocity. The LES results are averaged along lines of constant η while the data are averaged along lines of constant height above the wave surface. For this small slope, the difference between the two averaging definitions is negligible. The predicted profiles are generally in close agreement with the measurements and the two numerical resolutions result in nearly identical profiles. As with the comparison shown in Figure 3 for the flat channel, the LES profiles are somewhat low over the approximate range $10 < z^+ < 30$, although the discrepancy is slightly less here. The flat channel data of Hussain and Reynolds (1970) are also shown in the figure; it is evident that the wavelength average matches these data quite closely, as would be expected for linear perturbation at this small slope.

The velocity profiles at different locations along the wave are shown in Figure 7. Profiles are paired such that they should be symmetric around the wavelength average (shown as a dashed

line), assuming perfectly linear behavior. The overall agreement with the data is good, particularly above the viscous sublayer, $z^+ > 10$. The largest discrepancies occur near the surface of the upslope profiles at $x/\lambda = 0.6$ and 0.7, where the measurements show greater flow acceleration. It seems that the LES predictions in these cases show more linear behavior, i.e., the paired LES profiles are more nearly symmetric about the wavelength average than the experimental data.

In a study of flow over hills using second-order closure and mixing-length models, Newley (1985) examines the streamwise velocity perturbation profile above the wave crest and finds that the maximum can be expressed as

$$\Delta u_{\max} = \frac{\beta u_0^2(\ell_0)}{ak u_0^2(\ell_m)} \quad (18)$$

where u_0 is the unperturbed mean streamwise velocity, ak is the maximum slope, wavenumber $k = 2\pi/\lambda$, ℓ_m is the height of the maximum perturbation above the crest, ℓ_0 is an outer layer scale set to k^{-1} for periodic hills and β is an $O(1)$ constant. A fit to the second-order closure results gives $\beta \approx 1$ (and $\beta \approx 0.8$ for the mixing-length model). The LES results, using the wavelength average velocity for u_0 , give $\beta = 1.5$. This discrepancy partly reflects the fact that ℓ_m is higher with the LES model: $\ell_m/\lambda = 0.013$ compared with approximately 0.006 for Newley's second-order closure calculations for hills with similar slopes. Of course, Newley's calculations are for rough surfaces, so these results are not directly comparable, especially since ℓ_m is just barely above the viscous sublayer. If we re-examine the data of Figure 7 in terms of the perturbation velocity near the surface, as is done in Frederick (1986), we see that the prediction of ℓ_m matches the experiment quite well. As can be seen from Figure 8, the LES profiles at the wave crest and trough show good overall agreement with the data, although the overprediction at $x/\lambda = 0.5$, $z^+ > 10$ is more noticeable with the linear scale. The maximum perturbations above the crest are only about 10% higher than the experimental values, indicating that the LES prediction of β is reasonably consistent with the experimental data.

5.2. Turbulence intensity

Streamwise turbulence intensity measurements from Frederick (1986) are shown in Figure 9 along with the LES results. The predictions compare favorably overall with the experiment in that the basic variations with location are reproduced. The turbulence intensities generally are out of phase with the pressure gradients: a positive (adverse) pressure gradient has a destabilizing effect and hence increases the velocity fluctuations while the opposite is true for negative

(favorable) pressure gradients. Thus the peak values increase from profiles at $x/\lambda = 0.1$ to 0.5 and decrease thereafter to $x/\lambda = 1$. The LES peak values match the measurements quite well regarding both magnitude and location (typically around $z^+ \approx 20$). Near the wall, the LES predictions are generally low and show greater differences between the paired profiles. Away from the wall, $z^+ > 100$, the LES also tends to underpredict the fluctuation intensity. However, flat channel measurements from the same facility (Frederick, 1986) show 10–20% greater centerline intensities than typically given in the literature, e.g., Hussain and Reynolds (1975).

To relate the LES results to some of the theoretical models of flow over small-amplitude waves, e.g., Sykes (1980) and Newley (1986), we show the streamwise and vertical velocity variance perturbation fields for the high resolution case S1R in Figure 10. (The transverse component will be discussed in Section 9.) The streamwise component is defined as $\overline{\Delta u'^2} = \overline{u'^2} - \langle \overline{u'^2} \rangle$, with the vertical component defined similarly. There is qualitative agreement with the closure model predictions: a distinct surface layer is evident; the perturbations maximize above and are almost 180° out of phase with the surface layer; the maximum positive streamwise perturbation occurs over the trough while the largest negative perturbation occurs over the crest. A quantitative comparison with the models is not meaningful due to differences in the bottom boundary conditions; the inner layers defined in Sykes (1980) and Belcher *et al.* (1993) both would fall within the viscous sublayer of the LES, thus invalidating their assumption of a log profile. It is interesting to note that $\overline{\Delta u'^2}$ above the surface layer is out of phase with $\overline{\Delta w'^2}$. Whereas the streamwise variance decreases over the wave crest, the vertical variance increases there, a result not predicted by closure models or rapid distortion theory but observed in measurements over hills (Belcher *et al.* 1993). It should also be noted that the maximum in $\overline{\Delta u'^2}$ is localized close to the surface compared with $\overline{\Delta w'^2}$. Thus, although the maximum magnitude of $\overline{\Delta u'^2}$ is nearly ten times greater than $\overline{\Delta w'^2}$, it decays rapidly with height and so for the region $\eta/\lambda > 0.1$, the perturbations are of comparable magnitude.

The results shown in Figure 10 are determined to some extent by the subgrid model, especially near the surface. Therefore, it is important to examine how much of the total variances are explicitly resolved in the LES. The wavelength-averaged fractions of resolved variances, defined as $\langle \overline{u''^2} \rangle / \langle \overline{u'^2} \rangle$ for the streamwise variance and similarly for the transverse and vertical variances, are shown in Figure 11 for cases S1 and S1R. It can be seen that more than 90% of the streamwise variance is explicitly resolved over the entire domain for both numerical resolutions. In contrast, only 10% of the vertical variance is resolved very close to the surface in S1 while the minimum resolved fraction of the transverse variance approaches 60%. Higher resolution results in a noticeable improvement: the minimum resolved fraction increases

to 35% for the vertical variance and 75% for the transverse component. In the standard resolution case S1, all components are more than 80% resolved for $\eta/\lambda > 0.1$. This level of resolution is achieved for $\eta/\lambda > 0.05$ with the higher-resolution of S1R. Thus, the variance perturbations shown in Figure 10 are essentially resolved above the surface layer; the calculations within the surface layer must be viewed with some caution however.

5.3. Surface shear stress

Zilker (1976) presents surface wall stress data for this flow; a comparison with the LES results is shown in Figure 12. The model predictions are close to the measurements in both phase and magnitude, although the experimental scatter suggests caution in making any definitive conclusions. It is evident that the wall stress data show a phase lead relative to the wavecrest. Fitting the data with a two-harmonic Fourier series, Frederick (1986) finds a phase of 51° for the dominant first harmonic. The LES shows a slightly smaller phase shift of approximately 45°. These results are consistent with theoretical models, e.g. Hunt *et al.* (1988) and Sykes (1980) and reflect the fact that the maximum perturbation velocity near the surface is shifted upstream (Newley 1986). The shear stress perturbation is not exactly symmetric: the increase just ahead of the wave crest is of larger magnitude than the decrease that occurs just upwind of the trough. Accordingly, the low stress region around the trough is of somewhat greater extent than the high stress region.

6. Separated flow over a large-amplitude wavy surface

We now turn to the BHA configuration, $2a/\lambda = 0.2$, that exhibited a large separated region extending over most of the wave trough. There is some uncertainty in the definition of the bulk velocity used in BHA. They give a definition that is a function of position, which seems like an unnecessary complication. On the other hand, Buckles (1983) uses a bulk velocity with a normalizing depth equal to the minimum channel depth, $H - 2a$, rather than the mean channel depth. That is also consistent with integrals of the tabulated velocity profiles given in Buckles (1983) and used here for comparison with the LES. Therefore, for this section only, we use a definition of bulk velocity given by

$$U_b = (H - 2a)^{-1} \int_h^H \bar{u} dz$$

Note that using this definition gives a Reynolds number 12% higher compared with that obtained with the bulk velocity definition (17). This discrepancy is reflected in the Reynolds numbers given in Tables 2 and 3.

6.1. Mean velocity and streamlines

Profiles of the mean streamwise velocity for the simulations BHA1 and BHA1R are compared with the experimental data in Figure 13. Clearly, both the measurements and the LES show strongly separated flow. The predicted magnitude of the reversed flow in the recirculation zone, roughly between $x/\lambda = 0.1$ and 0.7, tends to be slightly greater than observed, but overall the profile variations along the wave are faithfully reproduced. Some locations show an underprediction in the middle of the channel, but this appears to be due to variations in the measurements. We note that the profiles reported by BHA contain discrepancies of up to 3% in the integrated mass flux, which is necessarily conserved in the LES.

Profiles at the crest, trough and two intermediate positions are shown on a log scale in Figure 14 to emphasize the near surface region. The LES profiles (only BHA1R is shown since BHA1 is very similar) are in reasonable agreement with the measured data. In particular, they match well over the crest except for a slight underprediction very close to the surface. Significant shear can be seen very close to the surface at the crest. Above this, the velocity profile is nearly constant for a short while before increasing to the channel centerline maximum. The LES overpredicts the reverse flow in the trough, but shows better agreement on the up- and downslope locations. Note that the LES profiles show slightly negative velocity at $x/\lambda = 0.7$ while the measurements are slightly positive, indicative of a somewhat further downstream reattachment point in the LES.

The mean streamwise velocity field and streamlines are shown in Figure 15 for BHA1R. (The results for BHA1 are similar.) The strong shear over the crests is clearly shown, but it should also be noted that there is still significant shear centered more or less around the $\Psi = 0$ streamline. The recirculation zone, bounded by the $\Psi = 0$ streamline and the wave surface, is somewhat deeper than that shown in BHA (their Figure 5); the bounding streamline has a maximum elevation approximately 90% of the wave height compared with 60% in BHA. Although the LES velocity profiles agree well with the observations over the bulk of the recirculation zone, the overprediction of the reverse flow near the surface results in the integral defining the streamlines, namely, $\Psi = \int_h^z \bar{u} dz'$, going to zero at a greater height.

A detailed examination of the LES and experimental data shows some discrepancy in the precise extent of the recirculation region. Separation (in the mean flow) occurs at $x/\lambda = 0.14$ in the experiment compared with 0.06 for both BHA1 and BHA1R; reattachment occurs at 0.69 in the experiment and at 0.73 and 0.75 for BHA1 and BHA1R respectively. Since the

experimenters note that velocity measurements are inaccurate very close to the surface (below $z/\lambda \approx 2.6 \times 10^{-3}$), there is some uncertainty in the precise locations of the mean separation and reattachment points. Nonetheless, this discrepancy has little adverse effect on predicting the salient features of the mean flow.

6.2. Intermittency and flow variability

It is suggested in BHA that the location of the zero mean streamwise velocity contour corresponds closely with the loci of 50% instantaneous reverse flow, i.e., $\gamma = 0.5$ where the intermittency γ is defined as the fraction of time that u is positive. This is clearly confirmed for the LES in Figure 15, where the $\gamma = 0.5$ line originates very close to the separation point and terminates very close to the point of reattachment, as in BHA. The $\gamma = 0.1$ contour indicates that there is a significant fraction of reverse flow at the top of the mean recirculation zone, i.e., at approximately the height of the wave crests. The location of this line matches well that shown in BHA, although they note that it falls surprisingly high above the recirculation zone. This is not the case with the LES due to its deeper recirculation zone.

The intermittency contours imply large variability in the flow associated with the recirculation zone. Plots of instantaneous velocity fields, examples of which are shown in Figure 16, indicate that large-scale flow features are responsible for this variability. Clearly, flow separation results in large-scale "flapping" of the shear layer as well as other complex behavior. For example, the character of the flow is strikingly different in each of the four troughs shown in Figure 16. In one case, reverse flow fills most of the "valley" above the trough while, in another, reverse flow is confined to a shallow region near the wave surface. In a third case, reverse flow seems to have been ejected away from the surface. Finally, we see a number of small areas, typically on the downslope, where the reverse flow appears to have separated so that there is forward flow very near the surface. It is clear from these examples that the mean streamlines are not at all representative of the instantaneous flow, but they do illustrate the region where recirculating flow is likely to be observed.

6.3. Higher-order statistics

The relative streamwise turbulent fluctuations are shown in Figure 17, where it can be seen that the LES results are in close agreement with the data. Only the total fluctuation intensities are plotted since the subgrid components are almost negligible everywhere. BHA1R profiles are

in close agreement with those of the lower resolution BHA1; there are slight differences in some details, but statistics for the two resolutions differ by less than a few percent.

The highest fluctuation intensities are associated with the free shear layer that detaches from the surface at the separation point and is elevated above the separation zone. The magnitude of this maximum intensity remains fairly constant over much of the wave. A reduction is seen after the flow reattaches and speeds up as it approaches the wave crest. These features can be seen more clearly in Figure 18, where turbulence intensity fields are shown for the three coordinate directions. The locus of maximum streamwise intensity extends over most of the trough at a height equal roughly to the maximum wave height, before elevating somewhat towards the crest. This locus approximately coincides with the midpoint of the vertical shear region in the mean velocity field (see Figure 15(a)). The vertical extent of this free shear layer is evident from the "elbows" in the mean velocity profiles of Figure 13, particularly for $x/\lambda = 0.3$ and 0.5 . The magnitude of the maximum streamwise intensity increases rapidly from a value of about 0.20 very close to the crest to around 0.25 a quarter of the wavelength downstream.

As discussed in BHA, remnants of the free shear layer separating from the upstream wave are manifested as an elevated ($z/H \approx 0.25$ to 0.35) region of increased streamwise turbulence intensity over the wave crest. It can be viewed simply as a continuation of the locus of maximum intensity mentioned above though a periodic domain. However, this elevated maximum decays rapidly downstream of the crest.

A moderate increase in the vertical fluctuation intensity, σ_w , above the wave crest may also be associated with the shear layer remnant. However, the maximum intensity occurs over the trough and is probably related to the large-scale eddies responsible for the variations of the separated flow, as illustrated in Figure 16.

Unlike σ_u and σ_w , the transverse fluctuation intensity, σ_v , does not show any particular feature associated with the free shear layer. However, there is a very pronounced maximum near the surface on the wave upslope whose effects extend over the downstream crest. This is a feature which seems characteristic of all wavy surface cases that we have examined. Since it is rather unexpected and, to our knowledge, has not been observed experimentally, we will discuss it further in Section 9.

The contour plots of streamwise and vertical turbulence intensities in Figure 18 appear qualitatively similar to those shown in Hudson *et al.* (1996) for separated flow over a smaller wave ($2a/\lambda = 0.1$) at a lower Reynolds number ($Re = 3380$). In fact, the locations and even the

magnitudes of the maximum observed intensities are reasonably close to the LES predictions. Hudson *et al.* correlate the different locations of σ_u and σ_w maxima with the different direct production terms (involving the Reynolds stresses and mean velocity gradients). They also point out that the lag in vertical intensity maximum relative to the streamwise intensity is consistent with the initial direct production of streamwise fluctuations (through $\overline{u'w'} \partial \bar{u} / \partial z$ and $\overline{u'^2} \partial \bar{u} / \partial x$) and the subsequent transfer of energy into vertical fluctuations via the pressure-strain term.

Hudson *et al.* also show contours of the Reynolds stress $-\overline{u'w'}$, which again is in qualitative agreement with the LES results shown in Figure 18. It can be seen that the elevation of the maximum Reynolds stress is very close to that of maximum σ_u and is clearly associated with the separated shear layer. The negative values close to the surface on the upslope are an artifact of the Cartesian coordinate system (Hudson 1993); they assume positive values if rotated into a boundary-layer or streamline coordinate system.

Profiles of skewness and flatness of the streamwise velocity, defined as $S = \overline{u'''^3} / \sigma_u^3$ and $F = \overline{u''''^4} / \sigma_u^4$, respectively, are compared with the BHA data for $x/\lambda = 0.3$ in Figure 19. The agreement between the LES profiles and the measurements is encouraging considering the difficulty in obtaining reliable higher-order statistics. Away from the wall, the profiles do not differ greatly from those computed or measured previously over a flat wall, e.g., Moin and Kim (1982). The mid-channel values of $S \approx -0.4$ and $F \approx 3$ are close to the flat channel values and result from velocity fluctuations produced by slow-moving fluid arriving from the wall region. However, the profiles clearly differ from flat channel flow near the wall. For instance, S decreases from its maximum, which is associated with the elevated shear layer, to a small negative value at the wall. In contrast, the flat channel profile of skewness maximizes at the wall. This is also true for flatness. However, for the BHA flow, F shows some rather complex behavior close to the wall, particularly around $(z-h)/H \approx 0.05$. While not inconsistent with the measurements, it remains to be seen if this is real or an artifact of the LES model. The LES profiles do show some sensitivity to resolution, especially for F near the wall. This is not surprising since only the resolved velocity fluctuations are considered.

Contour plots of skewness and flatness are shown in Figure 20. It can be seen that a region of high skewness occurs just downstream of the crest, reaching its maximum around the separation point. The locus of the maximum skewness seems to follow approximately along the middle of the recirculation zone. Large negative values of skewness are seen very close to the wave surface over the region of reverse flow while near-surface positive skewness seems to be associated with attached, forward-moving fluid. Both observations are consistent with the view that velocity fluctuations near the wall are caused by fast-moving fluid being mixed down from

above. But, the skewness is then necessarily negative in the reverse flow region. The region of high flatness is closely correlated with the region of high skewness, suggesting that the process of mixing faster-moving fluid to the wall is intermittent.

6.4. Surface pressure and shear stress

The final comparisons with BHA are of the pressure and shear stress on the wavy surface. An accurate prediction of these quantities is clearly an important aspect of LES since they determine the integrated forces on the wave, which is of interest in aeronautics, oceanography, meteorology and other fields. Variations of the pressure force with slope are discussed in Section 8; here we focus on the BHA configuration.

Figure 21 shows distributions of non-dimensional wall pressure p_w and shear stress τ_w compared with the experimentally measured distributions, where

$$p_w = \left(\frac{U_b^2}{2} \right)^{-1} \bar{p}|_{\eta=0} \quad \text{and} \quad \tau_w = \left(\frac{U_b^2}{2} \right)^{-1} \bar{\tau}_0$$

The pressure plots have been adjusted so that the LES and observations match at the wave trough. It can be seen that both BHA1 and BHA1R predict the pressure increase on the upslope quite well. However, the magnitude of the pressure trough at the wave crest is under-predicted in both cases and some sensitivity to resolution is evident. The wall shear stress is generally well predicted although the phasing of the peak stress lags somewhat compared to the experiment. Note that the experimental surface shear stress was estimated by assuming a linear velocity profile from the lowest measurement point to the wall and there is some uncertainty associated with these measurements.

The total forces on the lower wall per unit area in the x -direction can be calculated by integrating the curves in Figure 21. Defining the non-dimensional pressure and shear stress forces (per unit length) as

$$F_x = -\frac{2\pi a}{\lambda} \int_0^1 p_w \left(\frac{x}{\lambda} \right) \sin \left(2\pi \frac{x}{\lambda} \right) d \left(\frac{x}{\lambda} \right) \quad (19)$$

$$T_x = \int_0^1 \tau_w \left(\frac{x}{\lambda} \right) d \left(\frac{x}{\lambda} \right) \quad (20)$$

the experimental values are $F_x = 0.0261$ and $T_x = 0.0028$. This compares with $F_x = 0.0253$ and 0.0265 for BHA1 and BHA1R, respectively; the corresponding results for the shear stress are $T_x = 0.0016$ and 0.0014 . The accurate prediction of the pressure force, commonly called the

form drag, is due almost entirely to the fact that the pressure rise in Figure 21 matches the data well. The under-prediction of the pressure trough is not critical to the integrated force in the x -direction since the local pressure force there acts vertically. However, the predicted shear stress force is significantly lower than the experimental observations because the biggest discrepancy occurs on the upslope (which is opposite to what we just noted for the pressure distribution). This discrepancy stems from an underprediction of the acceleration on the upslope and the resulting delayed flow reattachment. Although the difficulty in measuring velocity close to the surface may be a factor in the discrepancy, in any case, the magnitude of the shear stress component is small compared with the pressure contribution, so the total drag force is reasonably well predicted by the numerical simulation.

7. Variations with slope

The LES model has been used to examine the effects of varying wave slope. Figure 22 shows mean streamwise velocity profiles for $2a/\lambda = 0.05, 0.10$ and 0.20 (cases S2, S3 and BHA1 in Table 1). It is evident that the mean flow separates for $2a/\lambda = 0.1$ but the 0.05 case is marginal in this regard. Other profile locations (not shown) between $x/\lambda = 0.3$ and 0.5 reveal that case S2 does show a very small region of flow separation. This finding is consistent with the flow regime map of Kuzan *et al.* (1989), which also indicates that the higher slope cases will show clearly separated mean flow. The depth of the shear region above the trough clearly scales with the wave amplitude. This is also true for the height of maximum streamwise turbulence intensity, shown in Figure 23. The turbulence intensity increases almost linearly with slope, especially away from the wave surface.

Figure 24 shows the variation in surface pressure and shear stress with wave slope. The pressure curves show a definite change in character as slope increases. The small-amplitude wave produces a smooth, slightly asymmetric, curve that is similar to the one shown in Zilker and Hanratty (1979) for this slope, but with a somewhat smaller peak. However, there may be some Reynolds number effect given that the measurements by Zilker and Hanratty are for $Re = 30000$. As slope increases, a nearly constant pressure region over the separated flow becomes more pronounced. The shape of the $2a/\lambda = 0.2$ curve is similar to that in Zilker and Hanratty (as well as BHA), but apparently the LES significantly underpredicts the total pressure perturbation (peak-to-trough). (As we saw above, the $2a/\lambda = 0.2$ case shows good overall agreement with the data of BHA if the predictions and observations are matched in the region of uniform pressure at the trough.) A comparison of the $2a/\lambda = 0.1$ case with the $2a/\lambda = 0.125$ data in Zilker and Hanratty also reveals an underprediction of the pressure perturbation. In this case,

though, the curves are also qualitatively different. As noted above, the LES curve shows evidence of separation by a relatively flat section. However, although Zilker and Hanratty observed separation at this slope, their pressure data do not show a similar feature.

The surface shear stress curves shown in Figure 24(b) clearly illustrate the regions of separated or stagnant flow for the three slopes. The shear stress for $2a/\lambda = 0.05$ is nearly symmetric (implying very little contribution to the increase in total surface force) and becomes slightly negative approximately from $x/\lambda = 0.2$ to 0.5. In light of the velocity profiles in Figure 22, it is evident that the flow here is only weakly separated and is probably better characterized as stagnant. The region of negative shear stress clearly increases with slope, as does the magnitude of the negative stress. The local maxima both $2a/\lambda = 0.1$ and 0.2 cases exhibit around $x/\lambda = 0.3$ is rather surprising, but results from a small reduction in the magnitude of the reverse flow there. Since measurements of surface shear stress are somewhat unreliable, we cannot ascertain if this feature is realistic. Because the reattachment point (the second zero stress crossing) moves downstream with increasing slope, the subsequent rate of increase in shear stress tends to be greater, although the location of the maximum also tends to move downstream slightly.

The pressure curves in Figure 24(a) certainly show significant variations with slope. However, probably of greater interest than the curves themselves is the resulting integrated force on the wave surface, especially as a function of slope. This is examined in the next section.

8. Form drag calculations

In this section, we present LES calculations of form drag for a number of wave slopes; see Table 1 for a summary of cases. These calculations include some variations with resolution and Reynolds number since the results may be somewhat controversial and we want to establish the sensitivity and consistency of the numerical calculations.

Figure 25 shows the variations in form drag as a function of slope. In comparing with the data of Zilker and Hanratty, as is done in Belcher *et al.* (1993) and Gong *et al.* (1996), we found that the LES form drag predictions were approximately twice as large as the reported values. However, we checked the Zilker and Hanratty results by integrating the corresponding pressure curves as presented in their paper. As seen from Table 3, the numerically integrated forces are around twice the values stated in Zilker and Hanratty and are reasonably consistent with the LES results as well as the measurements of BHA. These calculations are shown in Figure 25 as the solid symbols. We have employed this method on the data of BHA and get very close agreement

with the reported form drag (within 6%). We also show the form drag derived from the pressure data presented in Buckles *et al.* (1986) for $2a/\lambda = 0.125$ ($Re = 12300$), although they do not give their own calculated value. The form drag in this case appears to be quite high, being roughly equal with the $2a/\lambda = 0.2$ value, although not that much higher than the numerically integrated Zilker and Hanratty result for $Re = 14730$. This suggests there may be some dramatic change in the nature of the flow at this slope, possibly with some Reynolds number dependence, or it may point out some difficulties and uncertainties in the measurements. Note that the measurements of Gong *et al.* are still in reasonable agreement with the adjusted values of Zilker & Hanratty, particularly if the normalization in Gong *et al.* is corrected for the fact that the centerline velocity is approximately 20% larger than the bulk velocity. However, the predictions in Belcher *et al.* appear to be much lower than the adjusted Zilker and Hanratty forces as well as those of BHA and the LES in this study.

We have examined sensitivity to resolution, domain length and Reynolds number for $2a/\lambda = 0.2$. As can be seen from the figure and Table 3, the form drag calculated from the LES appears to be relatively insensitive in the range of Reynolds numbers considered. This is in contrast to Zilker and Hanratty, especially for the numerically integrated pressure forces, although there is certainly some question as to the reliability of these force results.

It should be pointed out that the LES results are subject to some uncertainty since they depend entirely on modeling the flow near the surface where, as has been shown, the explicit resolution of the turbulent motions is effectively reduced. However, the effective resolution increases with slope since larger-scale motions are generated and the form drag predictions are self-consistent in that a quadratic dependence on slope is shown over a range of amplitudes, i.e., a good fit is given by

$$F_x = 0.12(ak)^2$$

This relationship appears to be valid up to around $2a/\lambda = 0.1$; it starts to fall off as slope and hence separation increases. This behavior is consistent with theoretical expectations, e.g. Wood and Mason (1993).

Reference	$2a/\lambda$	Re	F_x	$\lambda^{-1} \int_0^\lambda p_w \frac{dh}{dx} dx'$
Zilker & Hanratty (1979)	0.05	29300	1.26×10^{-3}	2.89×10^{-3}
	0.125	14730	1.155×10^{-2}	2.29×10^{-2}
	0.125	30000	1.003×10^{-2}	1.64×10^{-2}
	0.20	30530	1.37×10^{-2}	2.56×10^{-2}
Buckles <i>et al.</i> (1986)	0.125	12300	—	3.08×10^{-2}
BHA	0.20	10700	3.27×10^{-2}	3.46×10^{-2}
LES – S1	0.031	6560	—	1.24×10^{-3}
S1R	0.031	5720	—	1.31×10^{-3}
S2	0.05	11050	—	2.90×10^{-3}
S3	0.10	10580	—	1.29×10^{-2}
S4	0.125	10800	—	1.70×10^{-2}
BHA1	0.20	10600	—	3.16×10^{-2}
BHA1R	0.20	10450	—	3.34×10^{-2}
BHA1L	0.20	12000	—	3.21×10^{-2}
BHA2	0.20	5990	—	3.20×10^{-2}
BHA3	0.20	20060	—	3.19×10^{-2}

Table 3. Form drag for various wave slopes and Reynolds numbers. F_x is the normalized form drag given in the cited references; the last column is the form drag computed using published surface pressure data (calculated by the present authors). Note that the values for BHA and Buckles *et al.* (1986) are scaled by $(H-a)^2/(H-2a)^2$ so they are consistent with U_b defined by (17).

9. Increased transverse fluctuations

As shown in Figure 18, the transverse fluctuations, $\overline{v'^2}$, show a marked increase on the upslope close to the wave surface. In fact, the largest velocity fluctuations are found in the lateral component, exceeding even the streamwise component maximum, located in the separating shear layer. A similar feature has recently been reported by De Angelis *et al.* (1997) and Cherukat *et al.* (1998) in their DNS studies of flow over waves with smaller slopes, although not as pronounced as in Figure 18. The magnitude and limited spatial extent of the $\overline{v'^2}$ increase strongly suggests a localized energy production mechanism associated with the wave slope and we, therefore, investigate the lateral velocity fluctuations in more detail.

An examination of instantaneous flow fields at $\eta/\lambda = 0.025$, such as that shown in Figure 26, indicates structures elongated in the streamwise direction; they are most easily seen in the transverse velocity field. However, they do not resemble the streaks seen in flat boundary layers: these are broader laterally and limited in streamwise extent. These broad areas of coherent transverse velocity are also evident in a plot of the secondary flow vectors at $x/\lambda = 0.75$, Figure 26(c). There are intense vortex-like transverse motions close to the surface, but they do not seem to be clearly defined closed circulations or streamwise rolls.

The velocity fluctuations associated with these intense transverse velocity regions are strongly affected by the presence of the solid boundary, since they occur so close to the wall. This most likely is the reason for the preferential manifestation of the kinetic energy in the v -component, rather than equally amongst v and w . For a streamwise vortex, an idealized reflective boundary condition at the wall reduces the normal component of the velocity to zero and doubles the transverse velocity component, giving a strong enhancement of $\overline{v'^2}$ at the surface. The wall layer drag reduces the velocity very close to the surface, but the large increase in $\overline{v'^2}$ on the lower side of the vortex-like structures is clearly evident in the LES results.

The persistence of these structures is illustrated in Figure 27, which shows the transverse velocity component at $x/\lambda = 0.75$ and $\eta/\lambda = 0.0125$ as a function of time and transverse position. Examples from BHA1 and the flat channel case F are shown. It can be seen that the flat channel contours are rather isotropic in appearance, indicating an intermittent flow structure that is not strongly correlated in time or along the transverse direction. In contrast, the contours for the wavy channel midway on the upslope show broad streaks of positive or negative velocity. Although these features meander laterally and the magnitude of the v -velocity in the streak is modulated over time, the identity of the structure is maintained throughout, providing strong evidence of their stability.

Both De Angelis *et al.* (1997) and Cherukat *et al.* (1998) suggest that the transverse velocity fluctuation increase is produced by the large-scale structures associated with flow separation and reattachment. This is not necessarily the case. Although the $\overline{v'^2}$ maximum is localized near the reattachment point over the large-amplitude wave, LES of flow over smaller wave slopes also show a similar feature on the wave upslope. Figure 28 shows the transverse fluctuation intensities for the three waves considered in Section 8. Note that the maximum on the upslope is present for all waves, including the smallest slope that exhibits very weak separation. (The mean reattachment point in that case is at $x/\lambda = 0.5$, well upstream of the $\overline{v'^2}$ maximum.).

Figure 29 shows the transverse variance perturbation for case S1R, as was done for the streamwise and vertical components in Figure 10. It can be seen that for a small-amplitude wave, a noticeable increase in $\Delta v'^2$ on the upslope is evident, but it is accompanied by an almost equal decrease on the downslope. (However, an examination of the larger-amplitude waves reveals that this near anti-symmetry breaks down as slope increase so that the magnitude of the upslope (positive) perturbation becomes much larger than the magnitude of the downslope (negative) perturbation.) In contrast to Figure 10, there is little qualitative agreement with closure model predictions.

The perturbation maximum in Figure 29 is close to the surface and thus is influenced by the subgrid model, but Figure 11 shows that at least 75% of the transverse variance is resolved at that location. Also, the fraction of resolved variance increases with slope (not shown), so results should be more reliable for the the larger-amplitude cases.

The results shown in Figure 28 indicate that $\overline{v'^2}$ increases with wave steepness. To quantify this, we examine the normalized maximum perturbations for the streamwise and transverse variances as functions of wave slope, given in Table 4. It can be seen that $\Delta \overline{u'^2}$ scales closely with slope for small-amplitude waves, in accord with linear theories (Sykes 1980). However, the $\Delta \overline{v'^2}$ increases suggest a quadratic dependence on slope, with a fall off at larger slopes similar to the form drag.

LES Case	ak	$\Delta \overline{u'^2}/ak$	$\Delta \overline{v'^2}/(ak)^2$
S1	0.098	7.70×10^{-2}	2.41×10^{-1}
S1R	0.098	8.43×10^{-2}	2.50×10^{-1}
S2	0.157	7.91×10^{-2}	1.93×10^{-1}
S3	0.314	9.13×10^{-2}	2.64×10^{-1}
S4	0.393	8.18×10^{-2}	1.86×10^{-1}
BHA1	0.628	8.67×10^{-2}	1.69×10^{-1}
BHA1R	0.628	6.47×10^{-2}	1.34×10^{-1}
BHA1L	0.628	9.55×10^{-2}	1.81×10^{-1}

Table 4. Maximum variance perturbations for LES cases defined in Table 1. The streamwise perturbations are normalized by the wave slope ak ; the transverse perturbations are normalized by the square of the wave slope.

Examination of the conservation equation for $\overline{v'^2}$ shows that, since there are no mean gradients in the lateral direction, direct production terms are zero and the transverse velocity fluctuations must be driven by the pressure-strain term, $\overline{p' \partial v' / \partial y}$, as pointed out by De Angelis *et al.* (1997). It is well-known that pressure-strain terms redistribute energy from one component to another and this is clearly the case with $\overline{v'^2}$: energy from the streamwise and/or vertical components are extracted through the correlation between pressure perturbations and transverse velocity gradients. The proximity of the wall is certainly a factor, as mentioned above, but the basic mechanism that gives rise to this correlation is unknown. It may be due to amplification of some flow instability, but it is not related to the large-scale shear instability described in Phillips *et al.* (1996) and possibly observed in the experiments of Gong *et al.* (1996), since that mechanism has a streamwise scale greater than the wavelength. The increased $\overline{v'^2}$ we observe is much more limited in extent. A possible mechanism is the Taylor-Görtler instability which produces streamwise vortices such as observed in boundary layer flow over a concave surface, e.g., Tani (1962), So and Mellor (1975) and Hoffman *et. al.* (1985). The trough region presents a concave surface, and we might therefore expect production of coherent streamwise vortices in the local flow. However, the magnitude of the $\overline{v'^2}$ increase observed in the LES calculations appears to be significantly larger than experimental observations in curved boundary layer flow, but this may be due to enhancement by the shear distortion in the flow over the waves. Experimental flows have generally involved minimal streamwise acceleration in an attempt to isolate the curvature mechanisms. In contrast, the vorticity production in flow over waves occurs in a region of strong acceleration and, hence, vortex stretching. Streamwise vorticity is therefore enhanced as the flow accelerates toward the wave crest, increasing the v -velocity and also stabilizing any existing vortices.

10. Conclusions

Large-eddy simulations of flow over a wavy surface have been presented and compared with available experimental data at Reynolds numbers of about 10^4 . The viscous effects are only important close to the smooth wall, and the LES grid size normal to the wall is chosen to resolve the viscous sublayer. A range of wave amplitudes has been studied, from small slopes with almost linear flow perturbations up to steep waves with large-scale flow separation. Particular attention has been paid to the large amplitude wave experiment of BHA.

In spite of the fact that surface elevation variations are known to induce complex distortion of the turbulence fields close to the surface, the moderate resolution of the LES appears sufficient to capture many aspects of the experimental flow. This is partially due to the fact that the

streamwise velocity fluctuations, often the only component measured in the laboratory, are relatively well resolved in the LES. Nevertheless, the response of the mean flow and the streamwise velocity variance to different wave amplitudes is accurately predicted even close to the surface.

Small amplitude waves illustrate the nature of the perturbations, and confirm the turbulence closure model predictions of an "inner layer" structure between the wall-layer and the outer flow on the scale of the horizontal wavelength. The LES results show rapid variation in the velocity variances within a layer of about 5% of the wavelength; this is generally consistent with closure theory predictions but quantitative comparison is precluded by the log-layer assumption of the analytical models.

At large amplitude, the flow is dominated by the separating shear layer which generates large-scale eddies, allowing more of the turbulent energy to be resolved by the LES. The predicted separation region is more extensive than in the experiment, but the turbulence and mean flow fields are only sensitive to this discrepancy very close to the wall. The predicted structure of the streamwise velocity fluctuations, including the higher order statistics of skewness and flatness, is consistent with the experimental data.

A comparison of predicted form drag with experimental observations has pointed out some uncertainties in the observations. In particular, it appears that the drag coefficients reported in Zilker and Hanratty (1979) are inconsistent with their surface pressure distributions. However, the form drag reported in BHA (which is consistent with their surface pressure data) is close to the LES value. The LES results are subject to uncertainty since resolution is effectively reduced near the surface, but they are self-consistent in that the form drag shows a quadratic dependence on slope for small-amplitude waves, as predicted by analytical models. A slight fall off with slope is predicted for larger amplitudes, again consistent with expectations, e.g., Wood and Mason (1993).

One of the most striking features of the numerical calculations is a dramatic increase in lateral velocity variance in a very localized region close to the surface on the upslope of the wave. This is a general feature of all our wavy surface simulations. The increase apparently scales with the square of the slope, in contrast to the other two velocity components, which scale linearly with slope for small amplitude waves. The eddies responsible for the high variance are persistent structures, elongated along the upslope, with relatively large lateral scale. The lateral motions are driven by pressure variations, constrained by the tangential plane of the wall, but the basic mechanism for their generation is unclear. This phenomenon has been observed in the DNS

studies of De Angelis *et al.* (1997) and Cherukat *et al.* (1998), but, as far as we are aware, not measured experimentally, and further investigation is warranted.

Acknowledgement

This work was supported by the U.S. Army Research Office under contract DAAH04-95-G-0041, monitored by Walter J. Bach, Jr.

References

Belcher, S. E. and J. C. R. Hunt (1998), "Turbulent flow over hills and waves", *Annu. Rev. Fluid Mech.*, **30**, 507-538.

Belcher, S. E., T. M. J. Newley and J. C. R. Hunt (1993), "The drag on an undulating surface induced by the flow of a turbulent boundary layer", *J. Fluid Mech.*, **249**, 557-596.

Buckles, J. J. (1983), "Turbulent separated flow over wavy surfaces", Ph. D. Thesis, University of Illinois.

Buckles, J., T. J. Hanratty and R. J. Adrian (1984), "Turbulent flow over large-amplitude wavy surfaces", *J. Fluid Mech.*, **140**, 27-44.

Buckles, J., T. J. Hanratty and R. J. Adrian (1986), "Separated turbulent flow over a small amplitude wave", *Laser anemometry in fluid mechanics - II*, 347-357, ed. R. J. Adrian, D. F. G. Durao, F. Durst, H. Mishina and J. H. Whitelaw, Ladoan, Lisbon.

Cherukat, P., Y. Na, T. J. Hanratty and J. B. McLaughlin (1998), "Direct numerical simulation of a fully developed turbulent flow over a wavy wall", *Theoret. Comp. Fluid Dyn.*, **11**, 109-134.

Clark, J. A. (1968), "A study of incompressible turbulent boundary layers in channel flow", *Trans. A.S.M.E. J. Basic Eng.*, **90**, 455.

Clark, T. L. (1977), "A small-scale dynamic model using a terrain-following coordinate transformation", *J. Comp. Phys.*, **24**, 186-215.

De Angelis, V., P. Lombardi and S. Banerjee (1997), "Direct numerical simulation of turbulent flow over a wavy wall", *Phys. Fluids*, **9**, 2429-2442.

Dörnbrack, A. and U. Schumann (1993). "Numerical simulation of turbulent convective flow over wavy terrain." *Boundary.-Layer Met.*, **65**, 323-355.

Frederick, K. A. (1986), "Turbulent air flow over hills", Ph. D. Thesis, University of Illinois.

Frederick, K. A. and T. J. Hanratty (1988), "Velocity measurements for a turbulent nonseparated flow over solid waves", *Experiments in Fluids*, **6**, 477-486.

Gong, W., P. A. Taylor and A. Dörnbrack (1996), "Turbulent boundary-layer flow over fixed aerodynamically rough two-dimensional sinusoidal waves", *J. Fluid Mech.*, **312**, 1-37.

Henn, D. S. and R. I. Sykes (1992). "Large-eddy simulation of dispersion in the convective boundary layer." *Atmos. Env.*, **26A**, 3145-3159.

Hoffman, P. H., K. C. Muck and P. Bradshaw (1985), "The effect of concave surface curvature on turbulent boundary layers", *J. Fluid Mech.*, **161**, 371-403.

Hudson, J. D. (1993), "The effect of a wavy boundary on a turbulent flow", Ph. D. Thesis, University of Illinois.

Hudson, J. D., L. Dykhno and T. J. Hanratty (1996), "Turbulence production in flow over a wavy wall", *Exps. Fluids*, **20**, 257-265.

Hunt, J. C. R., S. Leibovich and K. J. Richards (1988), "Turbulent shear flow over low hills", *Quart. J. Roy. Met. Soc.*, **114**, 1435-1470.

Hussain, A. K. M. F. and W. C. Reynolds (1970), "The mechanics of an organized wave in turbulent shear flow", *J. Fluid Mech.*, **41**, 241-258.

Hussain, A. K. M. F. and W. C. Reynolds (1975), "Measurements in fully developed turbulent channel flow", *Trans. A.S.M.E. J. Fluids Eng.*, **97**, 568-578.

Krettenauer, K. and U. Schumann (1992), "Numerical solution of turbulent convection over wavy terrain", *J. Fluid Mech.*, **237**, 261-300.

Kuzan, J. D. and T. J. Hanratty (1989), "Turbulent flows with incipient separation over solid waves", *Exps. Fluids*, **7**, 88-98.

Lewellen, W. S. (1977), "Use of invariant modeling", *Handbook of Turbulence*, 237-280, ed. W. Frost and T. H. Moulden, Plenum Press,

Mason, P. J. (1989), "Large-eddy simulation of the convective atmospheric boundary layer", *J. Atmos. Sci.*, **46**, 1492-1516.

Mason, P. J. and N. S. Callen (1986), "On the magnitude of the subgrid-scale eddy coefficient in large-eddy simulations of turbulent channel flow", *J. Fluid Mech.*, **162**, 439-462.

Maaß, C. and U. Schumann (1994), "Numerical simulation of turbulent flow over a wavy boundary", *Direct and Large Eddy Simulation I*, 287-297, ed. P. R. Voke, L. Kleiser and J. P. Chollet, Kluwer.

Maaß, C. and U. Schumann (1996), "Direct numerical simulation of separated turbulent flow over a wavy boundary", *Flow simulation with high performance computers II*, 227-241, ed. E. H. Hirschel,

Moin, P. and J. Kim (1982). "Numerical investigation of turbulent channel flow." *J. Fluid Mech.*, **118**, 341-377.

Newley, T. M. J. (1985), "Turbulent air flow over hills", Ph. D. Thesis, Cambridge University.

Phillips, W. R., Z. Wu *et al.* (1996). "On the formation of longitudinal vortices in a turbulent boundary layer over wavy terrain." *J. Fluid Mech.*, **326**, 321-341.

Schmidt, H. and U. Schumann (1989), "Coherent structure of the convective boundary layer derived from large-eddy simulations", *J. Fluid Mech.*, **200**, 511-562.

So, R. M. C. and G. L. Mellor (1975), "Experiment on turbulent boundary layers on a concave wall", *Aero. Quart.*, **26**, 25-40.

Sykes, R. I. (1980), "An asymptotic theory of incompressible turbulent boundary-layer flow over a small hump", *J. Fluid Mech.*, **101**, 647-670.

Sykes, R. I. and D. S. Henn (1989), "Large-eddy simulation of turbulent sheared convection", *J. Atmos. Sci.*, **46**, 1106-1118.

Sykes, R. I. and D. S. Henn (1992), "Large-eddy simulation of concentration fluctuations in a dispersing plume", *Atmos. Env.*, **26A**, 3127-3144.

Tani, I. (1962), "Production of longitudinal vortices in the boundary layer along a concave wall", *J. Geophys. Res.*, **67**, 3075-3080.

Taylor, P. A. (1977), "Numerical studies of neutrally stratified planetary boundary-layer flow above gentle topography", *Boundary-Layer Met.*, **12**, 37-60.

Walko, R. L., W. R. Cotton and R. A. Pielke (1992), "Large-eddy simulations of the effects of hilly terrain on the convective boundary layer", *Boundary-Layer Met.*, **58**, 133-150.

Wood, N. and P. J. Mason (1993), "The pressure force induced by neutral, turbulent flow over hills", *Quart. J. Roy. Met. Soc.*, **119**, 1233-1267.

Zilker, D. P. (1976), "Flow over wavy surfaces", Ph. D. Thesis, University of Illinois.

Zilker, D. P., G. W. Cook and T. J. Hanratty (1977), "Influence of the amplitude of a solid wavy wall on a turbulent flow. Part 1. Non-separated flows", *J. Fluid Mech.*, **82**, 29-51.

Zilker, D. P. and T. J. Hanratty (1979), "Influence of the amplitude of a solid wavy wall on a turbulent flow. Part 2. Separated flows", *J. Fluid Mech.*, **90**, 257-271.

Figures

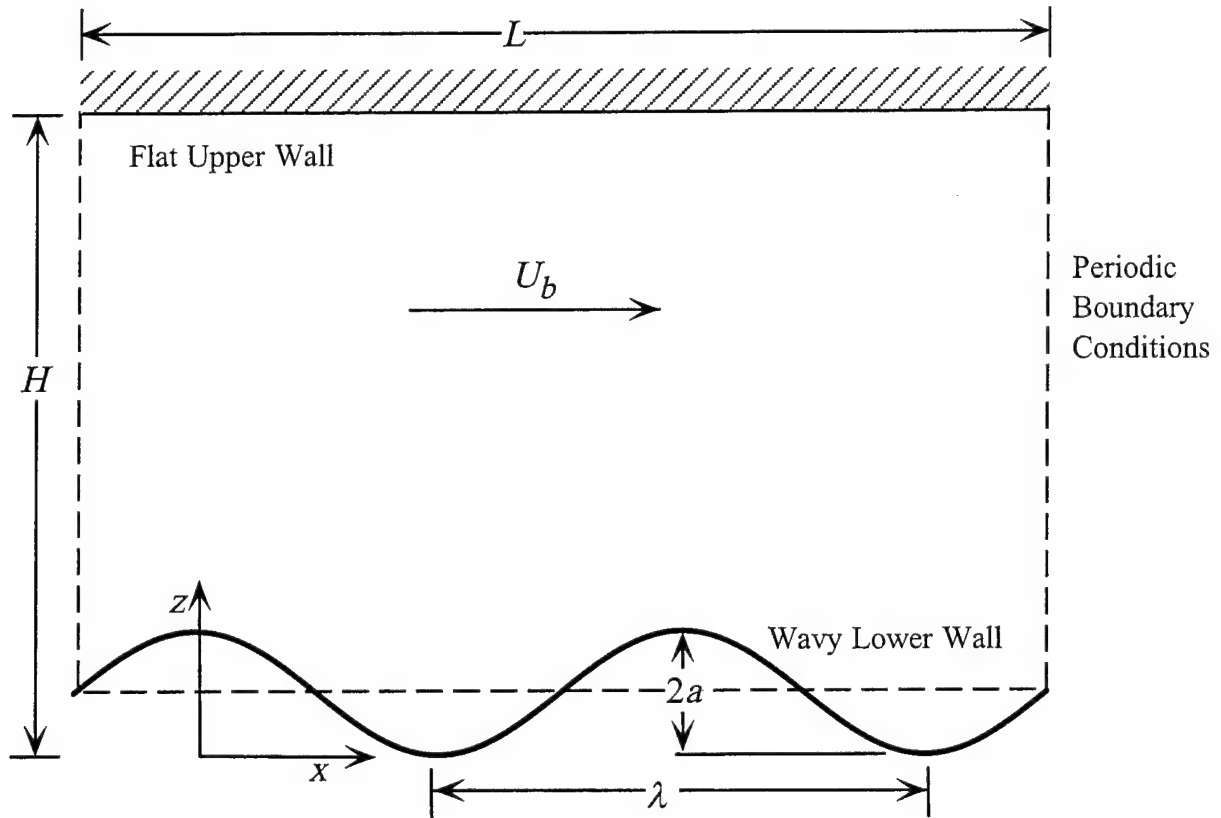


Figure 1. Schematic diagram of channel flow over a periodic wavy lower wall. The maximum channel depth is H ; the LES computational domain has a length L . For most cases with a wavy surface, L is twice the wavelength λ , the transverse computational width, W , is equal to λ and $\lambda \approx H$. For the flat channel cases, $L = 2H$ and $W = H$.

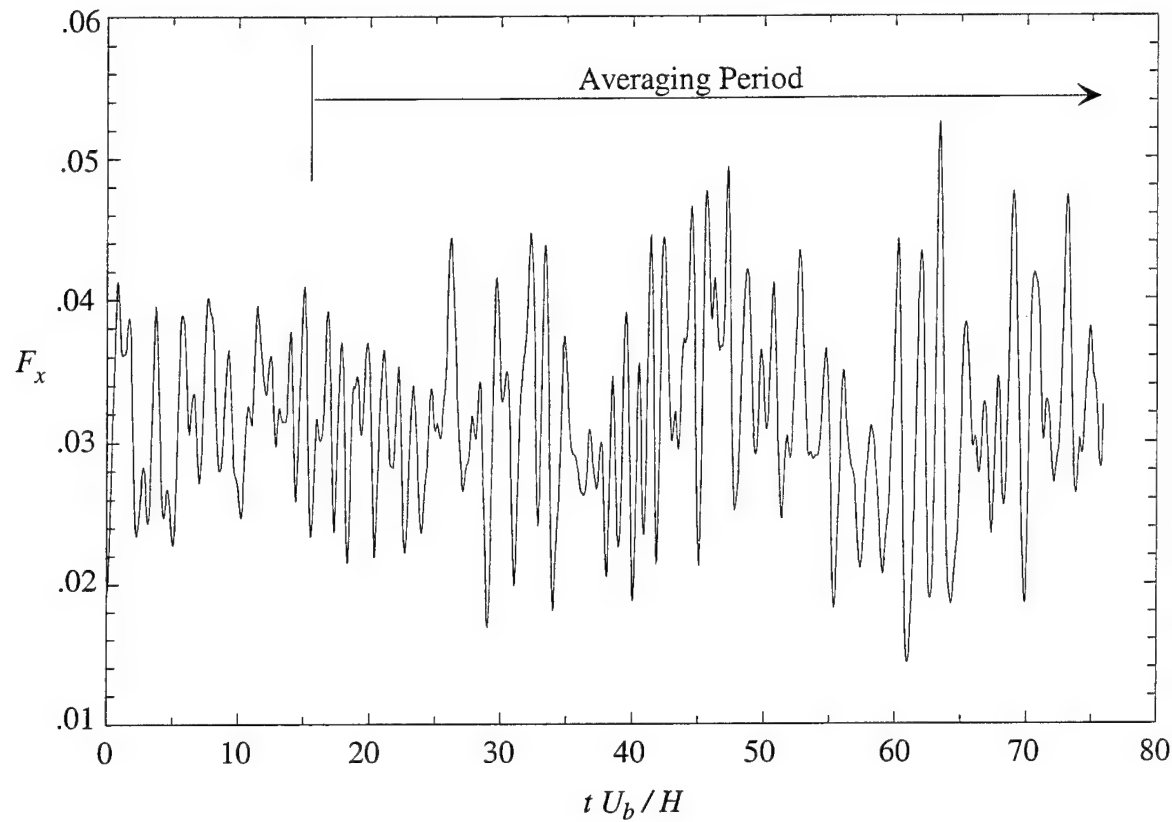


Figure 2. Time-history of integrated surface pressure force or form drag, defined by (19) for case BHA1. The averaging period used to generate steady-state statistics is shown on the figure.

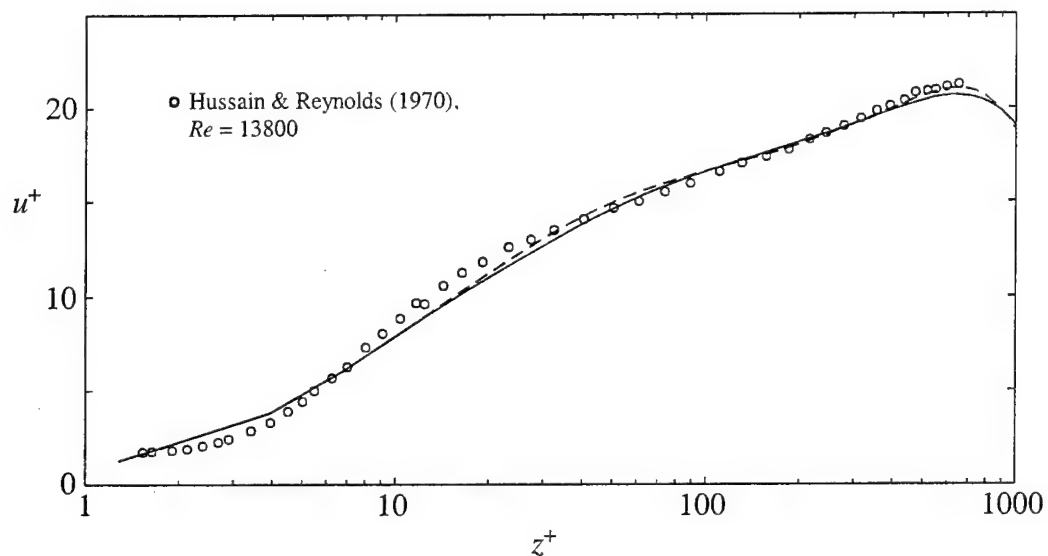


Figure 3. Mean velocity profile for flat channel cases compared with experimental data. Solid lines are standard resolution case F; dashed lines are higher resolution case FR; symbols denote measurements

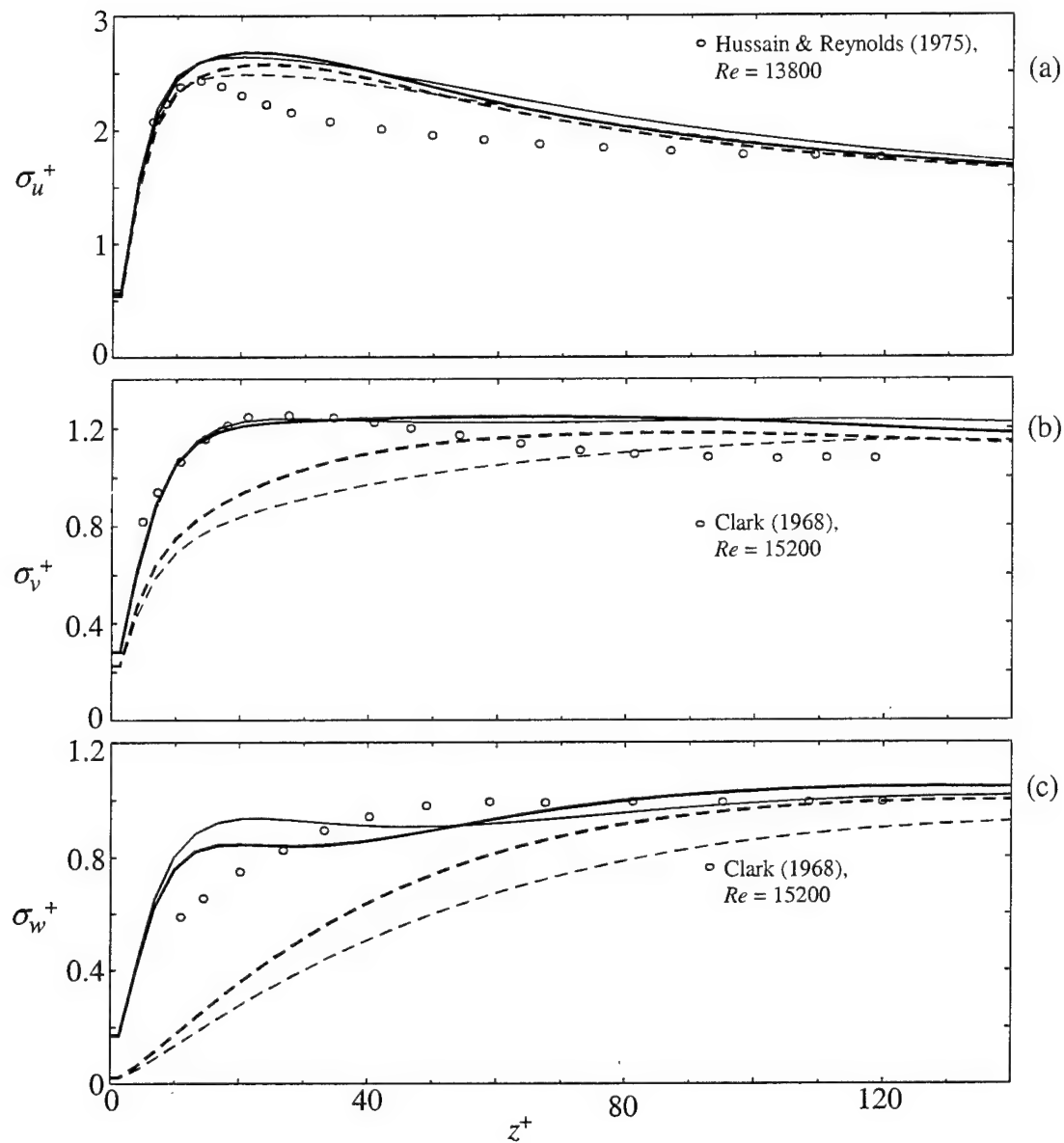


Figure 4. Turbulence intensities for cases F and FR compared with experimental data. The solid lines are the total fluctuations; dashed lines are the resolved components. The high resolution case FR is shown with dark lines. (a) Streamwise turbulence intensity (b) transverse turbulence intensity, (c) vertical turbulence intensity.

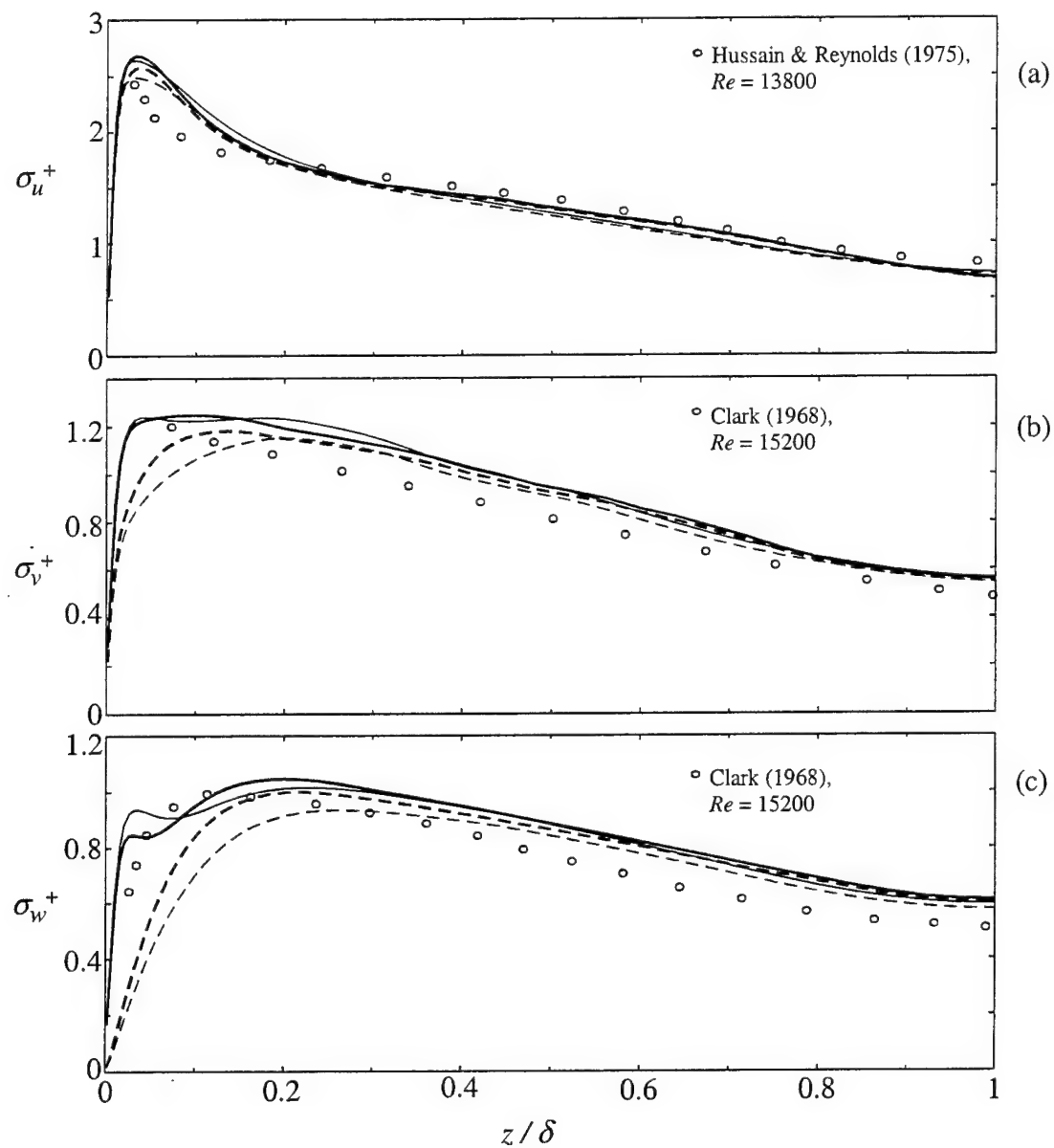


Figure 5. As Figure 4, but height above wall scaled by channel half-depth. (a) Streamwise turbulence intensity, (b) transverse turbulence intensity, (c) vertical turbulence intensity.

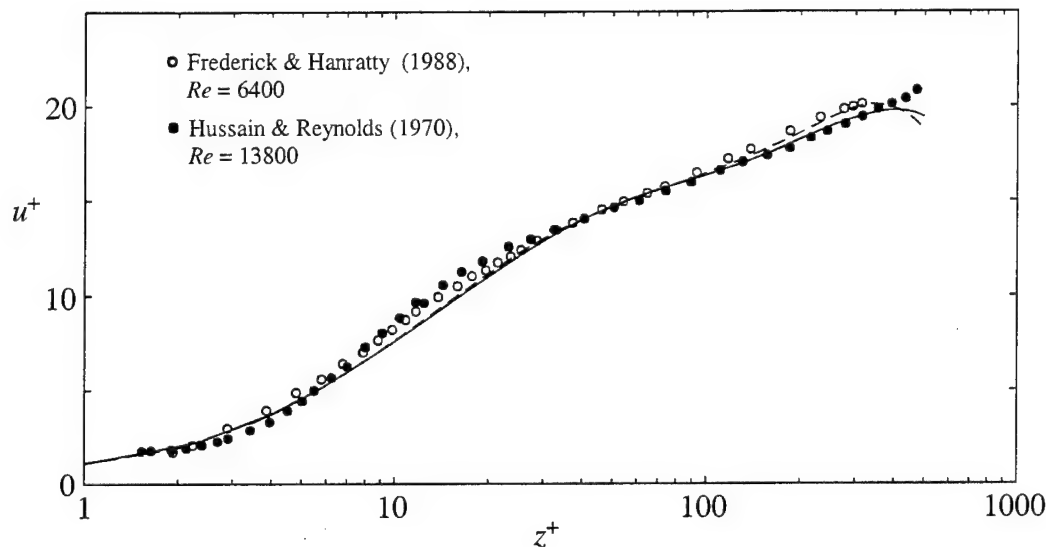


Figure 6. Mean wavelength-averaged velocity profile for cases S1 and S1R ($2a/\lambda = 0.031$) compared with experimental data. The standard resolution case S1 is shown as the solid line; the higher-resolution case S1R is shown as the dashed line; symbols denote experimental data.

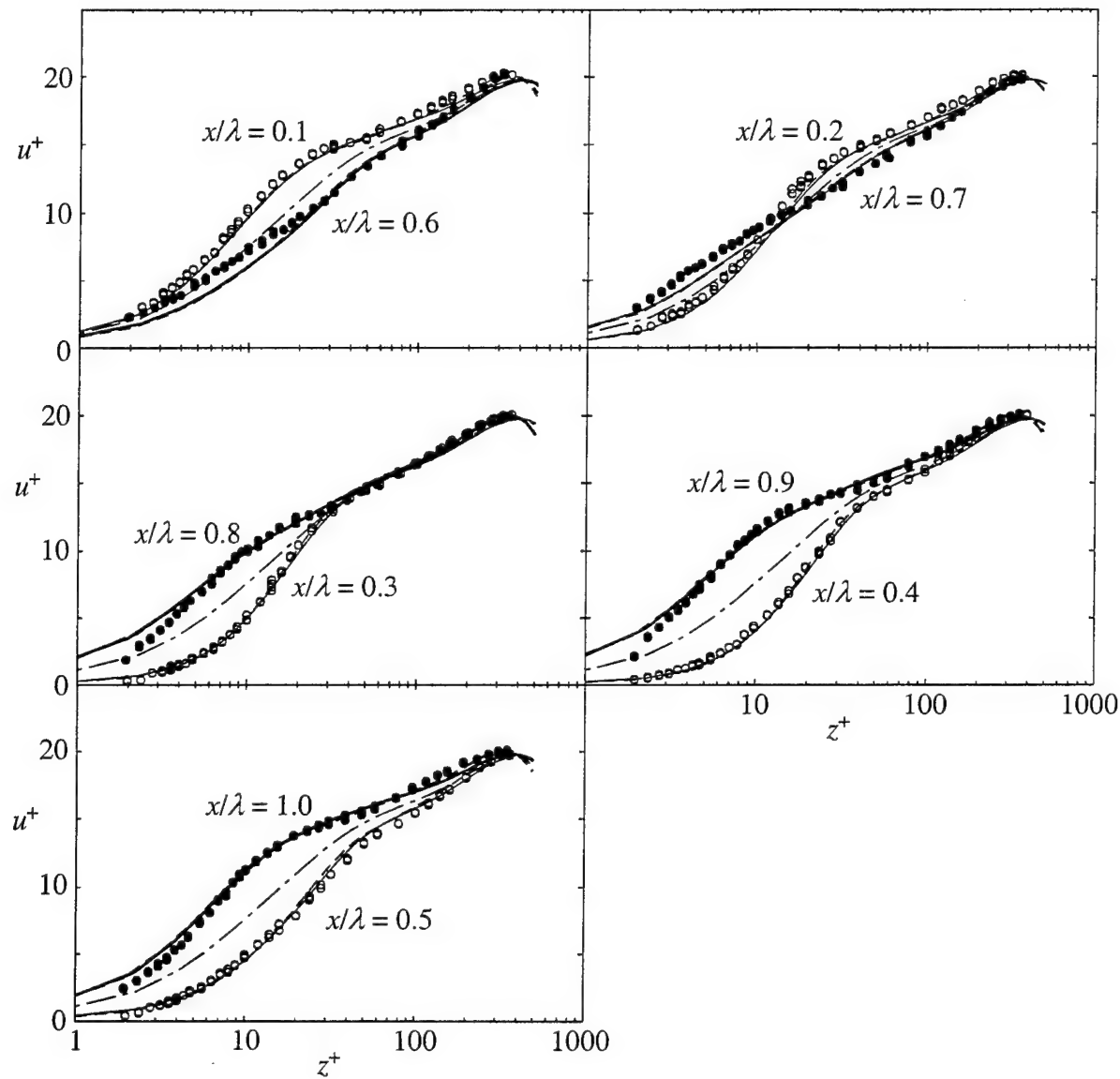


Figure 7. Profiles of mean streamwise velocity at various locations along the surface wave compared with data of Frederick and Hanratty (1988). For the downslope locations $x/\lambda = 0.1$ to 0.5 , thin solid lines are case S1, thin dashed lines are case S1R and open circles are the experimental data. For the upslope locations $x/\lambda = 0.6$ to 1.0 , thick solid lines are case S1, thick dashed lines are case S1R and solid circles are the experimental data. The wavelength average from S1R is shown with the long-dash, short-dash pattern. (The curves from the two LES cases are virtually indistinguishable.)

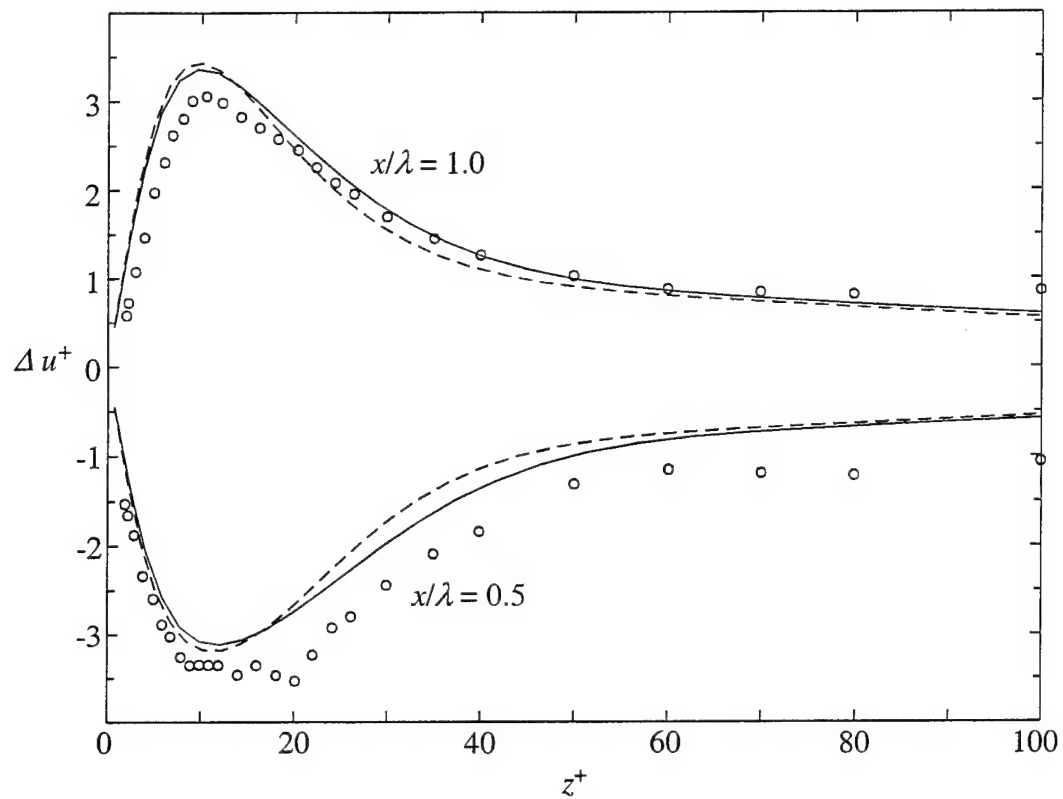


Figure 8. Profiles of mean streamwise velocity perturbation at the wave crest and trough. Solid lines are case S1; dashed lines are S1R; open circles are the experimental data of Frederick (1986).

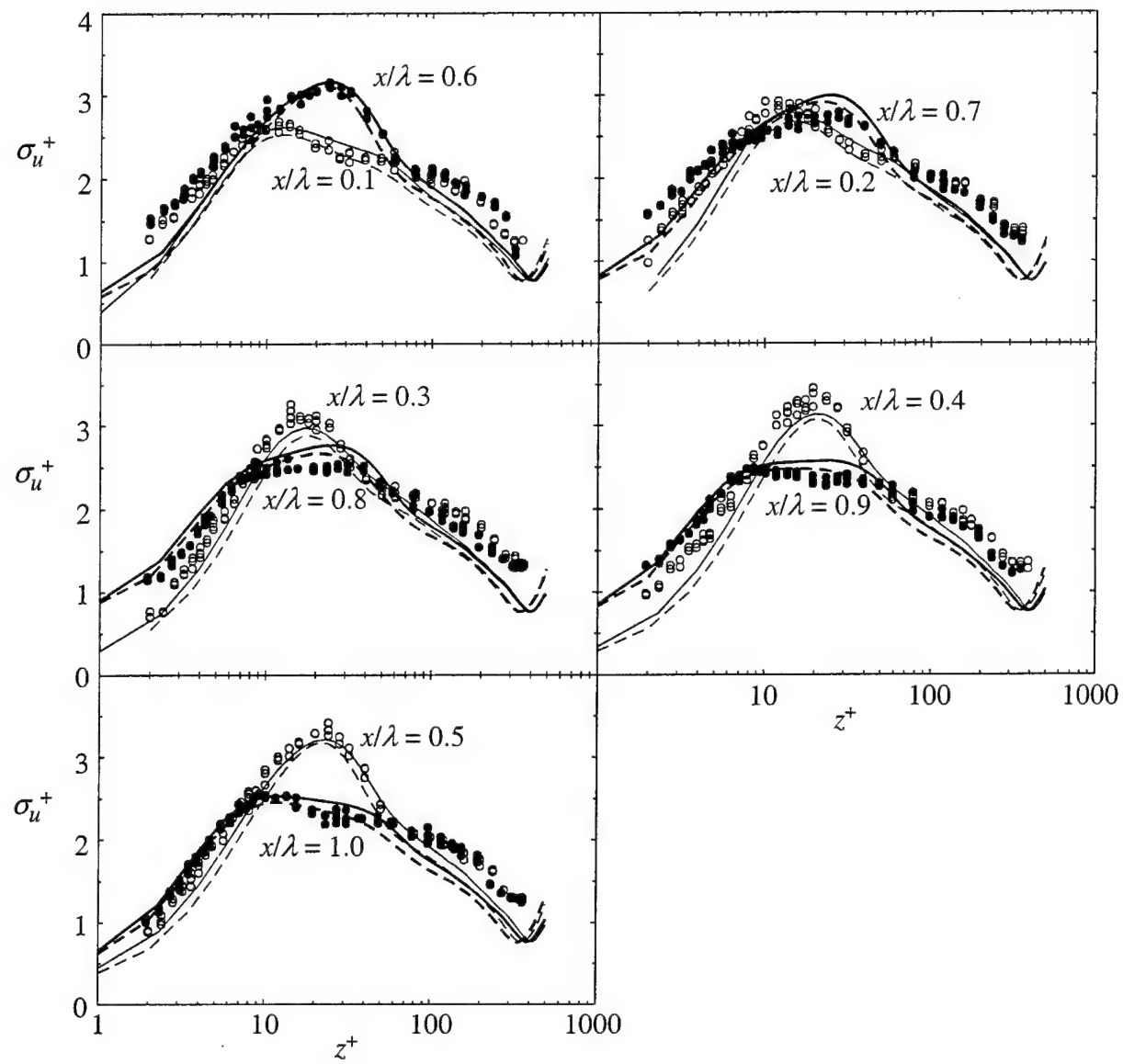


Figure 9. Profiles of mean streamwise turbulence intensities from cases S1 and S1R at various locations along the surface wave compared with the data of Frederick (1986). Line patterns and symbols as in Figure 7 (but the wavelength average is not shown here).

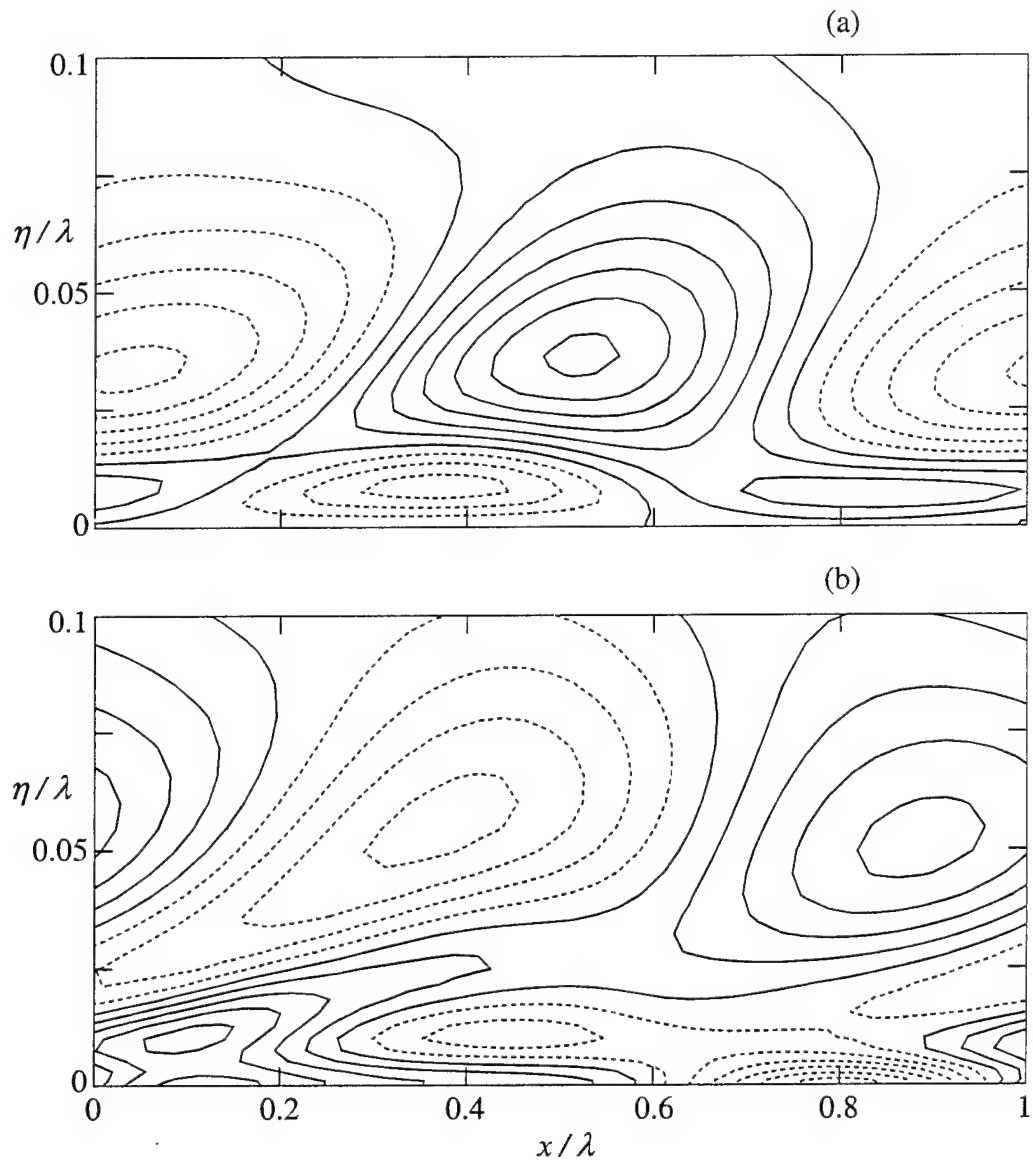


Figure 10. Velocity variance perturbation from the wavelength average, normalized by u_*^2 , for case S1R. (a) Streamwise component; contour interval is 0.4 (b) Vertical component; contour interval is 0.04. Dashed lines indicate negative values.

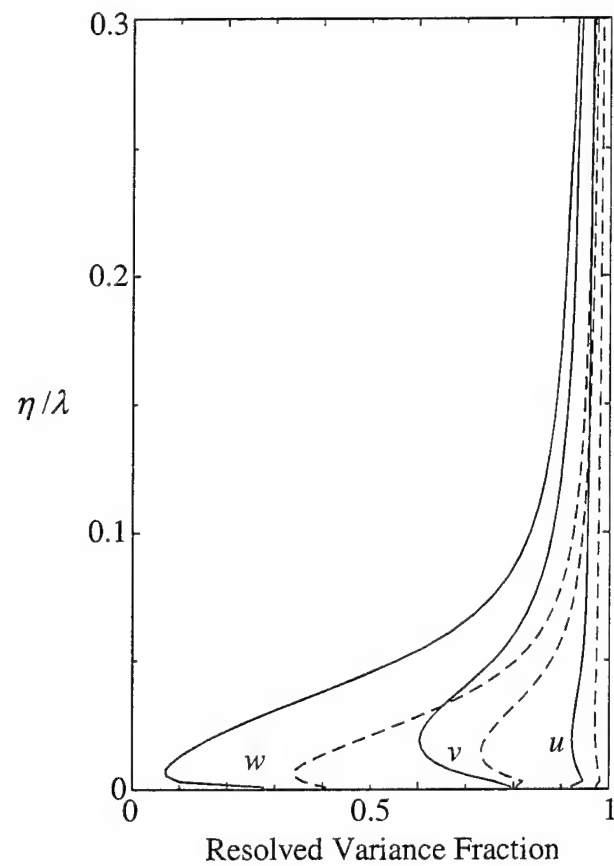


Figure 11. Fractions of velocity variances resolved by the LES. The standard resolution case S1 is shown with solid lines, the higher-resolution case S1R with dashed lines. The lines labeled "u" are fractions for the streamwise component (defined in the text); "v" and "w" denote the transverse and vertical components, respectively.

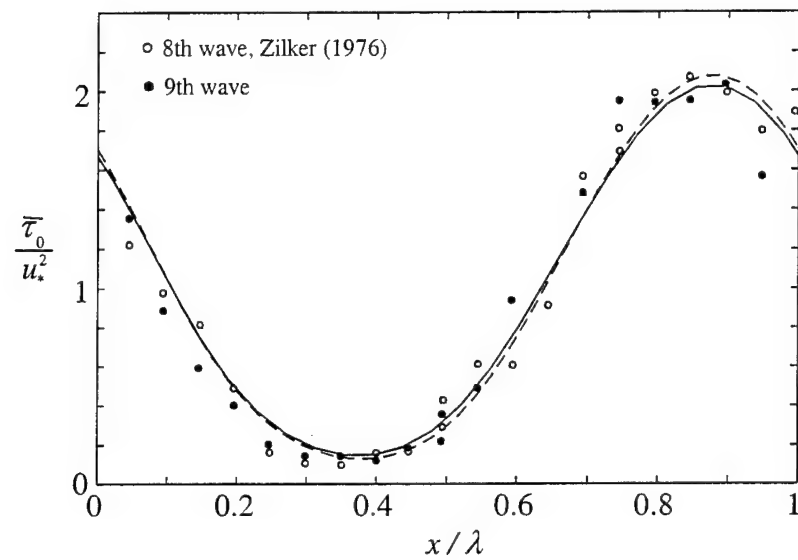


Figure 12. Non-dimensional shear stress distributions. Solid line is case S1; dashed line is S1R; symbols are the data of Zilker (1976) from two adjacent waves.

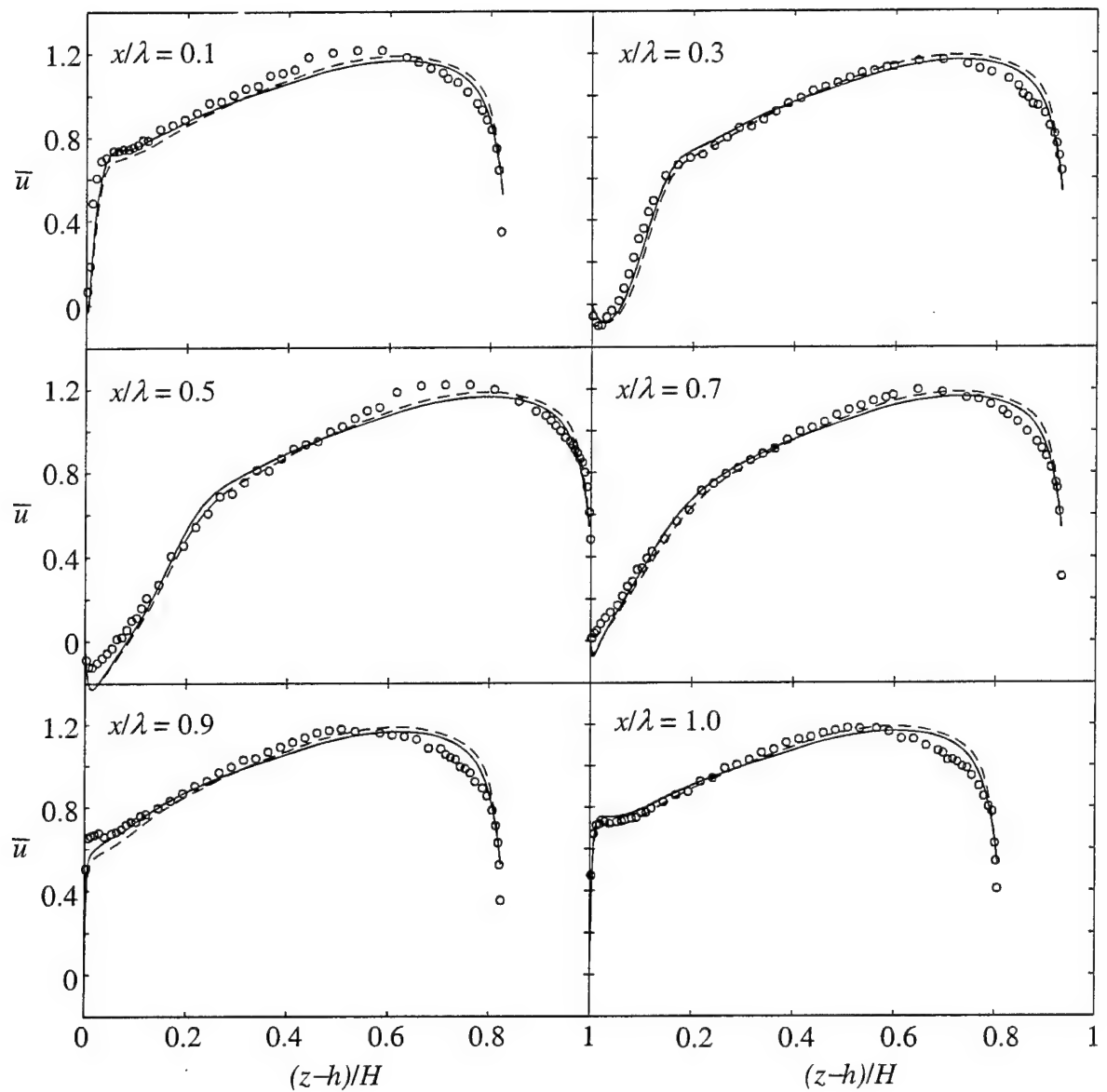


Figure 13. Profiles of mean streamwise velocity at various locations along the surface wave compared with the data of BHA. Solid lines are LES case BHA1; dashed lines are BHA1R; symbols are measurements.

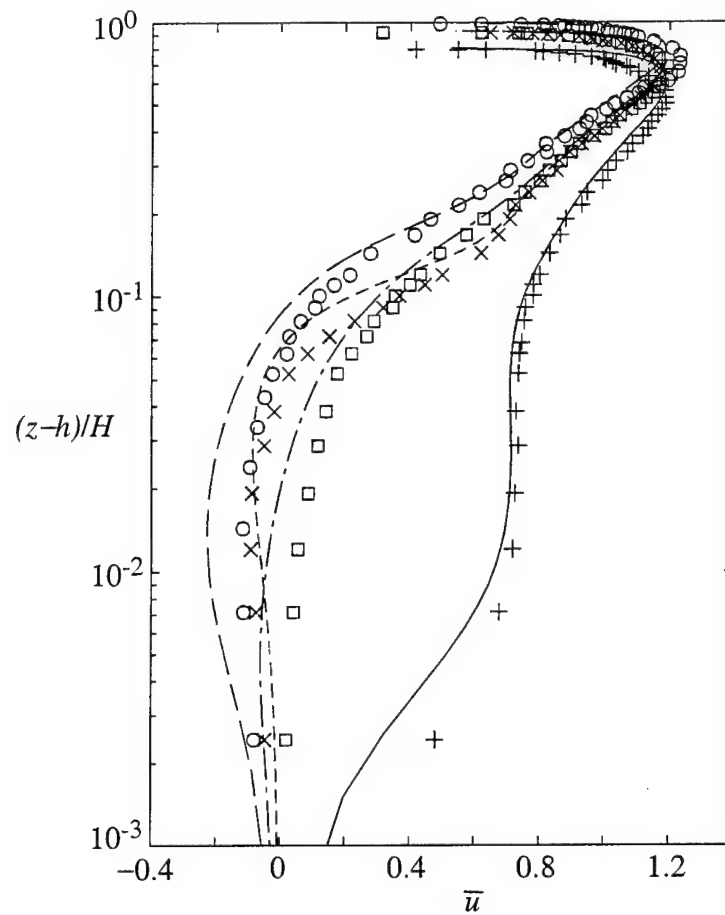


Figure 14. Profiles of mean streamwise velocity using a logarithmic vertical axis. Only profiles from BHA1R are shown for comparison with the data. (The profiles from BHA1 are very similar.) The lines denote LES profiles, symbols denote BHA measurements. $x/\lambda = 0.3$: short dashes; \times . $x/\lambda = 0.5$: long dashes; \circ . $x/\lambda = 0.7$: long-dash, short-dash; \square . $x/\lambda = 1$: solid line; $+$.

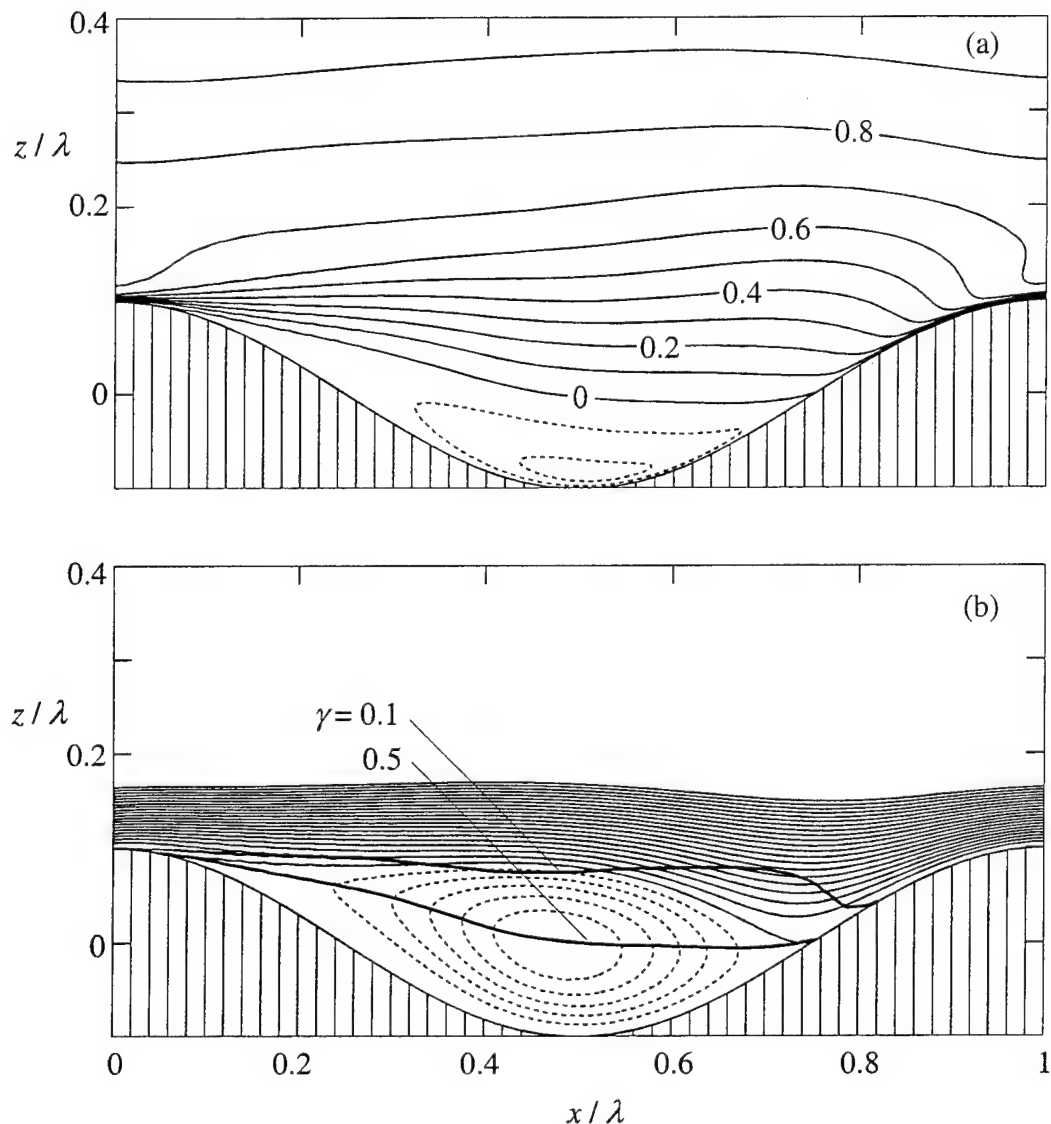


Figure 15. Mean flow field statistics from case BHA1R. (a) Streamwise velocity, (b) streamlines. Negative velocities and streamlines are shown as dashed lines. Also shown in (b) are the loci of 10% and 50% instantaneous reverse flow.

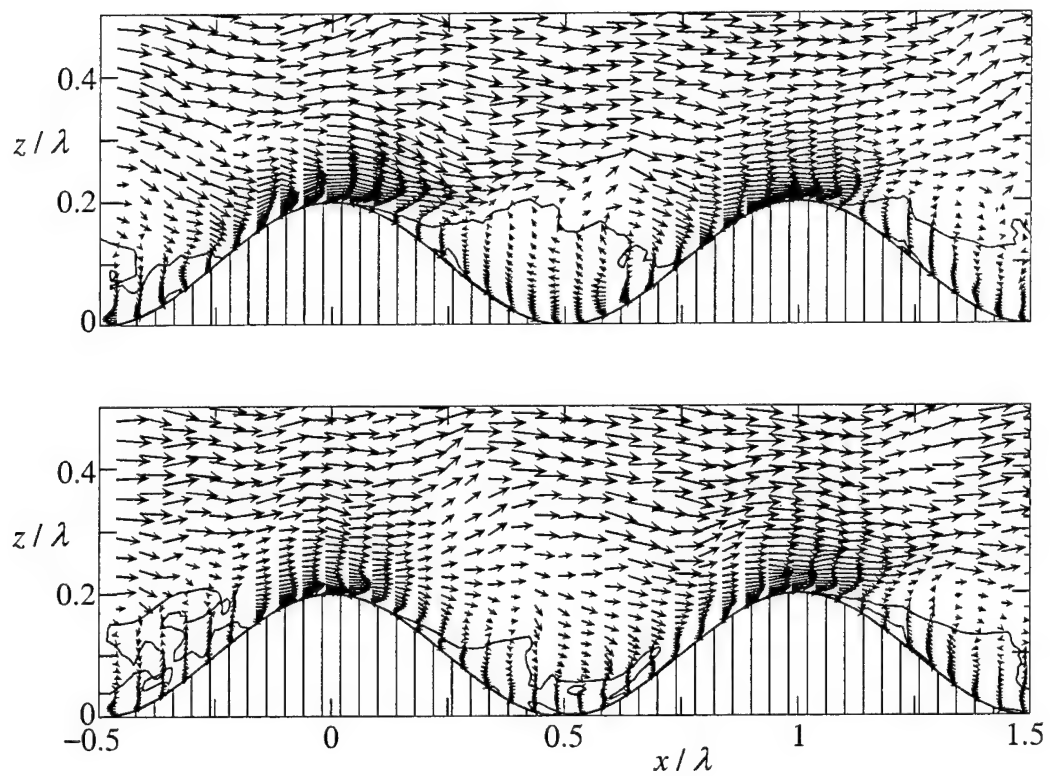


Figure 16. Two independent realizations of instantaneous velocity vectors (u, w) at $y = 0$ for case BHA1R. Solid lines denote loci of $u = 0$. Every other grid point is shown. The maximum velocity is approximately 1.4.

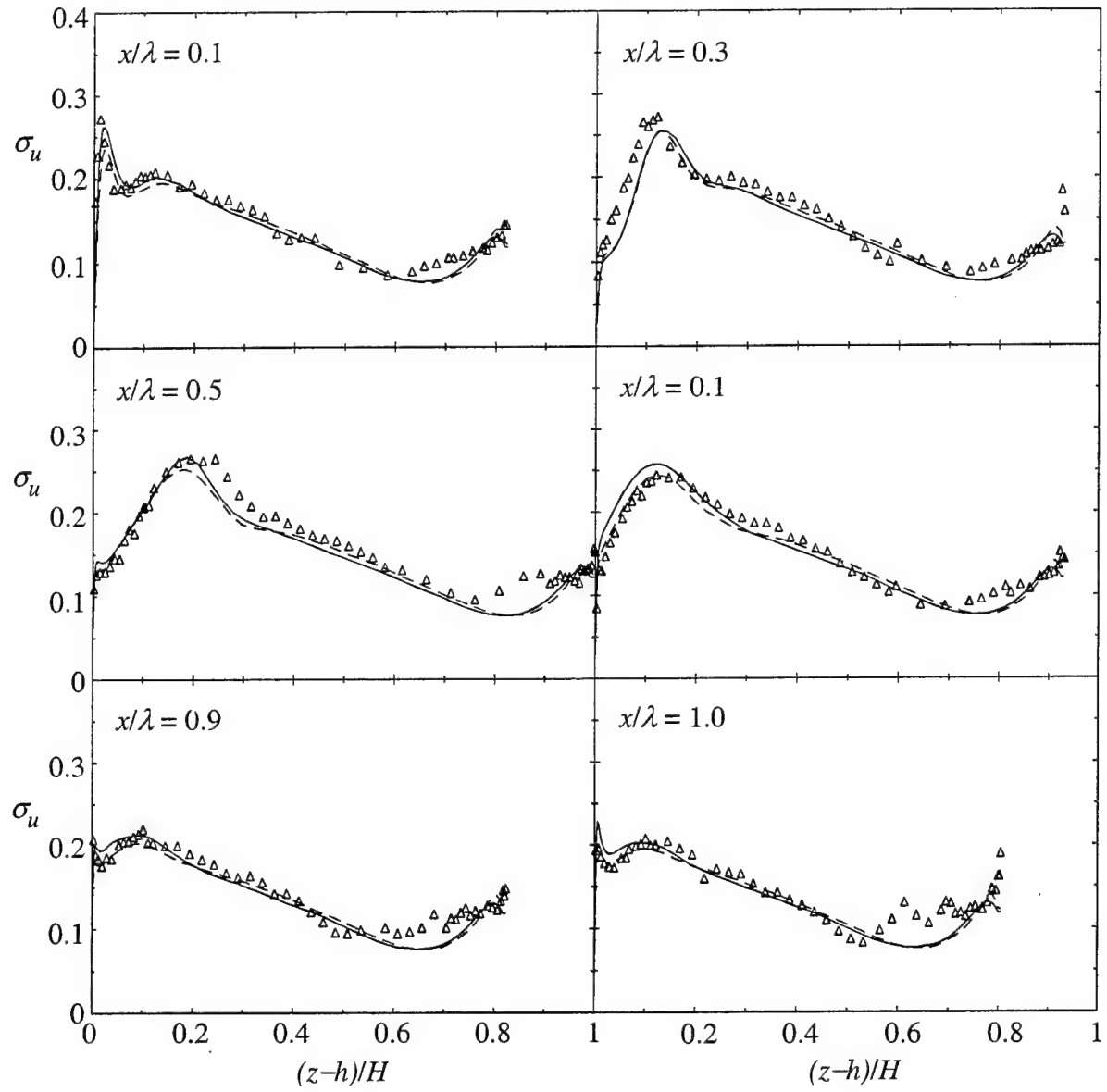


Figure 17. Profiles of mean streamwise turbulence intensity at various locations along the surface wave compared with the data of BHA. Solid lines are BHA1; dashed lines are BHA1R; symbols are measurements. Total LES turbulence intensities are shown.

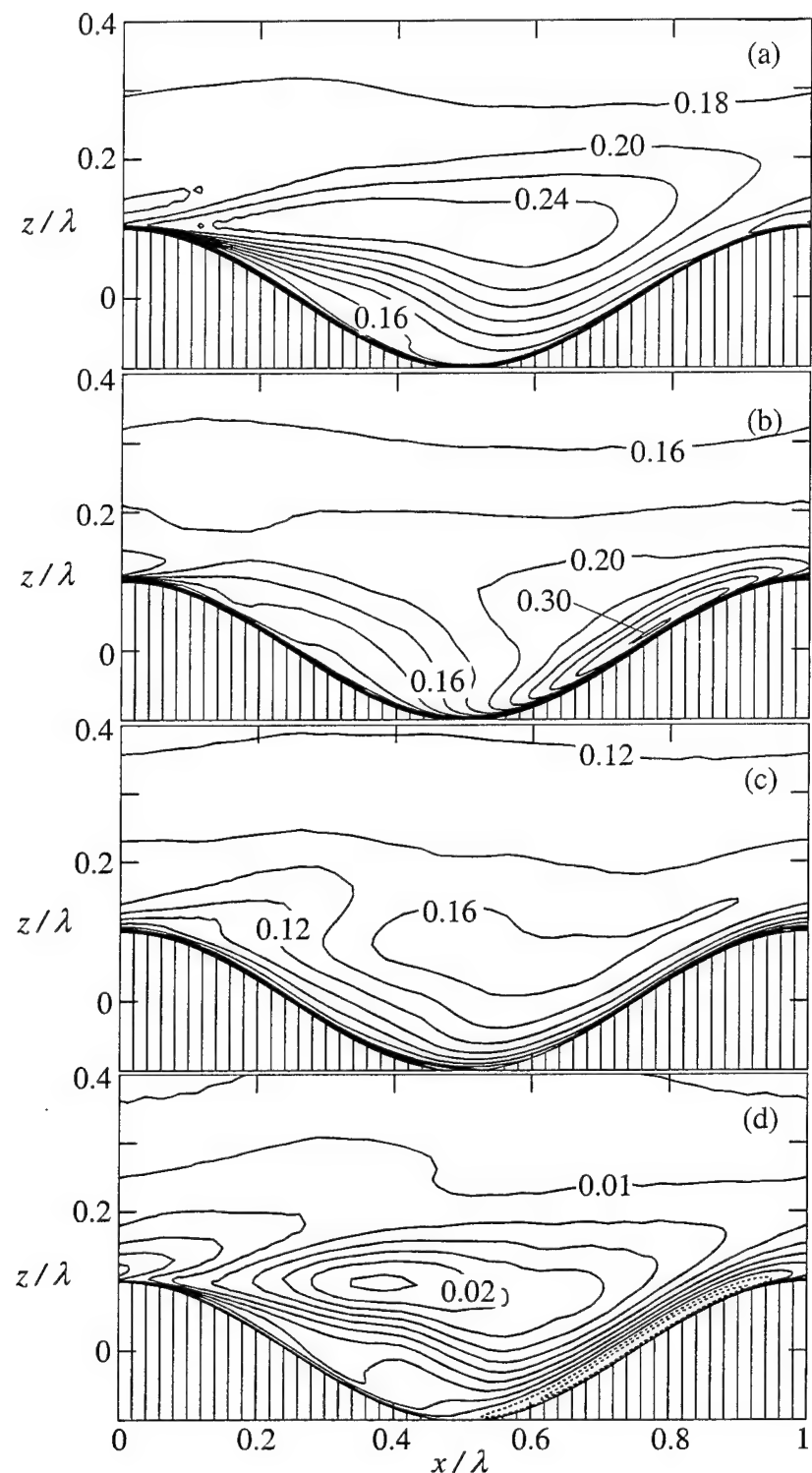


Figure 18. Dimensionless mean flow statistics from case BHA1R. (a) Streamwise turbulence intensity, σ_u , (b) transverse turbulence intensity, σ_v , (c) vertical turbulence intensity, σ_w , (d) Reynolds stress, $-\overline{u'w'}$.

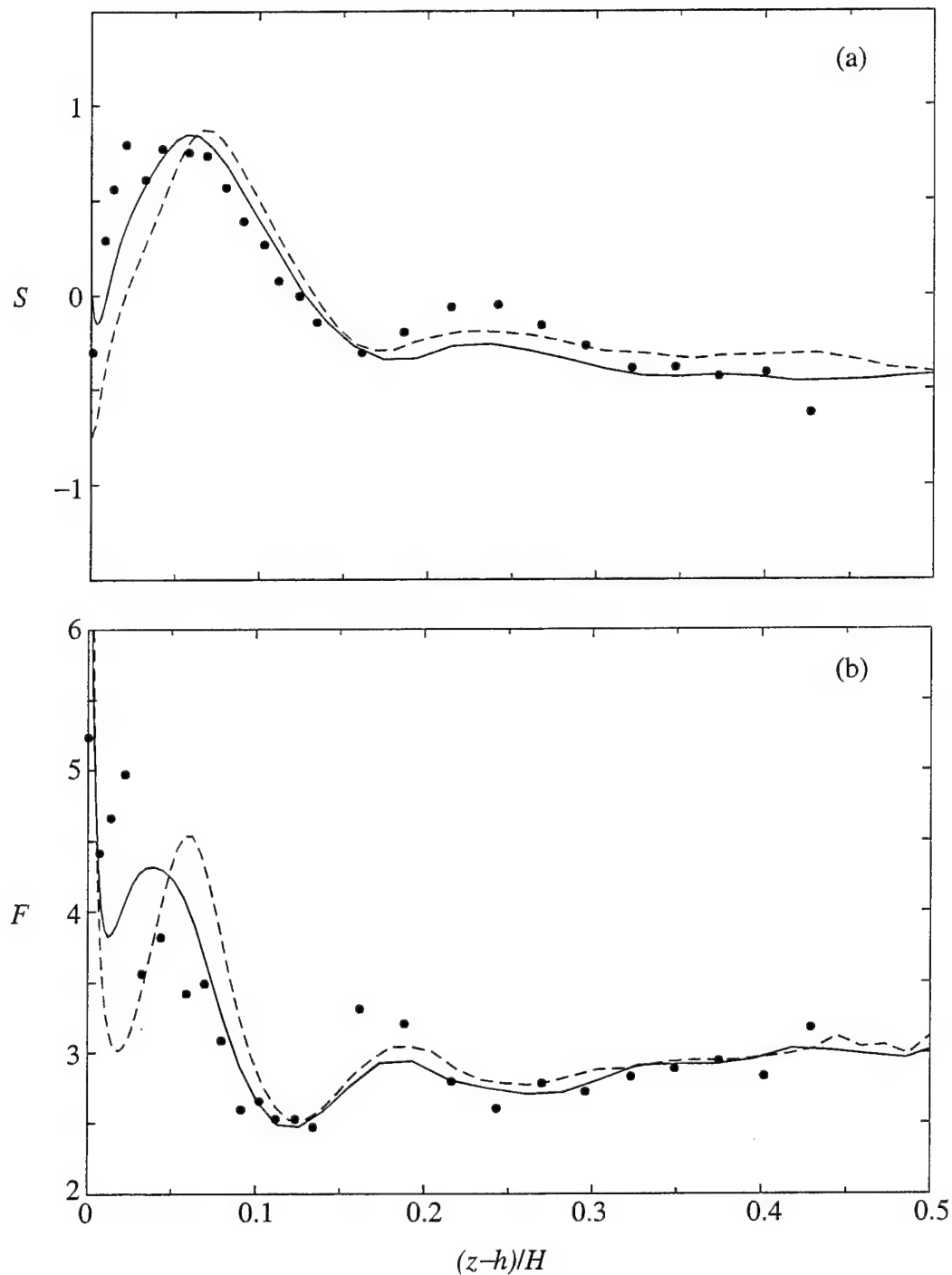


Figure 19. Higher-order statistics at $x/\lambda = 0.3$. Solid lines are BHA1; dashed lines are BHA1R; symbols are data of BHA. (a) Skewness. (b) Flatness.

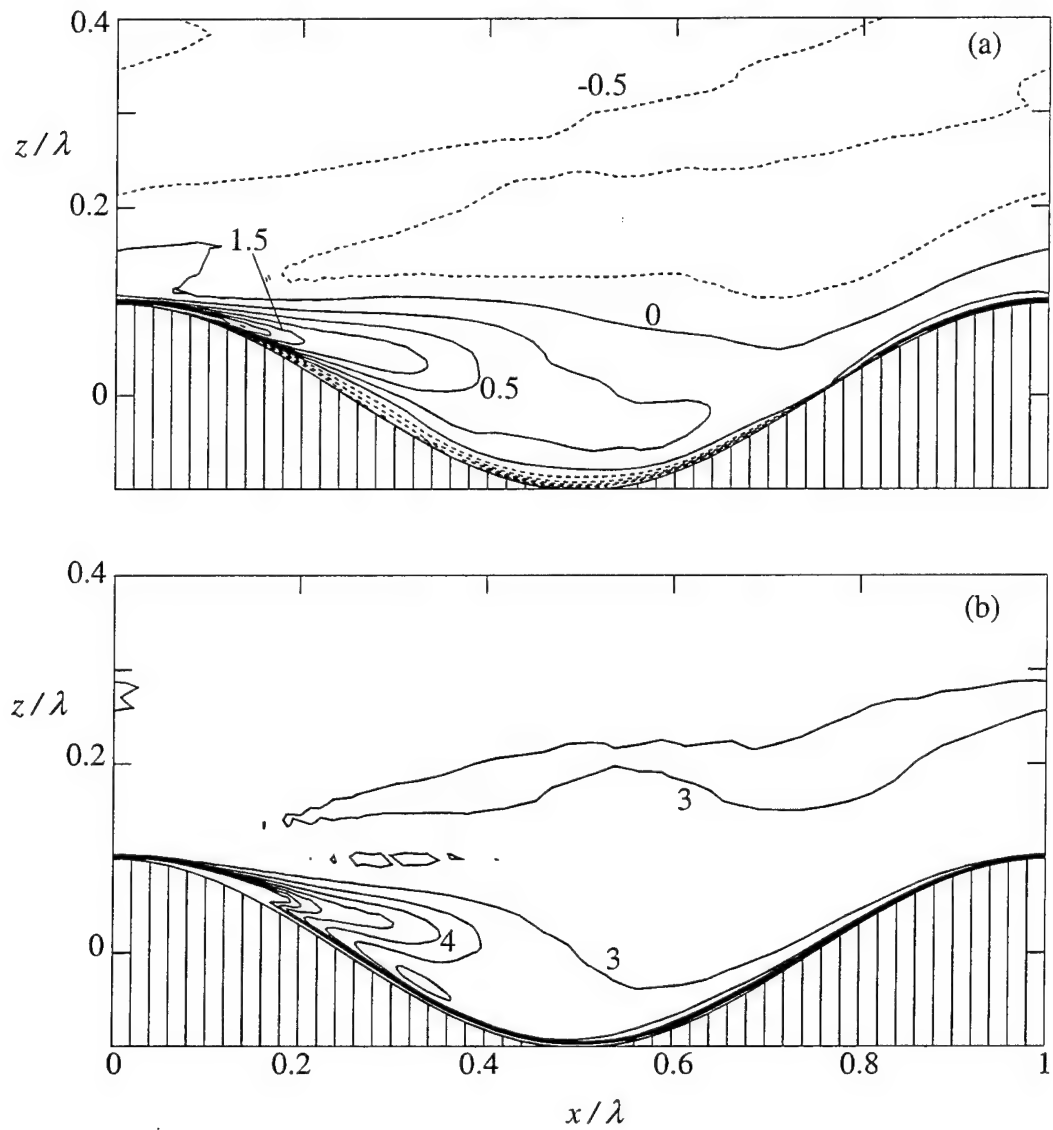


Figure 20. (a) Skewness; contour interval of 0.25. (b) Flatness; contour interval of 0.5.

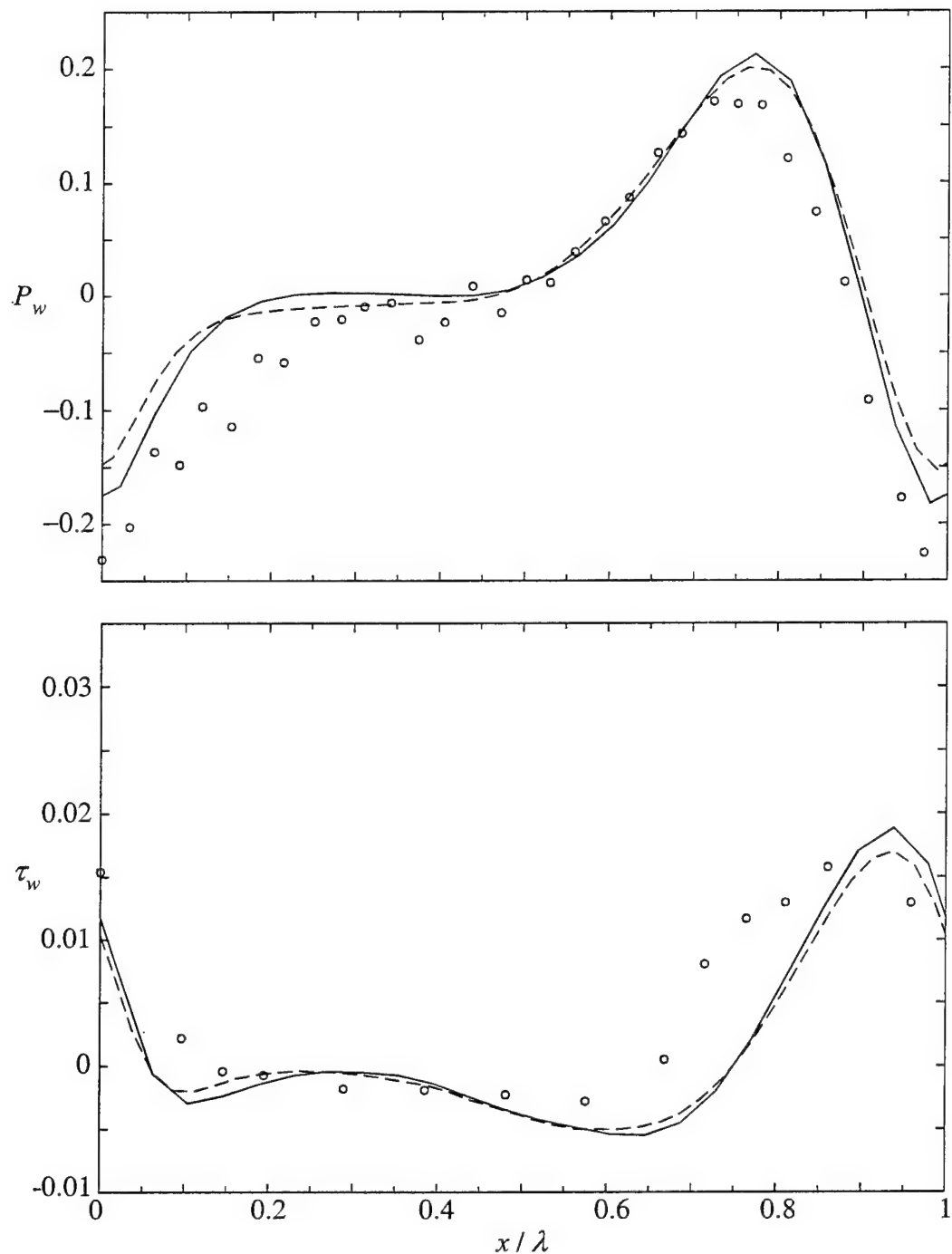


Figure 21. Non-dimensional wall pressure and surface shear stress distributions. Solid lines are BHA1; dashed lines are BHA1R; symbols are data of BHA.

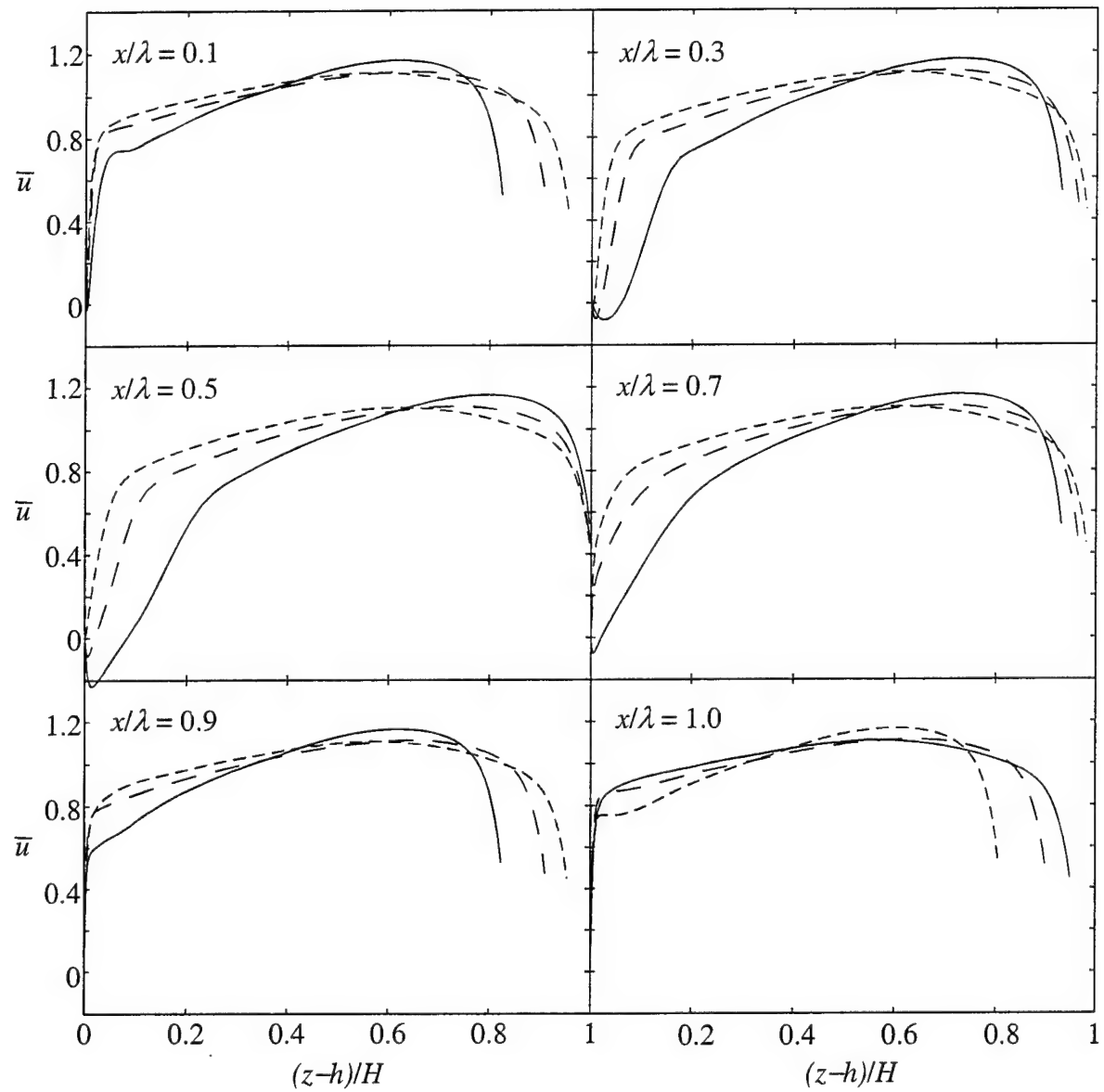


Figure 22. Profiles of mean streamwise velocity for 3 slopes: case BHA1 ($2a/\lambda = 0.2$), solid lines; case S3 ($2a/\lambda = 0.1$), long dashes; case S2 ($2a/\lambda = 0.05$), short dashes.

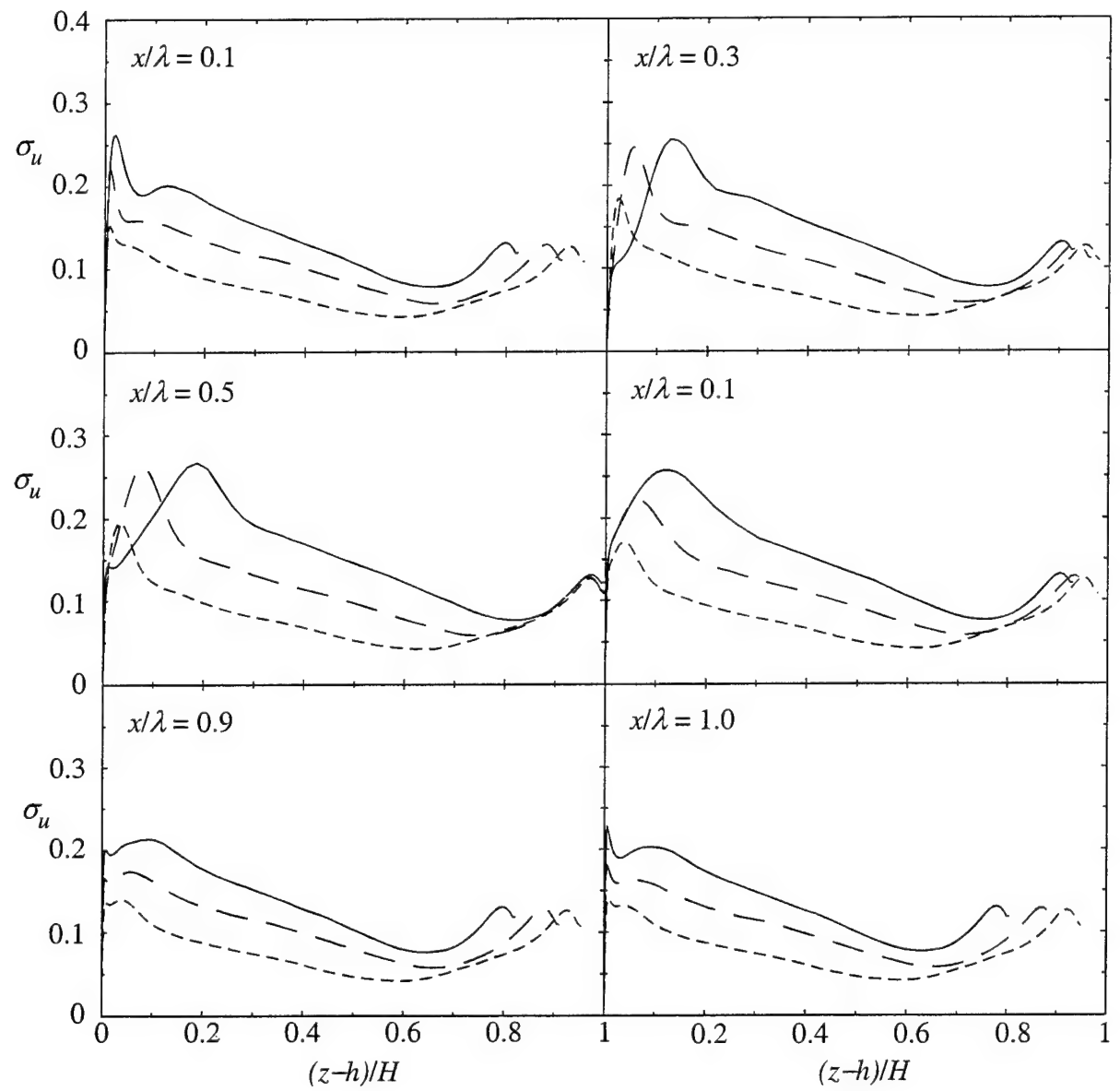


Figure 23. Profiles of mean streamwise turbulence intensity for cases BHA1, S3 and S2. Lines patterns as in Figure 22.

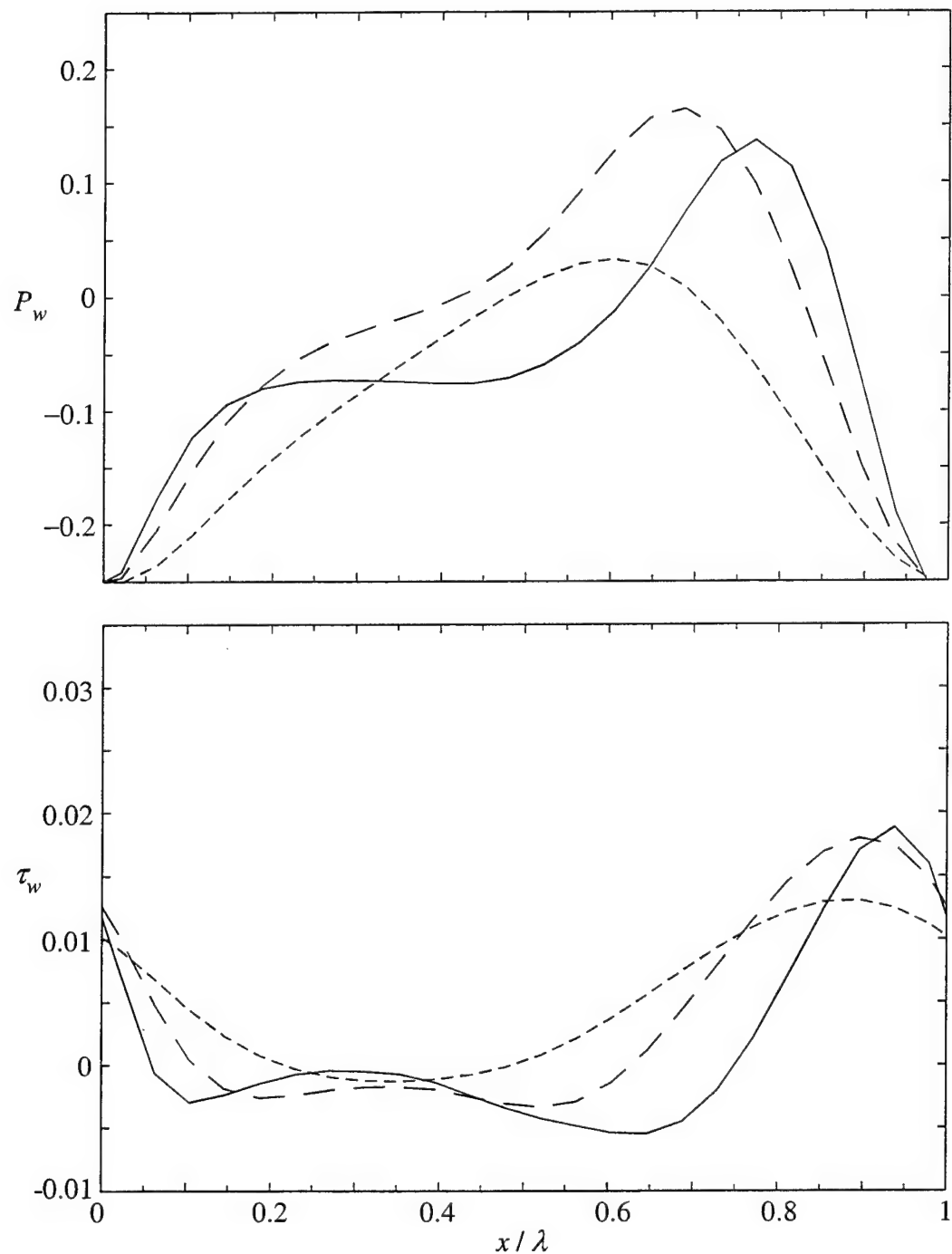


Figure 24. Non-dimensional wall pressure and surface shear stress distributions for cases BHA1, S3 and S2. Line patterns as in Figure 22.

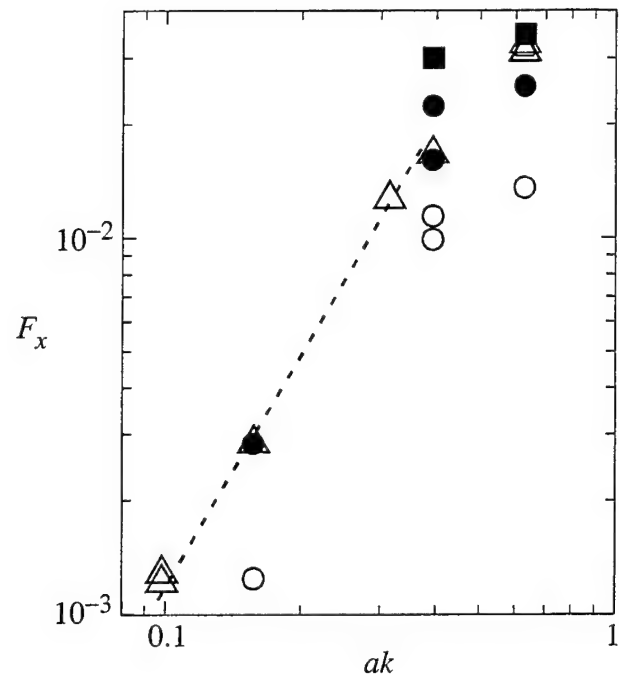


Figure 25. Form drag vs. wave slope as given in Table 3. \circ : data of Zilker and Hanratty (1979); \bullet : integration of Zilker and Hanratty pressure data; \square : data of BHA; \blacksquare : integration of BHA pressure data; \triangle : integration of LES surface pressure. Dashed line is proportional to $(ak)^2$.

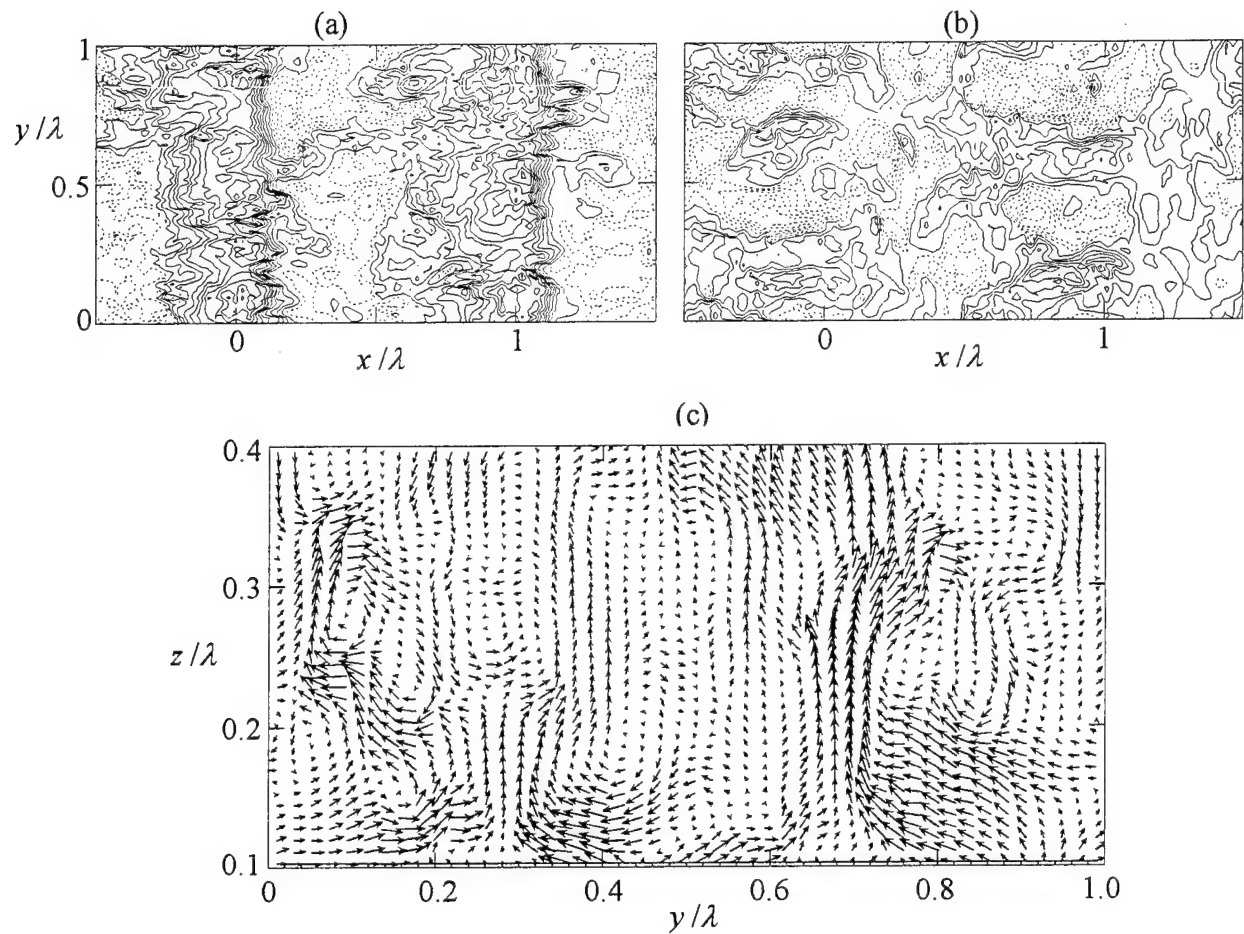


Figure 26. Instantaneous velocity fields from BHA1R. (a) u -component and (b) v -component at $\eta/\lambda = 0.025$. Contour interval is 0.1; dashed lines indicate negative values. (c) Secondary flow at $x/\lambda = 0.75$. The vectors are interpolated onto a 48×36 uniform grid. The maximum velocity is 0.7.

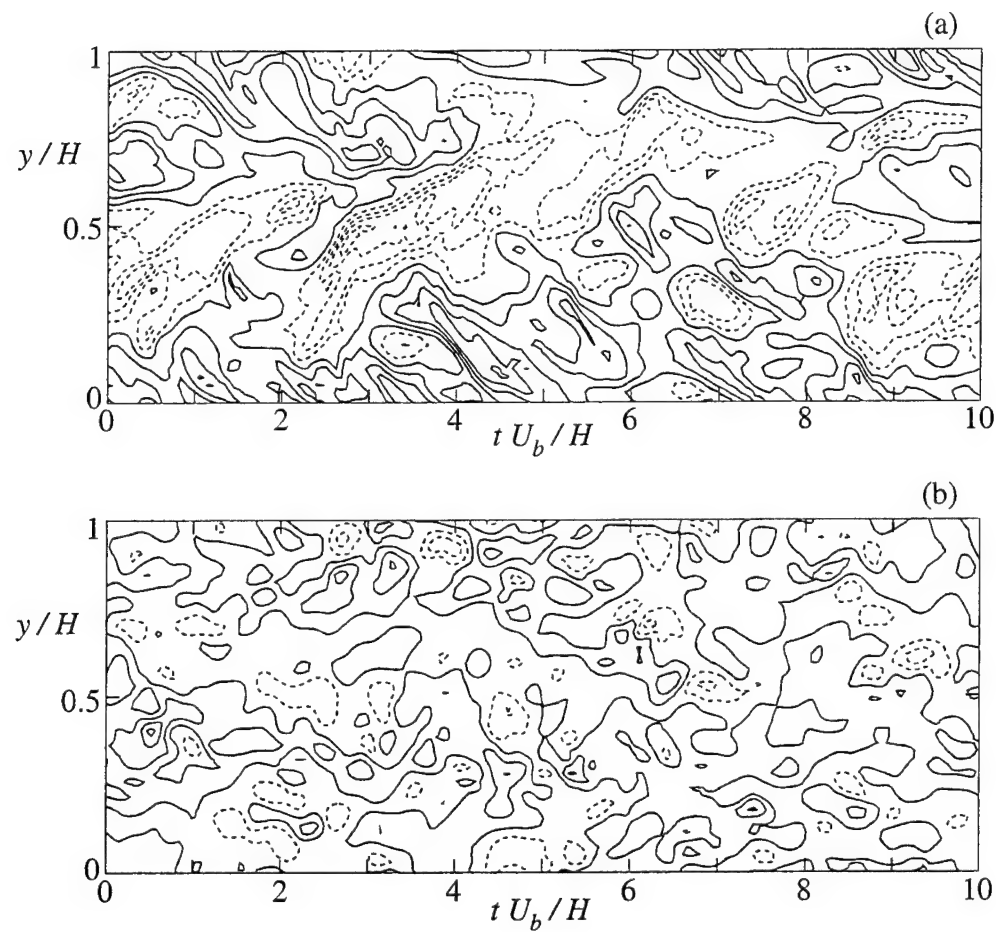


Figure 27. Transverse velocity at fixed streamwise and vertical position as a function of lateral position and time: (a) BHA1 at $x/\lambda = 0.75$ and $\eta/\lambda = 0.0125$, contour intervals are 0.1. (b) Case F at $z/H = 0.01$, contour intervals are 0.05.

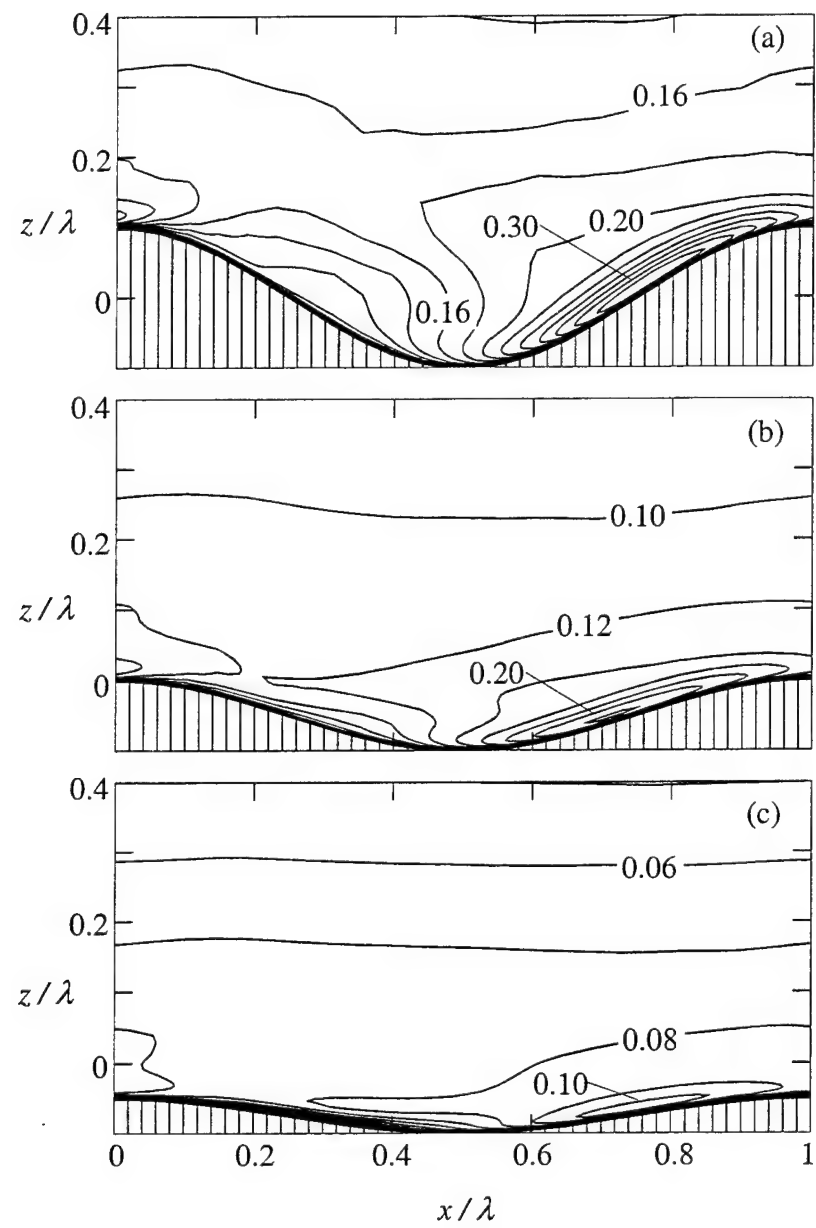


Figure 28. Transverse fluctuation intensity, σ_v , for three wave slopes. (a) BHA1, (b) S3, (c) S2.

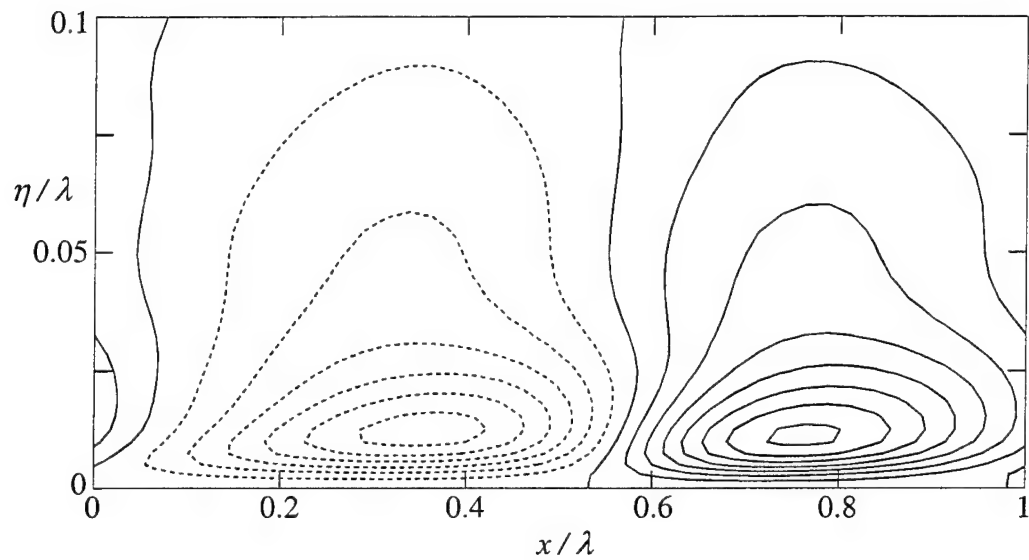


Figure 29. Transverse velocity variance perturbation from the wavelength average, normalized by u_*^2 , for case S1R. Contour interval is 0.1. Dashed lines indicate negative values.

APPENDIX B

Presented at the 9th Joint Conference on the Applications of Air Pollution Meteorology
American Meteorological Society
Atlanta, Georgia
28 January – 2 February 1996

7.3

LARGE-EDDY SIMULATION OF DISPERSION OVER TERRAIN

D. S. Henn* and R. I. Sykes

Titan/ARAP
Princeton, New Jersey

1. INTRODUCTION

Turbulent dispersion in the atmospheric boundary layer over a homogeneous surface is relatively well understood, especially under neutral and convectively unstable conditions. However, dispersion over terrain has not yet been studied extensively. In this paper, large-eddy simulation (LES), in conjunction with a generalized Gaussian puff method, is used to investigate the dispersion of a passive cloud in a convectively-driven boundary layer with moderate wind speed over idealized terrain. Variations in terrain slope, source location and wind direction are considered.

LES is a modelling technique wherein the large-scale eddies are represented explicitly while small scale turbulence is parameterized by a subgrid model. The convective boundary layer (CBL) is particularly amenable to study by LES, e.g. Mason (1989). LES has been used by Krettenauer and Schumann (1992) and Walko, et al. (1992) to study terrain-induced modifications to the CBL, but with no mean horizontal motion. Dispersion in the CBL has been investigated using LES, e.g., Lamb (1978) and Henn and Sykes (1992), but only for flat terrain.

To clearly illustrate the influence of terrain and isolate the effects of slope and release location an dispersion, height variations are sinusoidal in one direction only, obviously an idealized representation of ridge/valley topography.

2. MODEL DESCRIPTION

The LES model used to generate the velocity fields is an extension of the Cartesian model of Sykes and Henn (1989) and is based on the spatially-filtered equations of motion for an incompressible Boussinesq fluid. Second-order accurate, finite difference equations with leap-frog time differencing are used to solve for the velocity components (u, v, w), corresponding to the coordinate axes (x, y, z), and the perturbation potential temperature. The subgrid model uses a turbulent kinetic energy transport equation and an algebraic filter scale. The Cartesian model equations are

*Corresponding author address: D. S. Henn, Titan Research and Technology, ARAP Group, 50 Washington Road, Princeton, NJ 08543-2229.

recast using the terrain-following coordinate transformation of Clark (1977). Thus, the model vertical coordinate is defined by

$$\zeta = (z - h)/J, \quad (1)$$

where

$$J = 1 - h/D. \quad (2)$$

Here, $h(x, y)$ is the local terrain elevation and D is the depth of the computational domain. Details on the transformed equations can be found in Clark (1977) and Krettenauer and Schumann (1992).

Periodic boundary conditions are imposed horizontally. The upper boundary at $z = D$ is a rigid, stress-free lid. Rayleigh damping is applied to the vertical velocity near the upper lid to provide an effective non-reflecting boundary for propagating gravity waves. A uniform heat flux is specified on the bottom surface, $z = h(x, y)$. Monin-Obukov similarity relations are employed (with suitable rotations accounting for the local terrain slope) to set temperature and velocity on the first grid point above the surface.

The passive scalar conservation equation is solved by means of a generalized Gaussian puff model as described in Sykes and Henn (1995). Each puff has an associated mass, centroid and complete second-moment tensor which gives the Gaussian spread about its centroid. The method accounts completely for shear distortions of the puffs and employs an efficient splitting/merging scheme to maintain puff size consistent with the LES resolution. The LES subgrid turbulent kinetic energy is used to estimate puff diffusion. A puff is advected by the LES velocity field interpolated at the puff centroid; the periodicity of the velocity fields is utilized when a puff is transported beyond the nominal LES domain.

3. SIMULATION CONDITIONS

The terrain used in this study is a sinusoidal ridge defined as

$$h(x, y) = h_0(1 - \cos 2\pi x/\lambda)/2 \quad (3)$$

where λ is the wavelength and h_0 is the maximum height. The maximum slope is given by $S = \pi h_0/\lambda$. Results are presented for heights of 0, 159m and 318m, which, with a wavelength of 2km, correspond to $S = 0, 0.25$ and 0.5 , respectively. A surface rough

ness height of 1m and surface temperature flux of 0.03Kms^{-1} are specified for all simulations. The mean boundary layer depth is about 1000m, giving a convective velocity scale, w_* , of 1ms^{-1} .

The flow is initialized with a geostrophic wind (U_g, V_g) and a uniform vertical temperature gradient of 0.005Km^{-1} above $\zeta = 800 \text{m}$; a constant temperature and horizontal wind are prescribed below. Turbulence is initiated by a small random perturbation in the temperature field below $\zeta = 800 \text{m}$. The dispersion calculations commence only after an approximate balance is achieved between the Coriolis force and the surface momentum flux. This balance typically requires an integration time of about 40000s.

The LES calculations use a $48 \times 48 \times 65$ grid in a 4km cube domain. The horizontal grid spacing is uniform. The vertical grid spacing is non-uniform with 10m resolution at the surface, expanding to 40m in the middle of the boundary layer.

The dispersion calculations are initialized from a spherical puff 10m above the surface with a Gaussian spread of 10m. Independent dispersion realizations are obtained by varying the horizontal location of the source within the same LES fields as well as by releasing puffs 1800s apart. To examine the effects of terrain slope, source location and wind direction, seven cases are considered in this study and are summarized in Table 1. The dispersion statistics presented in Section 5 result from 24 realizations of 1800s duration for each case.

Table 1. Case Summary

Case	S	Source Location	U_g (ms^{-1})	V_g (ms^{-1})
F	0	arbitrary	5	0
H1	0.25	hill	5	0
V1	0.25	valley	5	0
H2	0.5	hill	5	0
V2	0.5	valley	5	0
H2D	0.5	hill	0	5
V2D	0.5	valley	0	5

4. VELOCITY FIELDS

Since the primary focus in this paper is the dispersion calculations, only a brief review of the velocity field results is presented.

Figure 1 shows the mean flow over ridges with $S = 0.5$ and $(U_g, V_g) = (5, 0)$. The streamlines show a clear reversed flow in the valleys and acceleration over the ridge crests, as expected. The transverse velocity component, v , (not shown) is relatively well-mixed with little response to the local terrain.

An example of the instantaneous flow structure is given in Figure 2. The near-surface streaklines, obtained by calculating trajectories in the instantaneous (u, v) -field 10m above the surface, show the distinct

separation region between the two ridges. The predominant flow near the surface is in the positive y -direction, except over the hill crests where the u -component is accelerated. The separation and reattachment lines, although meandered by the large eddies, are readily visible from the streaklines. The flow is clearly oriented along the valley axis in the separation and reattachment regions since the v -component is relatively constant.

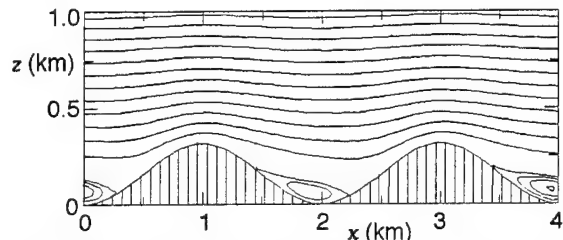


Figure 1. Mean streamlines, over 2km ridges with $S = 0.5$. Contour interval is $200 \text{m}^2 \text{s}^{-1}$ for positive values, $10 \text{m}^2 \text{s}^{-1}$ for negative values (shown dashed).

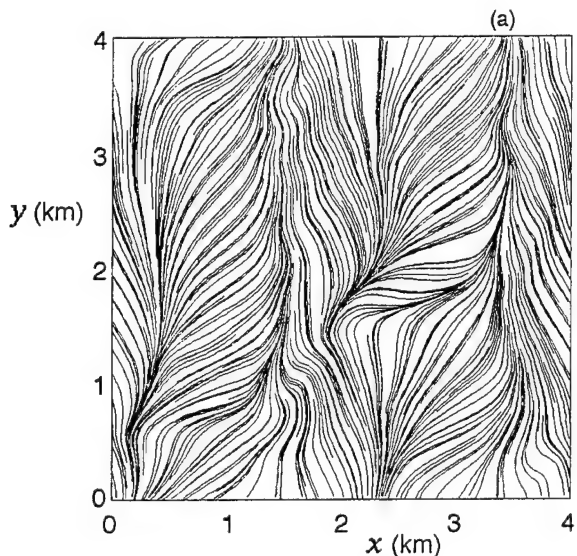


Figure 2. Instantaneous streaklines at $\zeta = 10 \text{m}$ over 2km ridges with $S = 0.5$.

Vertical profiles of the three velocity variance components are shown in Figure 3 along with the flat surface results. The general increase with terrain in all three components is immediately obvious. The horizontal variances are roughly doubled in the main boundary layer, with significant perturbations near the surface.

Although only results for $S = 0.5$ are shown here, those for the $S = 0.25$ case are qualitatively similar in the sense of an overall (but smaller) increase in horizontal variance. A notable difference is the absence of mean flow separation with $S = 0.25$. (But at any given time there generally are isolated occurrences of reverse flow.)

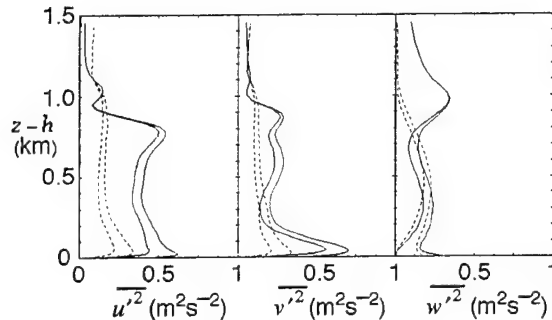


Figure 3. Vertical profiles of velocity variances for $S = 0.5$ at the hill crest. The dashed lines are for the corresponding flat case. Both resolved and total variances are shown.

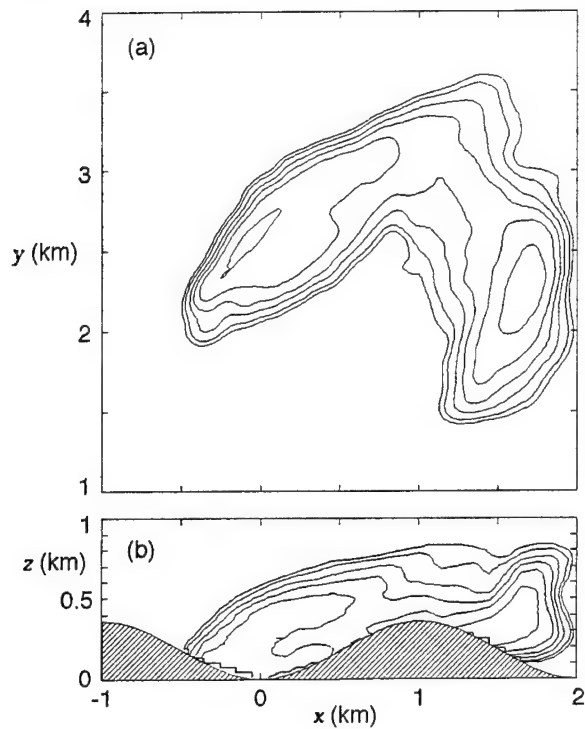


Figure 4. Instantaneous cloud from a realization of case V2 at 840s. (a) Vertically-integrated concentration. (b) Horizontally-integrated concentration. Normalized contours of .01, .02, 0.05, 0.1, 0.2, 0.5.

5. DISPERSION STATISTICS

A number of independent realizations of the contaminant field have been generated with the goal of obtaining reliable ensemble dispersion statistics. An example of the instantaneous field from a realization of case V2 is shown in Figure 4 and clearly illustrates how terrain can enhance dispersion by the separation of material between adjacent valleys.

To quantify the effects of terrain on dispersion estimates of the ensemble cloud centroid and spread

for the cases given in Table 1 will now be presented. The cloud centroid for each realization is defined as

$$\bar{x}_i = \sum_n Q_n \bar{x}_{i_n} / \sum_n Q_n \quad (4)$$

where the summation is over all puffs, Q_n is the mass of puff n and \bar{x}_{i_n} is the puff centroid relative to the release location. The ensemble centroid is then $\langle \bar{x}_i \rangle$ where the brackets indicate averaging over all realizations. The total ensemble spread, $T_{\alpha\alpha}$, is the combination of a meander component, $M_{\alpha\alpha}$ and a relative dispersion component, $S_{\alpha\alpha}$:

$$T_{\alpha\alpha} = M_{\alpha\alpha} + S_{\alpha\alpha} \quad (5)$$

($\alpha = 1, 2$ or 3 with no summation, corresponding to coordinates x , y , or z) where

$$M_{\alpha\alpha} = \left\langle \left(\bar{x}_\alpha - \langle \bar{x}_\alpha \rangle \right)^2 \right\rangle \quad (6)$$

and

$$S_{\alpha\alpha} = \left\langle \sum_n \left[Q_n \sigma_{\alpha\alpha n} + \left(\bar{x}_{\alpha n} - \bar{x}_\alpha \right)^2 \right] \right\rangle / \sum_n Q_n \quad (7)$$

Here, $\sigma_{\alpha\alpha n}$ are the diagonal components of the second-moment tensor for each puff.

The mean horizontal trajectories of the ensemble clouds, relative to the release locations, are shown in Figure 5. For the $U_g = 5 \text{ ms}^{-1}$ cases, the paths become increasingly oriented parallel to the ridges with increasing slope, a result of the Coriolis force balancing the increased surface stress normal to the ridges. The valley release with $S = 0.5$, case V2, is particularly interesting since its path initially shows a slight reverse flow in the x -direction and, as a result, is confined to the valley and travels along its axis for roughly the first 500s, after which it parallels the hill release. On the other hand, for $S = 0.25$, the paths for the hill and valley releases diverge only slightly at the outset and then quickly converge.

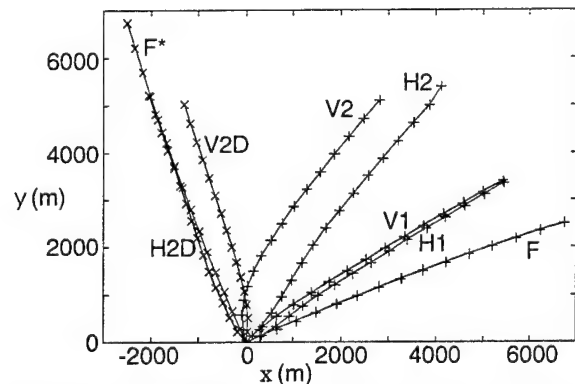


Figure 5. Ensemble cloud centroid trajectories for the cases of Table 1. Symbols represent 120s time increments. The flat case F^* is shown for comparison with the $U_g = 5 \text{ ms}^{-1}$ cases and is merely case F rotated 90° .

The ensemble cloud spread in the direction normal to the ridges as a function of time is shown in

Figure 6 for the first 5 cases from Table 1, i.e., $U_g = 5\text{ms}^{-1}$. It can be seen that T_{xx} is considerably enhanced for $S = 0.5$ over the flat terrain case for both hill and valley releases. And while the hill release with $S = 0.25$ also shows enhanced dispersion, the valley release surprisingly results in reduced dispersion.

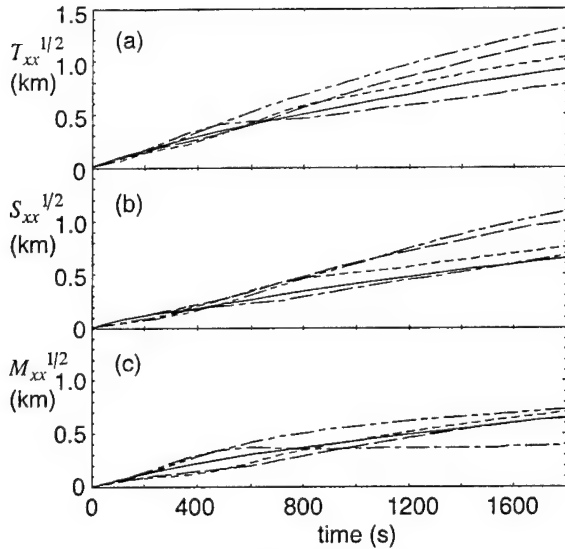


Figure 6. Ensemble dispersion normal to the ridges for the $U_g = 5\text{ms}^{-1}$ cases. Solid line: case F; short dashes: H1; long dash, short dash: V1; long dashes: H2; long dash, two short dashes: V2. (a) Total, (b) relative dispersion, (c) meander component.

Sensitivity to release location for the terrain cases is not surprising. V2 shows greater dispersion normal to the ridges than H2 and this is most likely related to the flow separation in the valleys generating a significantly larger meander component for V2 than for H2. Figure 5b clearly shows M_{xx} for V2 and H2 diverging over the first 600s, after which they slowly converge. Thus, sensitivity to release location is mainly due to the different time and spatial scales of the large eddies at the hill crest and in the valley.

The dispersion for case V1 appears to be anomalous and is clearly due to the behavior of M_{xx} since S_{xx} is quite close to cases F and H1. After closely matching the V2 results for the first 400s, the V1 meander component decreases slightly and then remains nearly constant for the remainder of the integration, showing no apparent convergence with the corresponding hill release. V1 is the only case which shows any decrease or constancy of M_{xx} ; all others show monotonic increases. The lack of convergence with H1 is especially surprising given that the mass-weighted (resolved) velocity variance, T_{uu} , does converge for the two cases, as shown in Figure 7. Here

$$T_{uu} = M_{uu} + S_{uu} \quad (8)$$

where

$$M_{uu} = \left\langle \left(\bar{u} - \langle \bar{u} \rangle \right)^2 \right\rangle \quad (9)$$

$$S_{uu} = \left\langle \sum_n \left[\left(\bar{u}_n - \bar{u} \right)^2 \right] \right\rangle / \sum_n Q_n \quad (10)$$

u_n is the u -component at the centroid of puff n and \bar{u} is the mass-weighted mean for a realization. It can be seen that T_{uu} for V1 is initially similar to V2, then decreases at a time corresponding to the decrease in T_{xx} and finally converges with case H1 at around 800s. The fact that T_{xx} does not converge for V1 and H1 despite this implies some kind of negative velocity correlation for the valley release. Since

$$\frac{dM_{xx}}{dt} = 2\langle \bar{x}' \bar{u}' \rangle \quad (11)$$

where the prime denotes fluctuation from the ensemble mean, M_{xx} can decrease or remain constant only if $\langle \bar{x}' \bar{u}' \rangle \leq 0$ and indeed this condition occurs for V1 but not the other cases. It is unknown if this is a general result or an artifact of the sinusoidal character of the terrain and clearly needs further investigation.

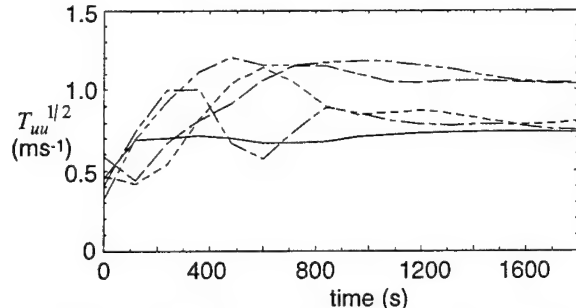


Figure 7. Total ensemble u -component velocity fluctuation intensities for the $U_g = 5\text{ms}^{-1}$ cases. Line patterns as in Figure 6.

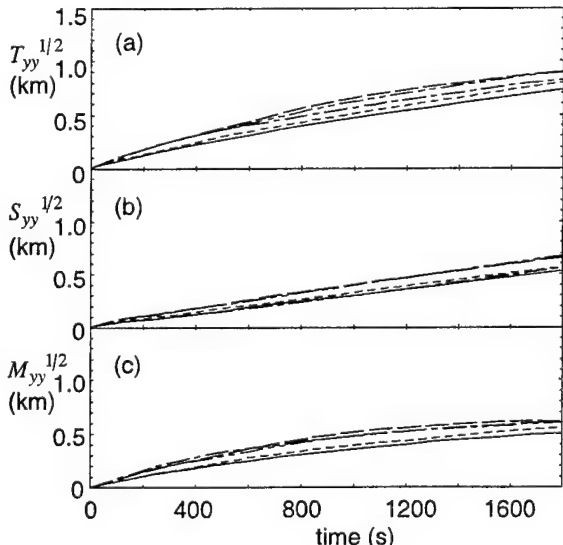


Figure 8. Ensemble dispersion parallel to the ridges for the $U_g = 5\text{ms}^{-1}$ cases. Line patterns as in Figure 6.

Dispersion parallel to the ridges is shown in Figure 8. All terrain cases show enhanced dispersion over the flat case but, with the exception of the

anomalous case V1, the absolute values are less than in the normal direction. The enhanced dispersion is mostly due to larger meander components; relative dispersion in the presence of terrain is not significantly greater than the flat case. Also, as expected, sensitivity to release location is not as pronounced as in the x -direction since v does not vary significantly with the local terrain.

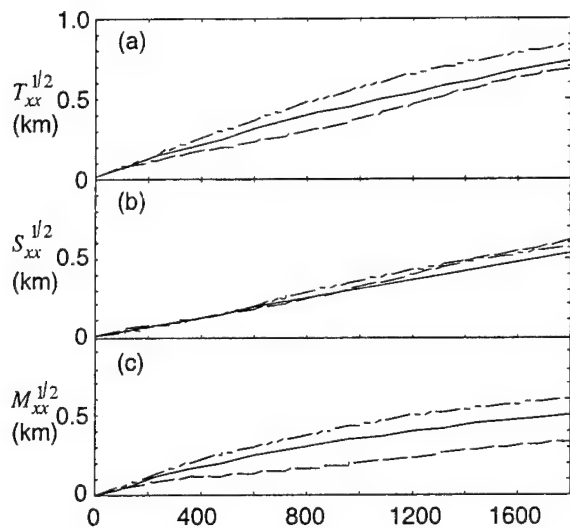


Figure 9. Ensemble dispersion normal to the ridges for the $V_g = 5 \text{ ms}^{-1}$ cases. Solid line: case F (rotated); long dashes: H2D; long dash, two short dashes: V2D. (a) Total, (b) relative dispersion, (c) meander component.

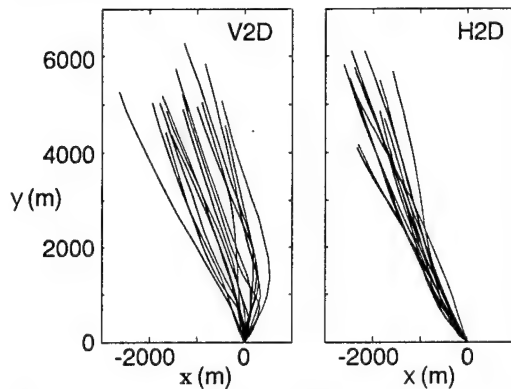


Figure 10. Trajectories of cloud centroids from individual realizations of cases V2D and H2D.

Finally, to show that the orientation between the wind and predominant terrain direction can be important, statistics for cases V2D and H2D are now presented. Figure 5 shows the horizontal ensemble trajectories of these cases in addition to the flat case F, rotated 90° for comparison. Obviously, the valley release results in slower transport across the ridges, implying that material may initially be trapped within a

valley. However, as shown in Figure 9, the dispersion across the ridges is greater for V2D than H2D due to an increased meander component for the valley release. Apparently, the cloud in some realizations of V2D remains in the valley in which it was released for a relatively long time, while in others, the cloud quickly moves over the ridge. Examples of this behavior are given in Figure 10 which shows the centroid trajectories of all realizations of cases V2D and H2D.

6. CONCLUSION

LES has been used to investigate the flow and dispersion over idealized ridge/valley terrain. It has been found that dispersion is generally enhanced by terrain, especially for large slopes, and that it can be sensitive to release location. It is also found that dispersion is a function of wind direction with respect to the ridge/valley orientation, greater dispersion resulting from flow predominantly normal to the ridge. An anomalous decrease in dispersion (relative to flat terrain) for a valley release and moderate slope certainly requires further investigation.

Future work will be aimed at quantifying the dispersion results in terms of terrain slope, wind speed and orientation and extending this to more complex terrain.

Acknowledgment. This work was supported by the U. S. Army Research Office and the U.S. Defense Nuclear Agency.

REFERENCES

- Clark, T. L. (1977), "A small-scale dynamic model using a terrain-following coordinate transformation", *J. Comp. Phys.*, **24**, 186-215.
- Henn, D. S. and R. I. Sykes (1992), "Large-eddy simulation of dispersion in the convective boundary layer", *Atmos. Env.*, **26A**, 3145-3159.
- Krettenauer, K. and U. Schumann (1992), "Numerical solution of turbulent convection over wavy terrain", *J. Fluid Mech.*, **237**, 261-300.
- Lamb, R. G. (1978), "A numerical simulation of dispersion from an elevated point source in the convective planetary boundary layer", *Atmos. Env.*, **12**, 1297-1304.
- Mason, P. J. (1989), "Large-eddy simulation of the convective atmospheric boundary layer", *J. Atmos. Sci.*, **46**, 1492-1516.
- Sykes, R. I. and D. S. Henn (1995), "Representation of velocity gradient effects in a Gaussian puff model", *J. Appl. Met.*, to appear.
- Sykes, R. I. and D. S. Henn (1989), "Large-eddy simulation of turbulent sheared convection", *J. Atmos. Sci.*, **46**, 1106-1118.

APPENDIX C

Presented at the 10th Joint Conference on the Applications of Air Pollution Meteorology
American Meteorological Society
Phoenix, Arizona
11–16 January 1998

5B.2

DISPERSION EFFECTS OVER RIDGE/VALLEY TERRAIN

D. S. Henn* and R. I. Sykes

Titan/ARAP
Princeton, New Jersey

1. INTRODUCTION

Most of our current understanding of dispersion in the atmosphere is based on an assumption of horizontal surface homogeneity, which is valid in only limited situations. Since significant terrain features cover much of the earth's surface, dispersion in the presence of terrain is of considerable interest. Here, we use large-eddy simulation (LES) to investigate the dispersion of a passive cloud over idealized terrain. Variations in terrain slope and source location under strongly convective and near-neutral conditions are considered.

LES is a modeling technique wherein the large-scale eddies are represented explicitly while a subgrid model parameterizes small-scale turbulence. The convective boundary layer, characterized by eddies on the scale of the boundary layer, is particularly amenable to study by LES, e.g. Mason (1989). Likewise, the presence of large-scale terrain features, while certainly presenting modeling difficulties, is expected to generate flow features well-represented by LES (Gong, et al., 1996). Terrain-induced modifications to the convective boundary layer have been studied using LES by Krettenauer and Schumann (1992), and Dörnbrack and Schumann (1993).

To clearly illustrate the influence of terrain and isolate the effects of slope and release location on dispersion, height variations are sinusoidal in one direction only. Although obviously an idealization, this is a reasonable prototype of ridge-valley terrain.

2. MODEL DESCRIPTION

The LES model used to generate the velocity fields is an extension of the Cartesian model of Sykes and Henn (1989) and is based on the spatially filtered equations of motion for an incompressible Boussinesq fluid. Second-order accurate, finite difference equations with leap-frog time differencing are used to solve for the resolved-scale velocity components (u, v, w), corresponding to the coordinate axes (x, y, z), and the perturbation potential temperature. The sub-

grid model uses a turbulent kinetic energy transport equation and an algebraic filter scale. The Cartesian model equations are recast using a terrain-following coordinate transformation; details can be found in Clark (1977) and Krettenauer and Schumann (1992). Preliminary results from this model have been reported in Henn and Sykes (1996, 1997).

Periodic boundary conditions are imposed horizontally. The upper boundary is a rigid, stress-free lid. Rayleigh damping is applied to the vertical velocity near the upper lid to provide an effectively non-reflecting boundary for propagating gravity waves. A uniform heat flux is specified on the bottom surface. Monin-Obukov similarity relations are employed (with suitable rotations accounting for the local terrain slope) to set temperature and velocity on the first grid point above the surface.

The scalar dispersion calculations employ the generalized Gaussian puff model of Sykes and Henn (1995) when early-time, near-source behavior is of primary interest or a particle method, which accounts for subgrid diffusivity with a random-walk model, when late-time statistics are desired. The second-order accurate Adams-Bashforth scheme is used in both methods to advance the puff/particle location, with the advection velocity determined by interpolation from the LES velocity field. The periodicity of the velocity fields is utilized when a puff or particle is transported beyond the nominal LES domain.

3. SIMULATION CONDITIONS

The terrain used in this study is a sinusoidal ridge defined as

$$h(x, y) = h_0(1 - \cos 2\pi x/\lambda)/2 \quad (3)$$

where λ is the wavelength and h_0 is the maximum height. The maximum slope is given by $S = \pi h_0/\lambda$. Results are presented for heights of 0, 159 m and 318 m, which, with $\lambda = 2$ km correspond to $S = 0, 0.25$ and 0.5, respectively. A surface roughness height of 1 m is assumed for all simulations.

The flow is driven by a geostrophic wind of 5 ms^{-1} perpendicular to the hill crests. To investigate the effects of thermal stability, two uniform surface temperature fluxes are considered: $0.03^\circ\text{Kms}^{-1}$ and $0.0045^\circ\text{Kms}^{-1}$. The resulting convective boundary layer is capped by an overlying stable layer with a

*Corresponding author address: D. S. Henn, Titan Corp., ARAP Group, 50 Washington Road, Princeton, NJ 08543-2229; e-mail: dhenn@titan.com

mean temperature gradient of $0.005^{\circ}\text{Km}^{-1}$. The boundary layer depth is maintained at approximately 1000 m, which means that the two heat fluxes considered correspond to convective velocity scales w_* of 1 ms^{-1} and 0.5 ms^{-1} , respectively. The higher heat flux results in flow which, at least over flat terrain, is dominated by large-scale convective eddies (the ratio of the shear-stress velocity to the convective velocity scale, $u_*/w_* = 0.4$) while the lower heat flux case is closer to neutral stability in character ($u_*/w_* \approx 0.7$).

The LES calculations use a $48 \times 48 \times 65$ grid in a 4 km cube domain. The horizontal grid spacing is uniform. The vertical grid spacing is non-uniform with 10 m resolution at the surface, expanding to 40 m in the middle of the boundary layer.

The short-range (puff) dispersion calculations are initialized from a spherical puff 10 m above the surface with a Gaussian spread of 10 m. The late-time (particle) calculations are initialized from a cloud of 1000 randomly distributed particles located 200 m above the wave crest with a spread of 100 m. Independent dispersion realizations within the same LES field are obtained by separating four releases 1000 m apart; this procedure is repeated for a number of independent LES fields. Thus, the dispersion statistics presented in Section 5 are computed from ensembles of 12 to 24 realizations.

To examine the effects of terrain slope, source location and stability, sixteen cases are considered and are summarized in Table 1. The case designations are as follows: "A" and "B" denote low heat flux or high heat flux cases, respectively; 0, 1 and 2 correspond to $S = 0, 0.25$ and 0.5 , respectively; "H" and "V" denote hill and valley releases, respectively, while "L" denotes a late-time calculation.

Table 1. Case Summary.

w_* (ms^{-1})	S		
	0	0.25	0.5
0.5	A0	A1H	A2H
	A0L	A1V	A2V
		A1L	A2L
1.0	B0	B1H	B2H
	B0L	B1V	B2V
		B1L	B2L

4. VELOCITY FIELDS

Since the primary focus of this paper is the effects of significant terrain on dispersion, only a brief review of the velocity field statistics will be presented.

Figure 1 shows the mean streamlines with $S = 0.5$ for the two heat fluxes (the A2 and B2 cases). The streamlines show a clear reversed flow in the valleys and acceleration over the ridge crests. Clearly, the separation zone is smaller for the higher heat flux case, most likely a result of greater vertical

mixing. The zero streamline is an indication of where, to some extent, the flow in the valleys is de-coupled from the flow above. This naturally has significant implications for dispersion. For example, material released in a valley is more likely to become trapped in a recirculating flow under lower heat flux conditions. Furthermore, less vertical mixing implies that the material will remain in the recirculation zone for a longer time.

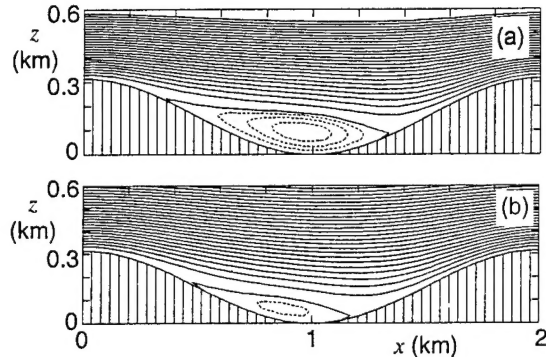


Figure 1. Mean streamlines over $S = 0.5$ ridges with (a) $w_* = 0.5 \text{ ms}^{-1}$, (b) $w_* = 1 \text{ ms}^{-1}$. Contour interval is $40 \text{ m}^2\text{s}^{-1}$ for positive values, $10 \text{ m}^2\text{s}^{-1}$ for negative values (shown dashed).

The $S = 0.25$ cases (not shown) have much less mean flow separation, particularly with the higher heat flux. However, reversed flow still occurs intermittently.

Vertical profiles of the mean streamwise velocity component are shown in Figure 2 for $S = 0.5$ and $S = 0$. The profiles are presented as perturbations from the mean sectional bulk average, defined as

$$u_b(x) = \frac{1}{H - h(x)} \int_{h(x)}^H u dz$$

where H is the boundary layer depth. The profiles over the valley are typical of much of the flow and show significantly enhanced shear compared with the flat cases. The shear is generally greater in magnitude as well as vertical extent. This is significant since Taylor's analysis for the longitudinal dispersion coefficient, D_∞ , is based on a convolution integral of the velocity perturbations, namely

$$D_\infty = -\frac{1}{H} \int_0^H u' \int_0^z K_z^{-1} \int_0^\eta u' d\xi d\eta dz$$

where K_z is the vertical diffusivity (Elder 1959). Hence, the greater the shear, the greater the longitudinal dispersion. Furthermore, greater vertical mixing reduces longitudinal dispersion. Although Taylor's analysis is only valid at late times (after complete vertical mixing) and over homogenous terrain, we still expect the enhanced shear and reduced vertical

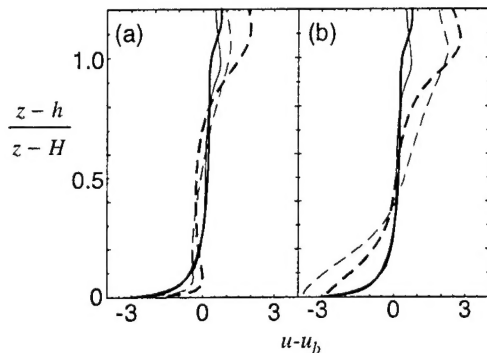


Figure 2. Mean perturbation velocity profiles. Solid lines indicate flat terrain, dashed lines $S = 0.5$; thin lines indicate $w_* = 0.5 \text{ ms}^{-1}$, thick lines $w_* = 1 \text{ ms}^{-1}$. (a) Hill crest and (b) valley bottom.

mixing of the lower heat flux case to result in enhanced dispersion.

5. DISPERSION STATISTICS

Ensemble statistics from the puffs or particles were generated at selected times (at intervals of 120s for the puffs and 100s for the particles). Due to space limitations, only longitudinal statistics (in the x -direction, normal to the hill crests) will be presented.

The total ensemble longitudinal second moment, T_{xx} , is the sum of a meander component, M_{xx} , and a relative dispersion component, S_{xx} :

$$T_{xx} = M_{xx} + S_{xx}$$

where

$$M_{xx} = \langle (\bar{x} - \langle \bar{x} \rangle)^2 \rangle$$

and

$$S_{xx} = \sqrt{\langle \sigma_{xx} + (x - \bar{x})^2 \rangle}$$

where an overbar denotes a mass-weighted average over all puffs for a particular realization and angle brackets denotes averaging over all realizations. Thus, the ensemble longitudinal cloud centroid is given by $\langle \bar{x} \rangle$. Note that for particle statistics the overbar simply indicates averaging over all particles of a realization since no mass is associated with a particle. Here, σ_{xx} is the individual puff longitudinal second-moment about its centroid (zero for a particle).

These moments, as functions of time, are shown in Figure 3 for the various short-range cases. It can be seen that the total spread T_{xx} is quite similar for A0 and B0, but this is actually due to offsetting trends in the relative and meander components. Not surprisingly, M_{xx} is greater in B0 due to the large-scale eddies characteristic of the convective boundary layer. The larger S_{xx} in A0 is probably due to the reduced vertical mixing, which allows puffs to remain in the near-surface shear region for a relatively long time.

The effects of terrain, at least for the slopes considered in this study, are quite substantial and show sensitivity to release location and thermal stability. The $S = 0.25$ hill releases (A1H and B1H) probably show the smallest differences from the flat terrain cases, but nonetheless some subtle effects are apparent. For approximately the first 500 s, the total spread is reduced compared to A0 and B0 due to a reduction in the meander component. (This is also seen in A2H and B2H.) Subsequently, the relative component in A1H is enhanced relative to both A0 and B1H, most likely due to terrain-induced shear.

The valley releases with $S = 0.25$ show rather surprising behavior regarding the meander component. In both A1V and B1V, M_{xx} increases rather rapidly for the first 500 s and then levels off. The early behavior is probably due to the intermittency of the separation in the valleys: while some releases initially get trapped in a recirculation zone and move slightly upstream for some time, others simply move downstream, thus resulting in a wide separation between centroids of different realizations. The fact that M_{xx} then levels off implies that the centroids of different realizations move downstream more or less in parallel. This, in turn, is probably an indication that little material is becoming trapped in a neighboring valley (which we assume would occur intermittently and hence result in an increase in M_{xx}). In contrast, puffs from some of the hill releases do become trapped, especially since their small size at this stage means they can easily be transported by downdrafts and recirculation zones. Thus, especially in B1H, the meander component is still increasing at 1800 s. This may also partially explain the larger relative components for A1H and B1H: S_{xx} will likely increase if some material gets trapped in a separation bubble.

All $S = 0.5$ cases ultimately result in enhanced total dispersion compared with the corresponding $S = 0.25$ and flat cases. This is principally due to the relative components which are enhanced both by the increase in mean shear and possibly by material getting trapped in recirculating flow. As with the $S = 0.25$ cases, S_{xx} is apparently converging for the hill and valley releases by the end of the calculations. Early on, S_{xx} is somewhat larger for the hill releases, as with A1H and B1H, due to material being brought down immediately into a valley and getting sheared out.

The meander components of A2V and B2V are an interesting study in contrasts. M_{xx} in B2V behaves in a manner similar to A1V and B1V in that it increases rapidly for approximately the first 500 s. Even with the larger slope, the separation in this case is rather intermittent, which as explained above, results in a relatively large meander component. However, after the first 200 s, M_{xx} in A2V is reduced relative to A2H, B2H and B2V. In this case, the separation zones are larger and tend to persist longer than

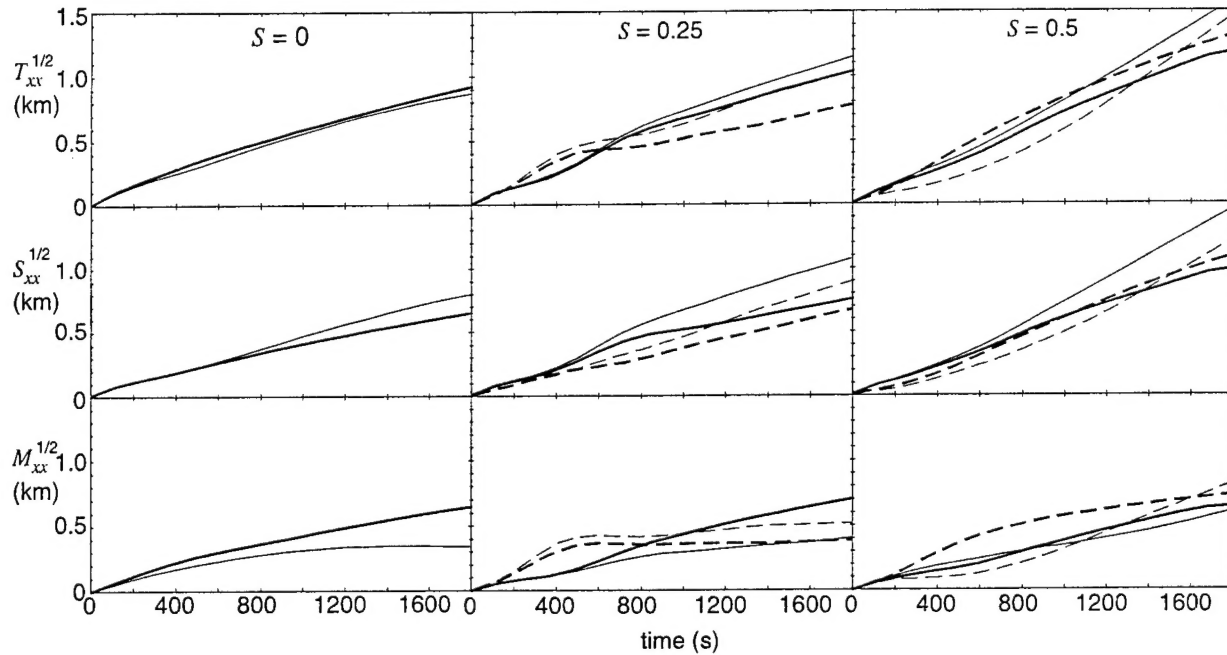


Figure 3. Longitudinal spreads from puff calculations for various hill slopes and release locations. Solid lines indicate hill releases, dashed lines valley releases; thin lines correspond to "A" cases, thick lines to "B" cases.

for the lower heat flux case. Thus virtually all realizations of A2V are initially released into a recirculation zone and remain in it for some time, with the result that the separation of the individual realizations is reduced. This is illustrated in Figure 4, which shows the longitudinal centroid locations for individual realizations of A2V and B2V. Note that the centroids of all A2V realizations remain in the original valley ($\bar{x} < 1$ km) for the first 1000 s; about half are still in at 1800 s, the end of the calculation. In contrast, while most realizations of B2V do evidently get released into recirculating flow, many nonetheless leave the valley quite quickly and all have left by approximately 1400 s. Figure 4 also illustrates why M_{xx} in A2V is still increasing at the end of the calculation while it is leveling off in B2V. The A2V realizations show a large variation in valley residence times, resulting in a rapid increase of the meander component. This will continue until all realizations have left the valley, as has already occurred with B2V.

We now examine longer simulations where the clouds become quite large, typically spanning a number of hill wavelengths, and presumably the initial source conditions are unimportant. Since a puff calculation would require a prohibitive number of puffs, we use particles to generate these dispersion statistics. While the particle simulations cannot provide detailed information about the concentration fields, they are adequate for computing centroids and second-moments. We are mainly interested in determining "late-time" behavior, which generally implies

steady growth of the second-moment and can only exist when material is vertically well-mixed.

The longitudinal second-moments from these cases are shown Figure 5. Generally, the spreads increase with slope. This is due entirely to the relative component since, as expected, the meander components all level off after a while. The $S = 0.5$ cases A2L and B2L take the longest to obtain a constant M_{xx} , most likely due to the larger-scale motions induced by the larger terrain features.

The increase in S_{xx} with slope is most evident in the lower heat flux cases. In contrast, the higher heat flux, moderate slope case, B1L, shows virtually no enhanced dispersion over B0L, although B2L does show considerably larger relative dispersion. For both non-zero slopes considered, the lower heat flux

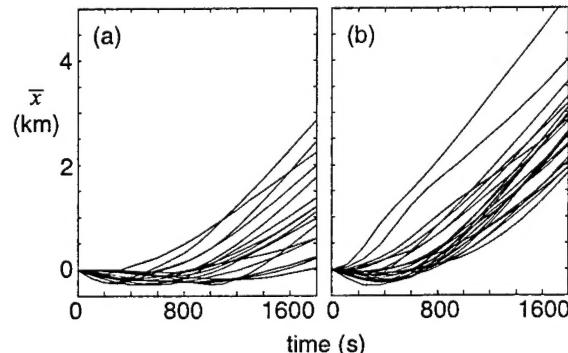


Figure 4. Longitudinal centroid position of individual realizations from (a) A2V and (b) B2V.

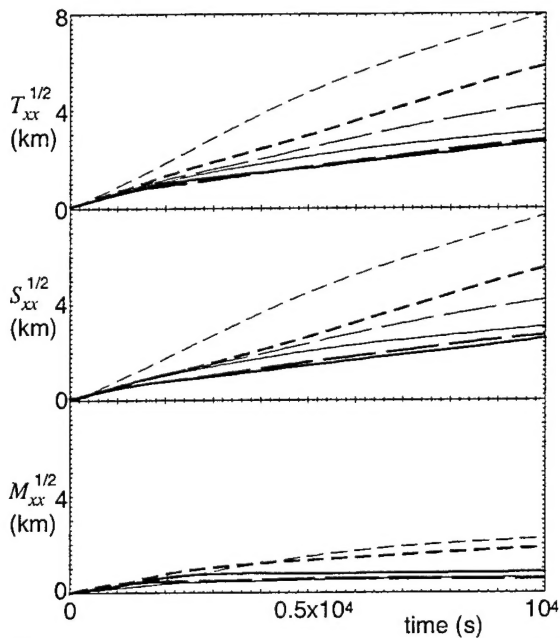


Figure 5. Longitudinal spread from late-time particle simulations. Solid lines: A0L (thin), B0L (thick); long dashes: A1L (thin), B1L (thick); Short dashes: A2L (thin), B2L (thick).

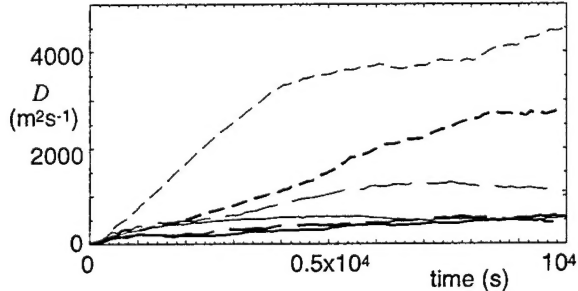


Figure 6. Longitudinal diffusion coefficients from late-time calculations. Line patterns as in Figure 5.

cases show greater dispersion than the corresponding high heat flux cases.

It is convenient to define a time-dependent longitudinal dispersion coefficient based on the rate of increase in the longitudinal second moment:

$$D(t) = \frac{1}{2} \frac{dS_{xx}}{dt}$$

This becomes equivalent to Taylor's late-time dispersion coefficient D_∞ when dS_{xx}/dt becomes constant. (We use the relative component since Figure 5 shows that the meander component is negligible at late-time.) Figure 6 shows that D is greatly enhanced by the terrain in this study, except for B1L, which is not very different from the flat terrain case. Most cases have achieved more or less steady values by approximated 5000 s, the exception being B2L. A2L

shows quite rapid early growth before leveling off to $D_\infty \approx 4000 \text{ m}^2 \text{s}^{-1}$, roughly eight times the flat terrain value. The continued growth in B2L is rather surprising given the length of this integration. It may reflect some unsteadiness in the wind fields on the Coriolis timescale and needs further investigation.

6. CONCLUSION

LES has been used to investigate dispersion over idealized ridge/valley terrain. It has been found that dispersion is generally enhanced by terrain, but that it can be sensitive to release location with respect to flow features such re-circulation zones, intermittent separation, vertical mixing and velocity shears. Late-time dispersion is shown to be significantly enhanced for large slopes, the dispersion coefficient being eight times the flat terrain value for the largest slope and lowest heat flux considered in this study.

Acknowledgment. This work was supported by the U.S. Army Research Office.

REFERENCES

Clark, T. L. (1977), "A small-scale dynamic model using a terrain-following coordinate transformation", *J. Comp. Phys.*, **24**, 186-215 .

Dörnbrack, A. and U. Schumann (1993), "Numerical simulation of turbulent convective flow over wavy terrain", *Boundary-Layer Met.*, **65**, 323-355.

Elder, J. W. (1959), "The dispersion of marked fluid in turbulent shear flow", *J. Fluid Mech.*, **5**, 544-560.

Gong, W., P. A. Taylor and A. Dörnbrack (1996), "Turbulent boundary-layer flow over fixed aerodynamically rough two-dimensional sinusoidal waves", *J. Fluid Mech.*, **312**, 1-37.

Henn, D. S. and R. I. Sykes (1996), "Large-eddy simulation of dispersion over terrain", Ninth Joint Conference on the Applications of Air Pollution Meteorology, AMS, Atlanta, GA.

Henn, D. S. and R. I. Sykes (1997), "Large-eddy simulation of flow over wavy surfaces", First AFSOR International Conference on DNS and LES, Ruston, LA.

Krettenauer, K. and U. Schumann (1992), "Numerical solution of turbulent convection over wavy terrain", *J. Fluid Mech.*, **237**, 261-300 .

Mason, P. J. (1989), "Large-eddy simulation of the convective atmospheric boundary layer", *J. Atmos. Sci.*, **46**, 1492-1516 .

Sykes, R. I. and D. S. Henn (1995), "Representation of velocity gradient effects in a Gaussian puff model", *J. Appl. Met.*, **34**, 2715-2723.

Sykes, R. I. and D. S. Henn (1989), "Large-eddy simulation of turbulent sheared convection", *J. Atmos. Sci.*, **46**, 1106-1118 .